

AN INTERCOMPARISON OF FORWARD CALCULATED  
ALBEDO TO SATELLITE OBSERVED ALBEDO  
IN CIRRUS CLOUDS

by

Donald G. Shannon

A thesis submitted to the faculty of  
The University of Utah  
in partial fulfillment of the requirements for the degree of

Master of Science

**DISTRIBUTION STATEMENT A**  
Approved for Public Release  
Distribution Unlimited

Department of Meteorology

The University of Utah

August 1999

DTIC QUALITY INSPECTED 4

19990907 168

## REPORT DOCUMENTATION PAGE

Form Approved  
OMB No. 0704-0188

Public reporting burden for this collection of information is estimated to average 1 hour per response, including the time for reviewing instructions, searching existing data sources, gathering and maintaining the data needed, and completing and reviewing the collection of information. Send comments regarding this burden estimate or any other aspect of this collection of information, including suggestions for reducing this burden, to Washington Headquarters Services, Directorate for Information Operations and Reports, 1215 Jefferson Davis Highway, Suite 1204, Arlington, VA 22202-4302, and to the Office of Management and Budget, Paperwork Reduction Project (0704-0188), Washington, DC 20503.

1. AGENCY USE ONLY (Leave blank)			2. REPORT DATE 23.Aug.99	3. REPORT TYPE AND DATES COVERED THESIS
4. TITLE AND SUBTITLE AN INTERCOMPARISON OF FORWARD CALCULATED ALBEDO TO SATELLITE OBSERVED ALBEDO IN CIRRUS CLOUDS			5. FUNDING NUMBERS	
6. AUTHOR(S) CAPT SHANNON DONALD G				
7. PERFORMING ORGANIZATION NAME(S) AND ADDRESS(ES) UNIVERSITY OF UTAH			8. PERFORMING ORGANIZATION REPORT NUMBER	
9. SPONSORING/MONITORING AGENCY NAME(S) AND ADDRESS(ES) THE DEPARTMENT OF THE AIR FORCE AFIT/CIA, BLDG 125 2950 P STREET WPAFB OH 45433			10. SPONSORING/MONITORING AGENCY REPORT NUMBER FY99-281	
11. SUPPLEMENTARY NOTES				
12a. DISTRIBUTION AVAILABILITY STATEMENT Unlimited distribution In Accordance With AFI 35-205/AFIT Sup 1			12b. DISTRIBUTION CODE	
13. ABSTRACT (Maximum 200 words)				
14. SUBJECT TERMS			15. NUMBER OF PAGES 109	
			16. PRICE CODE	
17. SECURITY CLASSIFICATION OF REPORT	18. SECURITY CLASSIFICATION OF THIS PAGE	19. SECURITY CLASSIFICATION OF ABSTRACT	20. LIMITATION OF ABSTRACT	

Copyright © Donald G. Shannon 1999

All Rights Reserved

THE UNIVERSITY OF UTAH GRADUATE SCHOOL

SUPERVISORY COMMITTEE APPROVAL

of a thesis submitted by

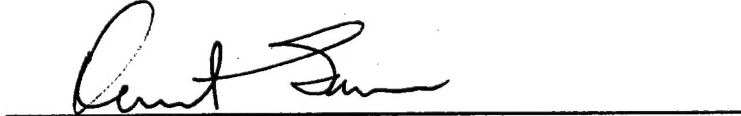
Donald G. Shannon

This thesis has been read by each member of the following supervisory committee and by majority vote has been found to be satisfactory.

June 22, 1999

  
Chair: Gerald G. Mace

June 22, 1999

  
Kenneth Sassen

June 22, 1999

  
Steven K. Krueger

THE UNIVERSITY OF UTAH GRADUATE SCHOOL

FINAL READING APPROVAL

To the Graduate Council of the University of Utah:

I have read the thesis of Donald G. Shannon in its final form and have found that (1) its format, citations, and bibliographic style are consistent and acceptable; (2) its illustrative materials including figures, tables, and charts are in place; and (3) the final manuscript is satisfactory to the supervisory committee and is ready for submission to The Graduate School.

June 22, 1999



Gerald G. Mace  
Chair, Supervisory Committee

Approved for the Major Department



---

Edward J. Zipser  
Chair

Approved for the Graduate Council

---

David S. Chapman  
Dean of The Graduate School

## ABSTRACT

Cirrus clouds are one of the least understood components of the global climate system. The Atmospheric Radiation Measurement (ARM) program is attempting to resolve the scientific uncertainties surrounding the effects of clouds on global climatic change. To this end, the ARM program is compiling continuous observations of clouds, including cirrus microphysical properties using a diverse suite of instruments, at several climatically significant locations around the globe. One of the algorithms used by the ARM program to derive the cirrus microphysical properties employs reflectivity measurements from a millimeter wavelength radar, and infrared emission spectra observed by an interferometer. In an effort to validate the results derived from this reflectivity-radiance algorithm, the effects of cirrus clouds on the radiation field, calculated using the microphysical properties retrieved by the algorithm, are compared against atmospheric radiative quantities derived from satellite observations and surface radiometers. For 15 cirrus events, the top of the atmosphere albedo calculated from the algorithm's retrievals is compared against the shortwave broadband albedo derived from satellite observations. In an attempt to move toward closure of the column radiation budget, for two case studies, comparisons are made between the calculated and observed surface solar fluxes. Using the results from the two case studies, we attempt to draw conclusions regarding the topic of anomalous absorption of solar radiation in cloudy atmospheres. Problems encountered during this research with the Moderate Resolution Transmittance (MODTRAN) radiative transfer code are also presented.

19990907 168

## TABLE OF CONTENTS

ABSTRACT .....	iv
ACKNOWLEDGMENTS .....	vi
INTRODUCTION .....	1
Background .....	1
Goals of this Research .....	7
DATA ANALYSIS.....	9
FL93 Parameterization .....	9
JM98 Algorithm .....	12
MODTRAN RADIATIVE TRANSFER CODE .....	17
Background .....	17
MODTRAN 3 Version 1.3 .....	20
MODTRAN 4 Version 1.1 .....	34
ALBEDO AND SOLAR FORCING COMPARISONS.....	40
Background .....	40
The "Observed" Albedo .....	42
The "Calculated" Albedo .....	43
Results .....	45
24 March 1997 .....	46
27 May 1998 .....	66
Calculated and Observed Albedo Correlation .....	83
Anomalous Absorption .....	86
SUMMARY AND CONCLUSIONS.....	93
APPENDIX: ALBEDO COMPARISONS.....	97
REFERENCES .....	106

## ACKNOWLEDGMENTS

First and foremost, I would like to thank my advisor, Dr. Jay Mace. This project would never have reached completion without his expertise and guidance. I would especially like to thank him for his patience and understanding of my Air Force mission, as a student in the Air Force Institute of Technology (AFIT), Civilian Institution program.

I would also like to thank Dr. Pat Minnis and his research associates at NASA's Langley Research Center, Atmospheric Sciences Division, Radiation Science Branch. Their data, derived from the NOAA GOES 8 satellite, was instrumental in the completion of this project.

The majority of the data used for this research project was obtained from funding provided by the Atmospheric Radiation Measurement (ARM) Program. This program is sponsored by the U.S. Department of Energy, Office of Science, Office of Biological and Environmental Research, Environmental Sciences Division.

Finally and most importantly, I would like to thank my family. To my parents, George and Dolores Shannon: thank you for your never-ending love, support, guidance and discipline. Your efforts have enabled me to soar to great heights, and the best is still to come. To my brother, Dan: I would like to thank you for the inspiration and knowledge only an older brother can impart. Hopefully, I have done the same for you. To my wife, Monica: your love, patience, compassion and encouragement are truly heaven-sent. From your example, I know that what may seem impossible and insurmountable, is made possible through faith and determination.

## CHAPTER 1

### INTRODUCTION

#### Background

Clouds play a critical role in the energy balance of the earth's climate system. On average, clouds continuously cover approximately 50% of the earth's atmosphere (Liou 1986). Validation of this statement can readily be seen from any modern, meteorological satellite image. Of these clouds, cirrus clouds account for nearly 20% of the global coverage (Liou 1986). However, because of their location in the frigid upper troposphere, their detailed structure and microphysical composition has been difficult to quantify. With the advent of sophisticated meteorological instruments, scientists have been able to more effectively probe cirrus clouds and postulate, test, and model their influences on the earth-atmosphere system.

While it is clear that cirrus clouds are an integral component of the global climate system, scientists still struggle with identifying the nature of their impact on the system. Unlike water clouds, cirrus, on average, contain significant amounts of relatively large, nonspherical ice crystals (Takano and Liou 1989) of low concentrations. As a result, they are normally optically thin and nonblack in the thermal infrared. Ackerman et al. (1988) showed that optically thin cirrus over warm surface regions enhance the infrared greenhouse effect (warm) on the atmosphere. However, Liou (1986) showed that as the optical thickness of cirrus increases, cirrus exert a cooling effect on the climate by reflecting more of the incident solar radiation back to space. Additionally, Liou (1986) and

Manabe (1975) have shown that the location, or height, of cirrus also affect the sign of their radiative effect. Finally, Stephens et al. (1990) determined that all cirrus feedback to the climate system is strongly modulated by the microphysical properties of the cloud.

Regardless of the sign of the cirrus radiative effect, the degree and extent of the greenhouse-versus-albedo effect involving cirrus clouds will result in significant atmospheric differential cooling and heating in both the vertical and horizontal scales. These combined feedbacks have been recognized to be dominant modes in the perturbation of the earth's meteorological processes; for processes whose time-scales are on the order of synoptic and global weather patterns. The sensitivity of the atmospheric general circulation, to cirrus cloud occurrence and cirrus microphysical properties, has been documented by many recent modeling studies (e.g., Lohman and Roeckner 1995).

Since the earth's climate system is sensitive to cirrus, it is important that cirrus clouds are properly accounted for in global climate models. Unfortunately, due to the complexity of the interaction of solar and infrared radiation with the nonspherical, highly variable cirrus particles, it is a virtual certainty that current climate models do not treat cirrus correctly (Mace et al. 1998a). Therefore, the conclusions drawn from the response of climate models to changes in cirrus, and the sensitivity of cirrus clouds to other climate forcing mechanisms, should be viewed and implemented with caution.

Due to the observational and computational shortcomings surrounding cirrus, scientists often employ "effective" cloud parameters to describe cirrus radiative properties and forcings. According to Mace et al. (1998a), the principal problem with current cirrus parameterizations lies in the small amount of observational data relating cirrus macrophysical, microphysical, and radiative properties to the atmospheric state resolved

by a large-scale model. Even though a number of recent research programs surrounding cirrus have been directed at crossing this scientific barrier, the results they present, represent a few instantaneous samples in a broadly distributed continuum (Mace et al. 1998a). Furthermore, we do not, as yet, know where in this continuum these events exist.

The Department of Energy (DOE) has attempted to fill the gaps in this data, in part, through their Atmospheric Radiation Measurement (ARM) program. The ARM program's efforts, to resolve scientific uncertainties surrounding the effects of clouds on global climatic change, have a specific focus on improving the performance of general circulation models. One portion of this pursuit involves the operation of field research sites, known as Cloud and Radiation Testbeds (CART). The CART sites are heavily instrumented surface facilities located around the globe, in climatically significant locations. The diverse array of instruments located at each site continuously gather data. The three primary CART locations are the Southern Great Plains (SGP) site, the Tropical Western Pacific (TWP) site, and the North Slope of Alaska/Adjacent Arctic Ocean (NSA/AAO) site. The SGP site, the first operational ARM CART site, has been in operation since 1992. The location of the ARM SGP CART site is identified by the red square, in northern Oklahoma, as seen in Figs. 1 and 2.

One of the many instruments available at the ARM SGP CART site is the millimeter wave cloud radar (MMCR). The MMCR is a zenith-pointing, doppler radar with an operating frequency of 35 GHz ( $\lambda \approx 8.57$  mm). Its main purpose is to distinguish cloud boundaries (e.g., cloud base and cloud top); although Sassen and Khvorostyanov (1998) illustrate problems associated with millimeter wavelength radars and their ability to accurately detect cirrus cloud top. The radar's doppler capability allows scientists to

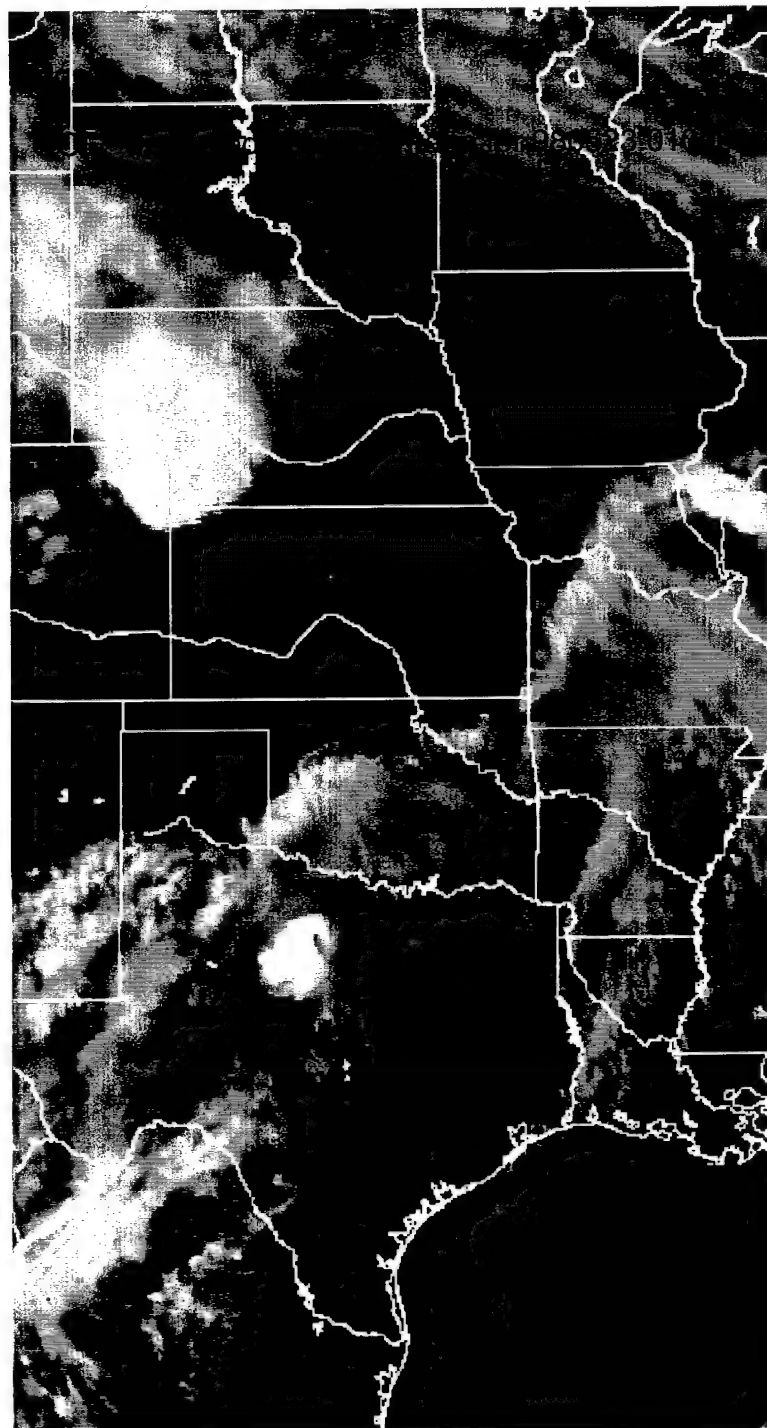


FIG. 1. Infrared satellite image taken from the meteorological Geostationary Satellite (GOES) 8. The red square identifies the ARM SGP CART site.

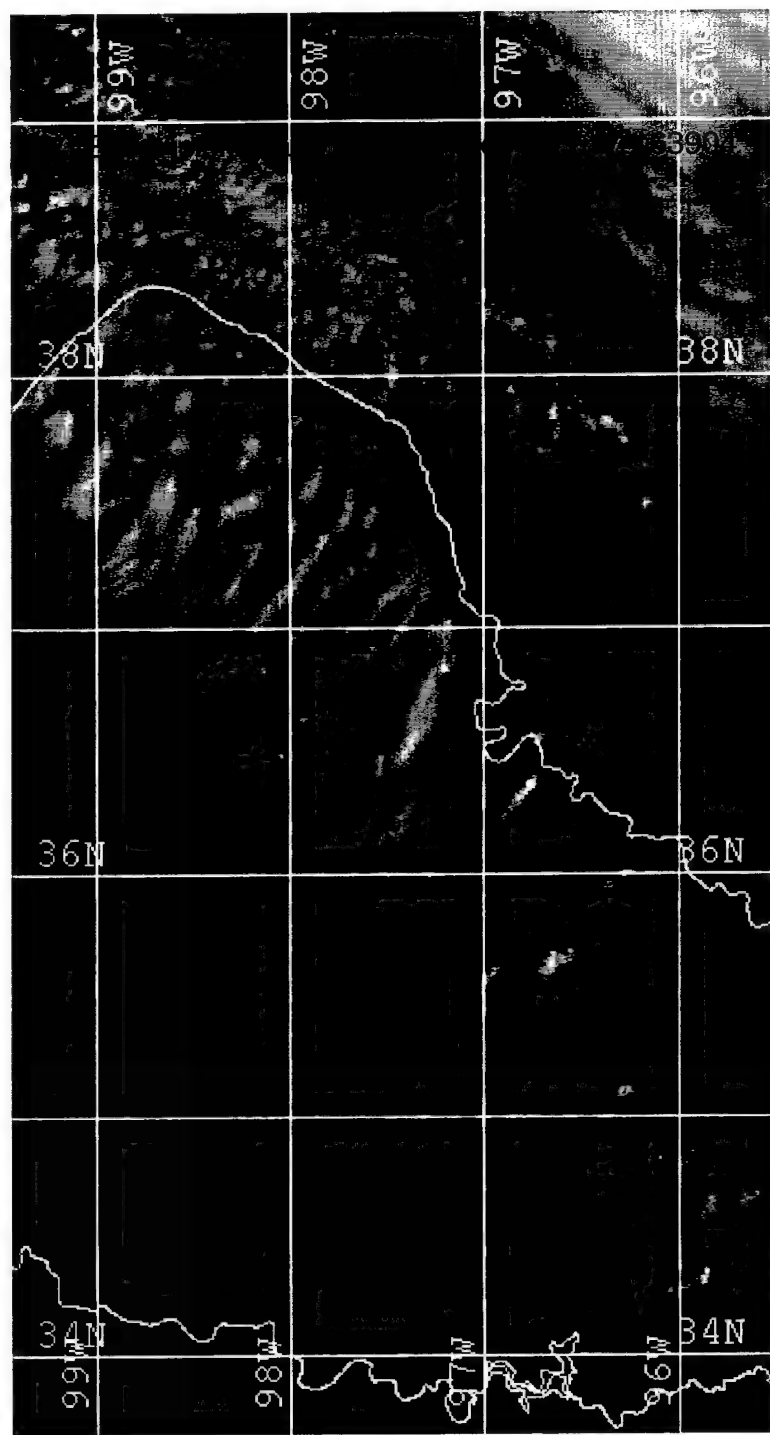


FIG. 2. High resolution visible satellite image taken from GOES 8. The red square identifies the location of the ARM SGP CART site. The site is located at  $36.6^{\circ}$  N and  $97.5^{\circ}$  W.

measure cloud constituent vertical velocities. Additionally, this radar will return the reflectivity (dBZ) of the atmosphere up to 20 kilometers.

Another instrument available at the SGP site is the atmospheric emitted radiance interferometer (AERI). This device measures the absolute infrared spectral radiance of the sky directly above the instrument. The spectral range of the instrument is 3 to 20 microns. The data gathered from the instrument can be used to quantify the spectral signature of the downwelling radiance in much of the thermal infrared. From the fine spectral detail of the AERI data, it is possible to retrieve the vertical atmospheric profile of temperature and water vapor. Additionally, the AERI data have been used to evaluate/validate line-by-line calculations from radiative transfer codes, among other applications.

The data accumulated by these two instruments, when combined in conjunction with sophisticated algorithms, have been used to effectively derive cirrus cloud microphysical properties. One such algorithm, that employs the data retrieved by these two instruments, is described in Mace et al. (1998a; hereinafter the algorithm will be referred to as JM98).

JM98 combines the AERI observed infrared radiance data with the MMCR reflectivity measurements to derive the microphysical properties of cirrus cloud layers. The properties retrieved are layer-averaged and, therefore, do not require homogeneous cirrus layers persisting for several hours. JM98 employs the parameterizations presented by Fu and Liou (1993; hereinafter referred to as FL93), but with a modified meaning for the FL93 ice crystal equivalent width,  $D_e$ . In JM98,  $D_e$  is redefined as the radius hexagonal ice crystals would have if converted to equivalent ice spheres. This conversion is based on regression analysis and the ice crystal dimensions presented by Auer and Veal

(1970). The goal of the JM98 research is to use the retrieved microphysical properties to evaluate the effect that optically thin cirrus have on the radiation fields at the surface and the top of the atmosphere. Further information regarding JM98 can be found in Chapter 2 and via the internet at the following address: <http://www.met.utah.edu/mace/homepages/research/archive/tech.html>

#### Goals of this Research

The algorithm of JM98 is currently being employed operationally on the ARM data streams. The ARM goal is to continuously monitor and archive the layer-averaged microphysical properties of optically thin cirrus. As with any algorithm or parameterization, comparison of the algorithm's results against observations is a necessity. Through this process, confidence in the product is gained and opportunities for refinements may be identified from both successful and unsuccessful results. Since cirrus clouds are known to exist in great variability, numerous comparisons are necessary to ensure confidence in the algorithm's results. Since the ultimate goal of JM98, and the ARM program, is to evaluate cloud effects on the radiation field, comparison of the calculated effects cirrus have on the atmospheric radiation field with observed atmospheric radiative properties are preferred.

The main goal of this research has been to determine the effectiveness of the JM98 algorithm and its retrieved cirrus properties. A secondary goal of this research was to determine, based on the data analyzed here, if cloudy atmospheres (cirrus) absorb more solar radiation than theory predicts.

To accomplish the main goal, the retrieved microphysical properties were used as input to the Moderate Resolution Transmittance (MODTRAN) radiative transfer model

(Berk et al. 1989), to calculate atmospheric radiance at solar wavelengths. These calculated radiances, and hence the retrieved cirrus properties, were to be validated through comparison to satellite-observed solar radiances. Unfortunately, the MODTRAN radiative transfer code did not work properly, and this route had to be abandoned. The research and problems involving the use of MODTRAN are further detailed in Chapter 3.

Even though the first approach was unsuccessful, another, similar, approach was adopted in an effort to accomplish our overall goal. The retrieved cirrus properties were used as input to the radiative transfer code of Toon et al. (1989). This code is known as the Rapid Radiative Transfer Code (RAPRAD). RAPRAD was used to calculate the downwelling (toward the earth's surface) and upwelling (away from the earth's surface) atmospheric solar fluxes. The top of the atmosphere (TOA) fluxes were combined to determine the model-calculated solar albedo. These calculated albedos were then compared to albedos derived from GOES 8 radiances. Chapter 4 describes the comparisons, presents two, in-depth case studies, and provides statistics and results from the 15 cirrus events compared during this research. The calculated fluxes were further utilized to examine the second research goal -- do (cirrus) clouds absorb more solar radiation than theory predicts? A further explanation of anomalous absorption, and what the data from this research have to say about this controversial topic, can also be found in Chapter 4. Finally, Chapter 5 presents some conclusions and recommendations for further research.

## CHAPTER 2

### DATA ANALYSIS

#### FL93 Parameterization

The complexity and variability of cirrus clouds, and the uncertainties surrounding their interaction with incoming solar and outgoing infrared radiation, require scientists to employ parametric relationships to describe cirrus radiative properties. One parameterization used to reliably and efficiently characterize the broadband solar and infrared radiative properties of cirrus clouds is FL93.

The parameterization of FL93 incorporates the scattering and absorption properties of hexagonal ice crystals, the correlated  $k$ -distribution method for non gray gaseous absorption in scattering cloudy atmospheres, and the radiative transfer methodology known as the  $\delta$ -four-stream approximation. According to Fu and Liou (1993), their parameterization is an improvement over previous parameterizations of cirrus broadband radiative properties (e.g., Liou and Whitman 1979), because they account for the effects caused by the hexagonal shape of cirrus crystals. Additionally, Fu and Liou (1993) contend the effects of ice crystal size distributions were not included in previous parameterizations. However, FL93 incorporates cirrus particle size distributions based on in-situ aircraft observations. Assuming that the observed particles are hexagonal columns, FL93 represents the particle size distribution through the use of an area-weighted mean crystal width ( $D_e$ ).

From  $D_e$  and the cirrus cloud ice water content (IWC), FL93 derives the basic single-scattering properties of ice crystals using third-order polynomial equations. Two of the single-scattering radiative properties derived by FL93 are the extinction coefficient ( $\beta$ ) and the single-scattering albedo ( $\omega_0$ ). The polynomial equation for the extinction coefficient is written as

$$\beta = IWC \sum_{n=0}^N \frac{a_n}{D_e^n} \quad (1)$$

where  $a_n$  represents spectrally-dependent coefficients determined through a numerical fitting scheme, the units of  $D_e$  and IWC are microns ( $\mu\text{m}$ ) and grams per cubic meter ( $\text{g}/\text{m}^3$ ), respectively, and  $N = 2$ . The coefficients,  $a_n$ , are also sensitive to the bulk density of ice ( $\rho_i$ ). The effective density of ice crystals has been shown to be a function of particle size (Brown and Francis 1995). This results from the internal air pockets that form during crystal growth. As such, cirrus particles tend to be hollow in nature. Thus, the bulk density of these hollow crystals can be quite different than the density of solid ice. When the coefficients of equation (1) were originally determined, the calculations were performed with the density of ice ( $\rho_{io}$ ) equal to 0.9167 grams per cubic centimeters ( $\text{g}/\text{cm}^3$ ). Therefore, the coefficients,  $a_n$ , as given in Table 3, of Fu and Liou (1993), need to be adjusted by a factor  $\rho_{io}/\rho_i$ . According to Fu and Liou (1993), this expression for  $\beta$  is sufficient to yield an accuracy within 1%.

Fu and Liou (1993) use a similar polynomial expansion, in terms of  $D_e$ , to derive the single-scattering albedo for cirrus ice crystals. It is written as

$$1 - \omega_o = \sum_{n=0}^N b_n D_e^n \quad (2)$$

In this case,  $N = 3$  is necessary to attain an accuracy within 1%, and the polynomial coefficients,  $b_n$ , are only spectrally dependent. Once again, the coefficients are determined through a numerical fitting scheme. They are given in Table 4 of Fu and Liou (1993).

FL93 uses similar polynomial expansions to derive the scattering phase function of cirrus crystals, as an expansion of Legendre polynomials, and the asymmetry parameter ( $g$ ), a measure of the degree of forward scattering of the phase function. For brevity, these equations will not be provided here. However, these equations are given as (2.11), (2.12), (2.13a), (2.13b), (2.14), and (2.15) in Fu and Liou (1993). Care should be taken when using the phase function in radiative transfer calculations. The FL93 parameterization of the cirrus phase function is only strictly applicable in flux and heating rate calculations. For more precise radiative transfer calculations (i.e., radiance calculations), the full phase function (e.g., Takano and Liou 1989) must be employed (Q. Fu 1998, personal communication).

A final note regarding the coefficients used in the FL93 polynomial expansion equations is required. As mentioned in the preceding paragraphs, the coefficients were determined from numerical fitting to data computed from "exact" light scattering and absorption programs (Fu and Liou 1993). For ice crystals with size parameters larger than 30, FL93 used the geometric ray-tracing program from Takano and Liou (1989), to determine the coefficients. However, for particles with size parameters less than 30, there was no exact solution for hexagonal crystals available to fit the data. Therefore, FL93 used

results computed from a modified light scattering program developed for spheroids (Takano et al., 1992). Although naturally occurring ice crystals will have a hexagonal shape that cannot be approximated by spheroids, the smaller size parameters are usually associated with infrared wavelengths. In this portion of the electromagnetic spectrum, ice crystals are highly absorbing (Liou 1986). Hence, Fu and Liou (1993) concluded that for crystals with size parameters smaller than 30, the detailed shape factor may not be critical in scattering and absorption calculations.

#### JM98 Algorithm

As previously stated, JM98 seeks to derive the layer-mean microphysical properties of optically thin cirrus. The algorithm employs the MMCR radar reflectivity and the AERI observed downwelling radiance to derive these microphysical properties. The complete algorithm description will not be developed here. However, the key concepts will be discussed to provide the reader with the basic understanding of JM98.

One of the major components of JM98, is the implementation of a modified version of FL93. In JM98, the meaning of  $D_e$  is redefined as the radius ice crystals would have if converted from hexagonal columns to equivalent ice spheres. This is necessary since the algorithm formulates the radar reflectivity in terms of spherical particles. Upon initial inspection, this may seem to pose a problem. As mentioned before, spheroids cannot approximate the hexagonal shape of naturally occurring ice crystals. However, the MMCR's wavelength is quite large in comparison to the crystal sizes. Hence, the size parameter, for radar wavelengths, is so small that the exact shape of the crystal is not critical for the radar reflectivity. This fact was confirmed by Schneider and Stephens (1995), where exact backscattering calculations were compared to the sphere

approximation. The redefinition of  $D_e$  in JM98 is based on regression analysis and the aspect ratios given by Auer and Veal (1970). The relationship between  $D_e$  and the JM98 particle radius is given by the following polynomial expansion.

$$D_e = \sum_{i=0}^4 C_i r_e^i \quad (3)$$

where  $C_i$  are constant coefficients listed in Table 1 of Mace et al. (1998a), and  $r_e$  is the effective spherical radius of the ice crystal. Equation 3 is substituted into Equations (1) and (2) to provide the layer-averaged extinction coefficient and single-scattering albedo. Using the results from equation (1) and (2), the layer emittance can be found from

$$\epsilon = 1 - \exp[-(1 - \omega_o)\beta\Delta h] \quad (4)$$

where  $\Delta h$  is the layer thickness derived from the radar reflectivity.

Another major component of JM98 is the assumption that the layer-mean particle distribution can be described by a single order, modified gamma distribution. Recasting this relationship in terms of the modal crystal diameter ( $D_x$ ) and the number of particles per unit volume per unit length at the functional mode ( $N_x$ ), the particle size distribution is given by

$$N(D) = N_x \exp(\alpha) \left[ \frac{D}{D_x} \right] \exp \left[ -\frac{(D\alpha)}{D_x} \right] \quad (5)$$

where  $\alpha$  is the order of the distribution. From analysis of in-situ data, Dowling and Radke (1990) found  $\alpha \leq 2$  for cirrus. Based on this work, JM98 assumes  $\alpha = 1$  in all cases.

Combining equation (5) with the radar equation, the relation between the equivalent radar reflectivity factor ( $Z$ ),  $N_x$ , and  $D_x$  is found to be

$$Z = N_x \exp(\alpha) D_x^7 \left[ \frac{(6+\alpha)!}{\alpha^{7+\alpha}} \right] \quad (6)$$

A similar approach can be used to derive the layer IWC, the layer ice water path (IWP), the total particle concentration ( $N_T$ ), and  $r_c$ . These relations can be found in Mace et al. (1998a) as equations (5), (6), and (7), respectively.

Additional considerations regarding the structure of ice crystals must be accounted for in the algorithm. As mentioned in the previous section, cirrus crystals tend to be hollow. As a result, Mace et al. (1998a) list the effective density of ice crystals, and the effect that the departure of bulk density from solid ice has on the radar reflectivity, as two major concerns that must be incorporated into the algorithm. With these two considerations taken into account, equation (4) can be written to express  $D_x$  in terms of the layer emittance and radar reflectivity as

$$\frac{[\ln(1-\varepsilon)]}{k_1 \bar{Z} \Delta h} = \frac{C_1 k_2^3 D_x^5 + C_2 k_2^2 D_x^4 + C_3 k_2 D_x^3 + C_4 D_x^2 + \frac{C_5}{k_2} D_x + \frac{C_6}{k_2^2}}{D_x^2 \left[ B_0 D_x^3 + \frac{B_1}{k_2} D_x^2 + \frac{B_2}{k_2^2} D_x + \frac{B_3}{k_2^3} \right]} \quad (7)$$

where

$$k_1 = \left[ \frac{k_i^2}{k_w^2} \right] \rho_{i, solid}^2 \frac{\pi}{6} \alpha^3 \left[ \frac{(3+\alpha)!}{(6+\alpha)!} \right] \quad (8)$$

$$k_2 = \left(\frac{1}{2}\right) \left[\frac{(3+\alpha)!}{(2+\alpha)!}\right] \left(\frac{1}{\alpha^2}\right) \quad (9)$$

and the constant coefficients,  $C_n$ , are determined by combinations of the FL93 coefficients,  $a_n$  and  $b_n$ , newly redefined by equation (3). The coefficients,  $B_n$ , arise from the parameterization used to account for the effective density of the ice crystals; as listed in Table 3 of Mace et al. (1998a). And,  $k_w$  and  $k_i$  are the refractive indices of water and ice, respectively.

Using the MMCR reflectivity, and the AERI observed downwelling radiance to determine the layer emittance, equation (7) can be solved numerically for  $D_x$ . In turn,  $D_x$  can be used to determine  $N_x$ ,  $r_e$ , and  $N_T$ . With  $D_x$  and  $r_e$  known, the layer radiative properties can be found using the parameterizations of FL93.

A final note regarding the JM98 algorithm and its application with cirrus containing very small crystal sizes is necessary. As given by the radar equation,

$$Z = \int_0^\infty N(D) D^6 dD \quad (10)$$

the reflectivity is a function of the sixth moment of the particle distribution. According to Mace et al. (1998a), the radiance depends, to first order, on the second moment of the particle distribution (the integrated ice mass). Hence, they conclude that the algorithm is insensitive to the smallest particles, if any, in the particle size distribution. As a result, JM98 relies on the distribution of the larger particles to predict the distribution of the smaller. Thus, the accuracy of the algorithm to predict the smaller particles is dependent on the correlative relationship between the larger and smaller sizes. Mace et al. (1998a)

site analysis of in-situ probe data that contends this correlative relationship can be weak, bimodal, and possibly unrelated in some cases. However, since the algorithm provides layer-averaged microphysical quantities, the authors state that this possible drawback may not have significant adverse affects on their algorithm's capabilities. Further research is necessary to substantiate this claim.

Additionally, the JM98 algorithm is affected by the poor scattering response of the millimeter wavelength radar signals to the very small ice particles in cirrus. Sassen and Khvorostyanov (1998) illustrate this problem very well. Thus, at cirrus cloud top, in portions of cirrus clouds where new particle generation is occurring, or in contrail cirrus, the MMCR may not be able to effectively sample the minute crystals contained in these regions. As such, the IWC of the cirrus derived from the radar reflectivity may be underestimated in these instances. Sassen and Khvorostyanov (1998) list the discrepancy of deducing IWC (a measure of the  $\Sigma r^3$ ) from the radar reflectivity (a measure of the  $\Sigma r^6$ ) as a formidable problem facing radar remote sensing of cirrus clouds.

## CHAPTER 3

### MODTRAN RADIATIVE TRANSFER CODE

#### Background

The Moderate Resolution Transmittance (MODTRAN) Code is a radiative transfer code developed under the direction of Air Force Material Command's, Air Force Research Laboratory, Space Vehicle Directorate, Battlespace Environment Division, Background Clutter Mitigation Branch (AFRL/VSBM), located at Hanscom Air Force Base, Massachusetts. MODTRAN calculates atmospheric transmittance and radiance in the spectral wavenumber range from 0 to 50,000  $\text{cm}^{-1}$ , at moderate spectral resolution. Although the code can be run with minimal user input, it has the capability to perform radiative transfer simulations using a wide variety of atmospheric conditions.

The radiative transfer simulations can use standard seasonal atmospheric profiles and molecular, aerosol, and gaseous concentrations, or incorporate user-defined input (up to 34 atmospheric layers). Computations can be performed with or without multiple scattering included (up to 16 streams), depending on the precision required by the user. Complicated geometrical paths for the radiative transfer simulation can be readily implemented. The code allows users to perform calculations with or without clouds. Additionally, the latest version of the code enables the user to define many lower tropospheric clouds (to include precipitation) in great detail and in mixed phases. The flexibility of the model made it very attractive as a research tool. My status as an AFIT student and active duty officer in the Air Force made it an even more appealing research

platform. Unfortunately, there is one drawback with MODTRAN. Its cirrus cloud model is very restrictive, with many of the cloud's microphysical properties fixed. Therefore, MODTRAN's cirrus model (ICLD=18) tends to be unrepresentative of the highly variable cirrus microphysical characteristics found in the atmosphere.

If a user includes the model cirrus clouds in radiative transfer calculations, MODTRAN assumes a 64  $\mu\text{m}$  mode radius for the ice particles. The only information a user can supply for cirrus clouds is the height of the cloud base, the cloud thickness, and the extinction coefficient. The optical thickness of the cloud ( $\tau$ ) is derived from the product of the extinction coefficient and the cloud thickness.

$$\tau = \beta \Delta h \quad (11)$$

The remainder of the cirrus microphysical properties are fixed in the model and information regarding their values is not provided in the user's guide (Beck et al. 1989; Anderson et al. 1998). The scattering phase function used for the cirrus particles is also not defined in the user's guide, and was unknown by the model's point of contact (J. Chetwynd 1998, personal communication). Mr. Chetwynd assumed that MODTRAN's cirrus phase function is modeled after the Henyey-Greenstein phase function (Henyey and Greenstein 1941) (hereinafter referred to as HG), with the asymmetry parameter included as standard model data. Although the halos and other sharp features of the cirrus phase function tend to diminish as the size parameter decreases (as wavelength increases), and, in these instances, the HG phase function *might* be able to approximate the "exact" cirrus phase function (Q. Fu 1998, personal communication), for most solar radiative transfer calculations involving cirrus, this approximation is inadequate. Fu and Takano (1994)

have shown that attempting to describe the cirrus phase function by a single parameter, in terms of the asymmetry factor (as done in HG), can result in solar flux calculations with errors as large as 70%.

Fortunately, MODTRAN provides for a user-defined cloud as optional input (ICLD = 11). This option triggers the code to read the user-defined, spectrally-dependent cloud extinction coefficient, absorption coefficient, and asymmetry parameter from a nonstandard portion of the input file. Additionally, a conversion factor from equivalent liquid water content to extinction coefficient, normalized to the equivalent liquid water content for an extinction coefficient of  $1.0 \text{ km}^{-1}$  at a wavelength of  $0.55 \mu\text{m}$ , is required. To delineate the cloud boundaries (top and base), the user invokes the ICLD1 = 11 option in the 34-layer, user-defined atmospheric profile (Card 2C3), marking the atmospheric "boundary" change with the layer's ICHR1 parameter. With these options in place, only one piece of information is left to properly describe the cirrus cloud -- the scattering phase function.

MODTRAN also allows the user to define a scattering phase function as nonstandard input. However, some confusion surrounds this option. The MODTRAN user's guide specifies the use of optional input cards 3B1 and 3B2 for entering user-defined phase functions. Unfortunately, the data on these cards are invoked only if the parameter IPH = 1 on a separate input card (Card 3A1). The IPH parameter is used to specify the model *aerosol* phase function selection. By setting IPH = 1, the user triggers the implementation of cards 3B1 and 3B2 for the *aerosol* phase function, in place of the model Mie-generated or HG aerosol phase function. This would lead one to believe that this user-defined phase function option does *not* apply to clouds. However, in the

concluding notes pertaining to cards 3B1 and 3B2, the user's guide specifies, "The default altitude regions [for the user-specified phase function] may be overridden by the parameters IHA1, *ICLD1*, or IVUL1 on CARD 2C3." Card 2C3 is implemented when the user wishes to specify a user-defined atmospheric profile. As mentioned previously, *ICLD1* is used (on Card 2C3) to designate clouds in a user-specified atmospheric layer. As such, will the use of Card 2C3 (user-defined atmospheric profile) and *ICLD1* = 11 (user-defined cloud) trigger the code to read the user-defined phase function for my cloud? Further reading of the MODTRAN 3 user's manual (Beck et al. 1989) does not clarify the answer to this question. In consultation with Mr. Chetwynd, he concluded the phase function for *ICLD1* = 11 *should* be able to be input using these optional phase function cards. With this last piece of the puzzle apparently in place, MODTRAN was chosen as the research tool to help accomplish the first goal of this research endeavor.

#### MODTRAN 3 Version 1.3

To validate the JM98 retrievals, comparisons were to be made between MODTRAN forward-calculated radiances, computed using the radiative properties derived from the JM98 retrievals, and satellite-observed radiances. Since radiance calculations involve specific solid-angles, very precise MODTRAN calculations were required. Hence, multiple scattering was included with a minimum of eight radiation streams used. In MODTRAN, multiple scattering calculations are performed using the discreet ordinate radiative transfer (DISORT) algorithm of Stamnes et al. (1988). The DISORT algorithm provides a numerically stable method to solve the equations of plane-parallel radiative transfer in an inhomogeneous atmosphere. The user-defined atmospheric profiles used for these calculations were derived from radiosonde data taken at the SGP

site. The cirrus phase function was given by Table 1, of Takano and Liou (1989) and is shown in Fig. 3. MODTRAN's optional input cards 3B1 and 3B2 allow the user to describe the phase function at 50 discrete scattering angles (for four atmospheric regions, with fixed boundaries). Therefore, 50 significant scattering angles were chosen from Table 1, Takano and Liou (1989), to best approximate the "exact" cirrus phase function. Also, the user-defined phase function input to MODTRAN must be normalized as

$$\int_{4\pi} P(\Theta) d\Omega = 1 \quad (12)$$

where  $P(\Theta)$  is the phase function and  $d\Omega$  represents the incremental solid angle.

With so much uncertainty surrounding the implementation of the user-defined phase function, a test of the code was performed. For the test, all input parameters, standard and user-defined, were fixed, except for the solar zenith angle. To simplify the scattering geometry, the latitude of the instrument/sensor (provided as input to MODTRAN) was moved to the equator, the instrument/sensor was modeled as a zenith-pointing instrument, and the simulation date was chosen to be the Vernal Equinox of 20 March (when the sun is directly overhead at the equator). One day's worth of calculations were performed, at 15 minute increments. From these calculations, a radiance versus time plot was created; see Fig. 4. Comparisons of this plot to a MODTRAN calculated clear sky plot (not shown) seemed to indicate that the code was correctly implementing the phase function. Significant deviations from the clear sky plot were found at scattering angles at or near the cirrus phase function halos (approximately 1600Z and 1900Z), with a huge increase in radiation at scattering angles near the cirrus forward diffraction peak (approximately 1730Z).

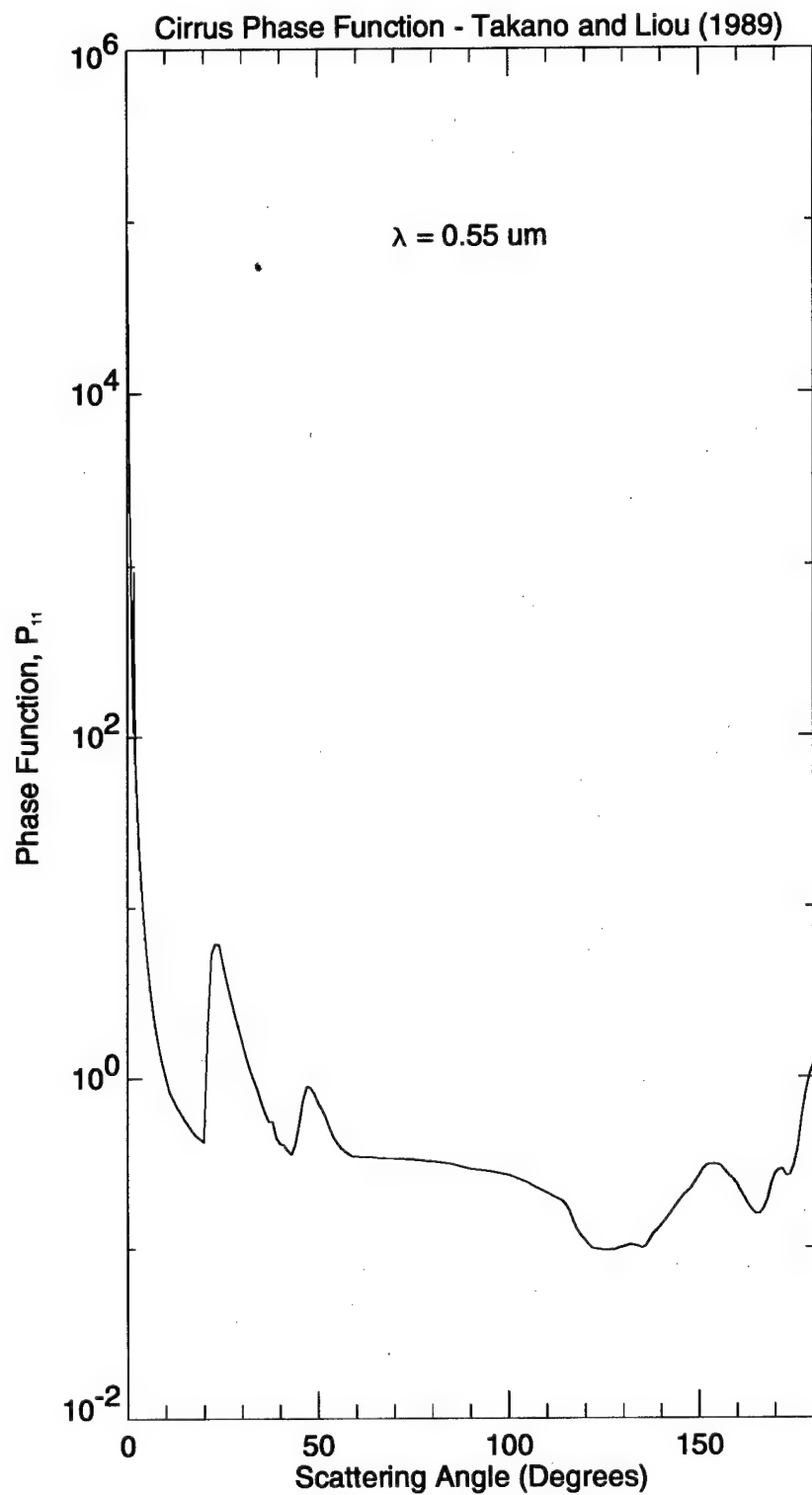


FIG. 3. Cirrus phase function for  $\lambda = 0.55 \mu\text{m}$ , as given by Takano and Liou (1989).

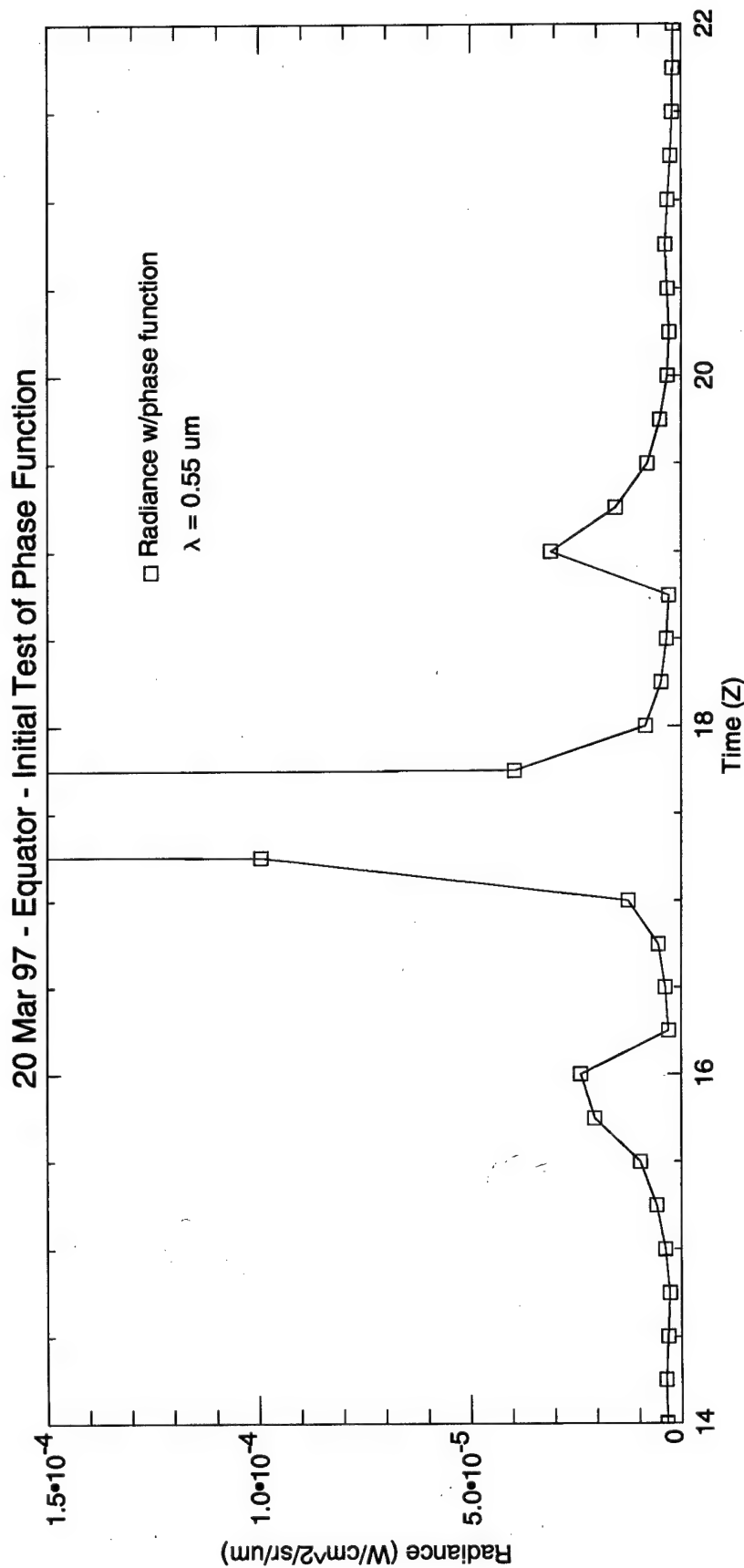


FIG. 4. MODTRAN 3 calculated radiance for 20 March 1997.

With the user-defined phase function seemingly working in conjunction with the user-defined cloud option, the decision was made to calculate radiances using the actual SGP CART site sounding and cirrus retrieval data. However, since the scattering geometry involved with satellite observations can be quite complicated, an intermediate step was implemented to gain confidence in the code and calculated radiance.

For this intermediate step, the calculated radiance determined from the actual cirrus and atmospheric data were compared to the SGP CART site's AERI-observed radiance. As mentioned previously, the AERI measures the absolute infrared spectral radiance of the sky directly above the instrument. With a fixed, zenith pointing surface instrument, the scattering geometry was very simple to model. Also, the error in the AERI measurements is well known; according to Mace et al. (1998a), Smith et al. (1993) document the AERI accuracy to be within 0.5%. A portion of the spectral bin for the AERI's channel 2 (3.31  $\mu\text{m}$  to 5.56  $\mu\text{m}$ ) falls within the near infrared portion of the electromagnetic spectrum. The spectral range chosen for this comparison was approximately 3.4  $\mu\text{m}$  to 3.7  $\mu\text{m}$ . Since the phase function given by Takano and Liou (1989) is valid for visible wavelengths, some question as to its validity in this spectral range is reasonable. Minnis et al. (1998) show that although the 22° and 46° halos, found in the cirrus phase function for visible wavelengths, are replaced by a single halo at 30° for near infrared wavelengths, the two phase functions are in general agreement with each other. As such, the cirrus phase function given by Takano and Liou (1989) was determined to be a good approximation of the actual cirrus phase function (for near infrared wavelengths) for the purposes of this intermediate comparison. The comparison was carried out for the 26 September 1997 cirrus case observed at the ARM SGP CART site.

This event was associated with the remnants of Hurricane Nora, which had tracked into the Desert Southwest from the eastern Pacific Ocean a few days earlier. The high altitude clouds associated with the remnants of Hurricane Nora were entrained into the jet stream and advected over the SGP site. A plot of the MODTRAN-calculated radiance and AERI-observed radiance for this spectral range is shown in Fig. 5.

From the plot it can be readily seen that the calculated radiance shows little or no correlation to the observed radiance. In most cases the magnitude of the observed radiance is two to three times the magnitude of the calculated radiance. Also, the trend of the calculated radiance bears little resemblance to the observed radiance. Finally, when the calculated radiance is compared to the satellite images for this day (Figs. 6 through 9), it is hard to find any relationship between the calculations and the actual cloud conditions occurring at the SGP site. Between the hours of 18Z and 21Z, the calculated radiance exhibited little or no change in magnitude. This was in direct contrast to the satellite images and retrieved cirrus properties (Fig. 10) which show the highly variable cirrus conditions that existed over the SGP CART site during these hours.

Given these poor results, it was apparent that something was awry with the calculated radiances. Unfortunately, the exact cause of the problem was not immediately known. Suspicions surrounding the implementation of the user-defined phase function with the user-defined cloud was an obvious potential source of error. However, given the complex nature of the input file, and its specific syntax and format, user error was not ruled out either. A third problem could have resulted from the use of the Takano and Liou (1989) cirrus phase function (which is given for  $\lambda = 0.55 \mu\text{m}$ ) for this comparison. As

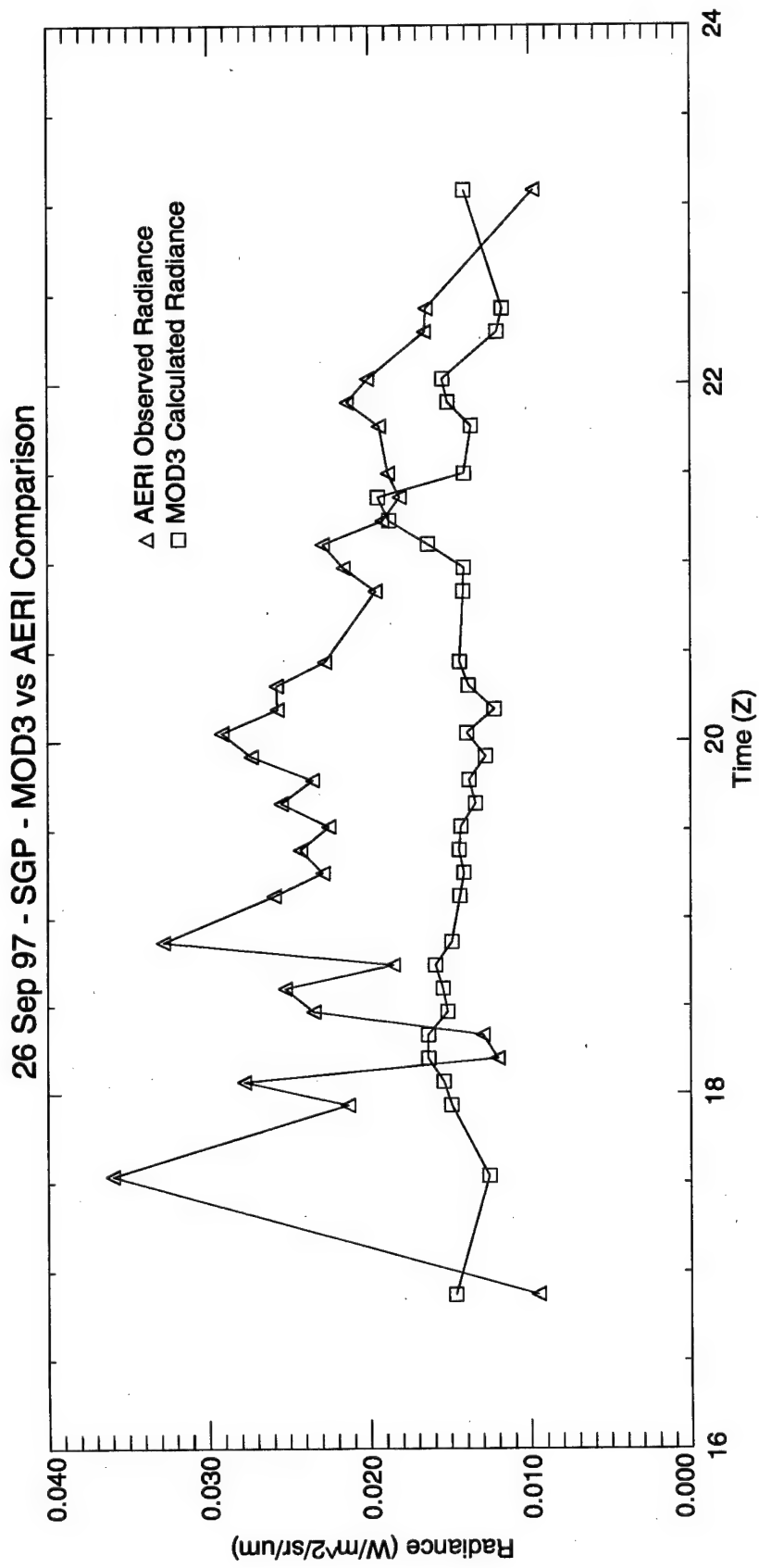


FIG. 5. MODTRAN 3 calculated and AERI-observed radiances for the ARM SGP CART site. The data was compiled from the 26 September 1997 cirrus case.

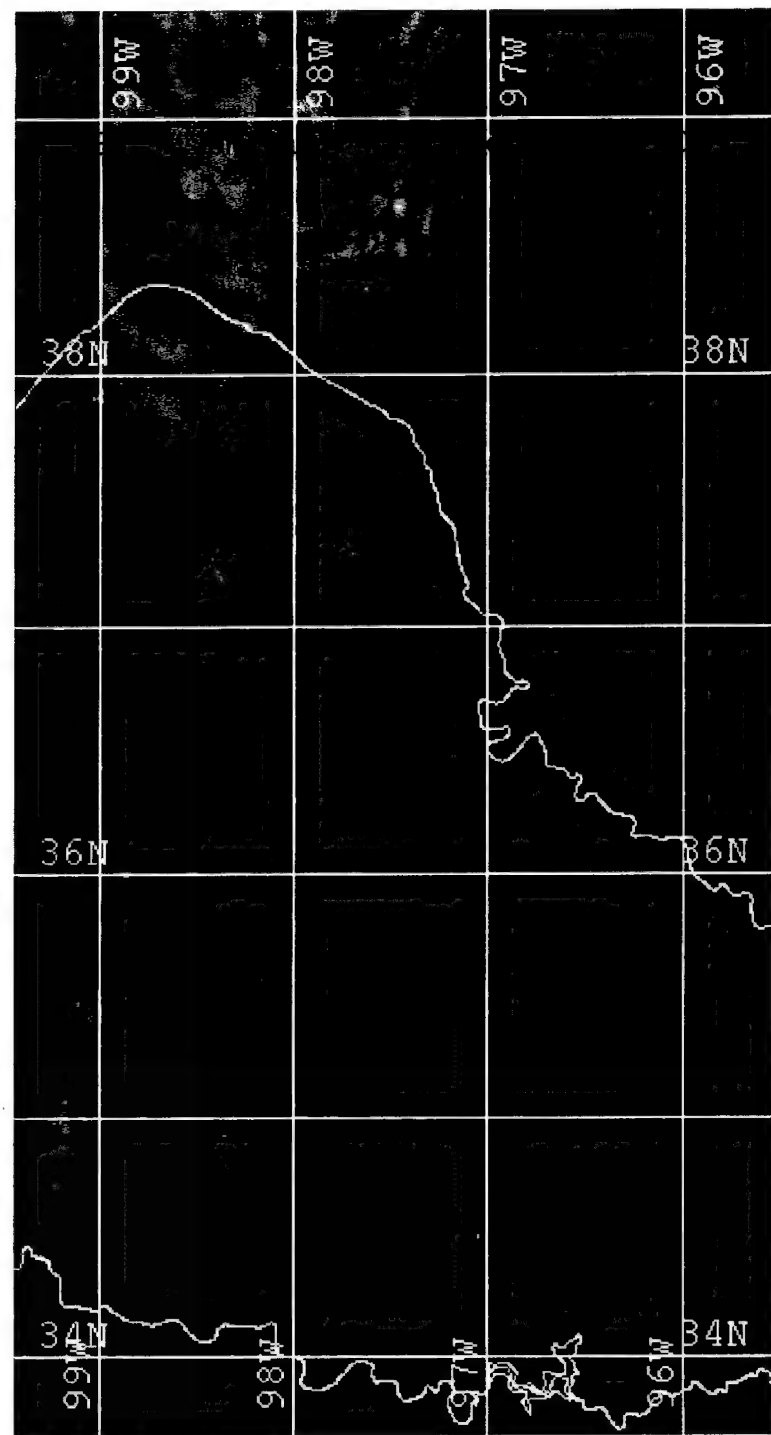


FIG. 6. GOES 8 visible satellite image for the ARM SGP CART site, 26 September 1997 cirrus case. The time of this image is 1809 Zulu.

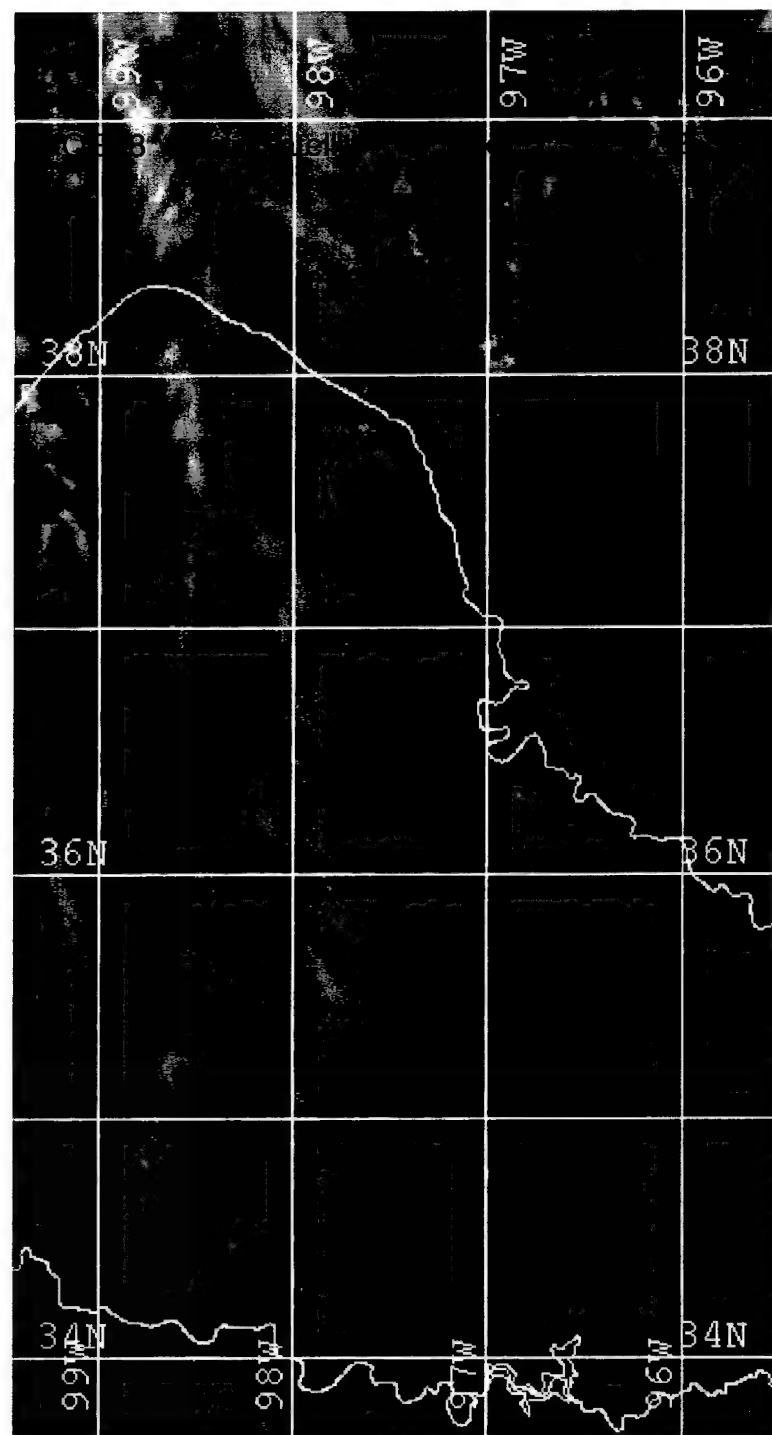


FIG. 7. GOES 8 visible satellite image for the ARM SGP CART site, 26 September 1997 cirrus case. The time of this image is 1925 Zulu.

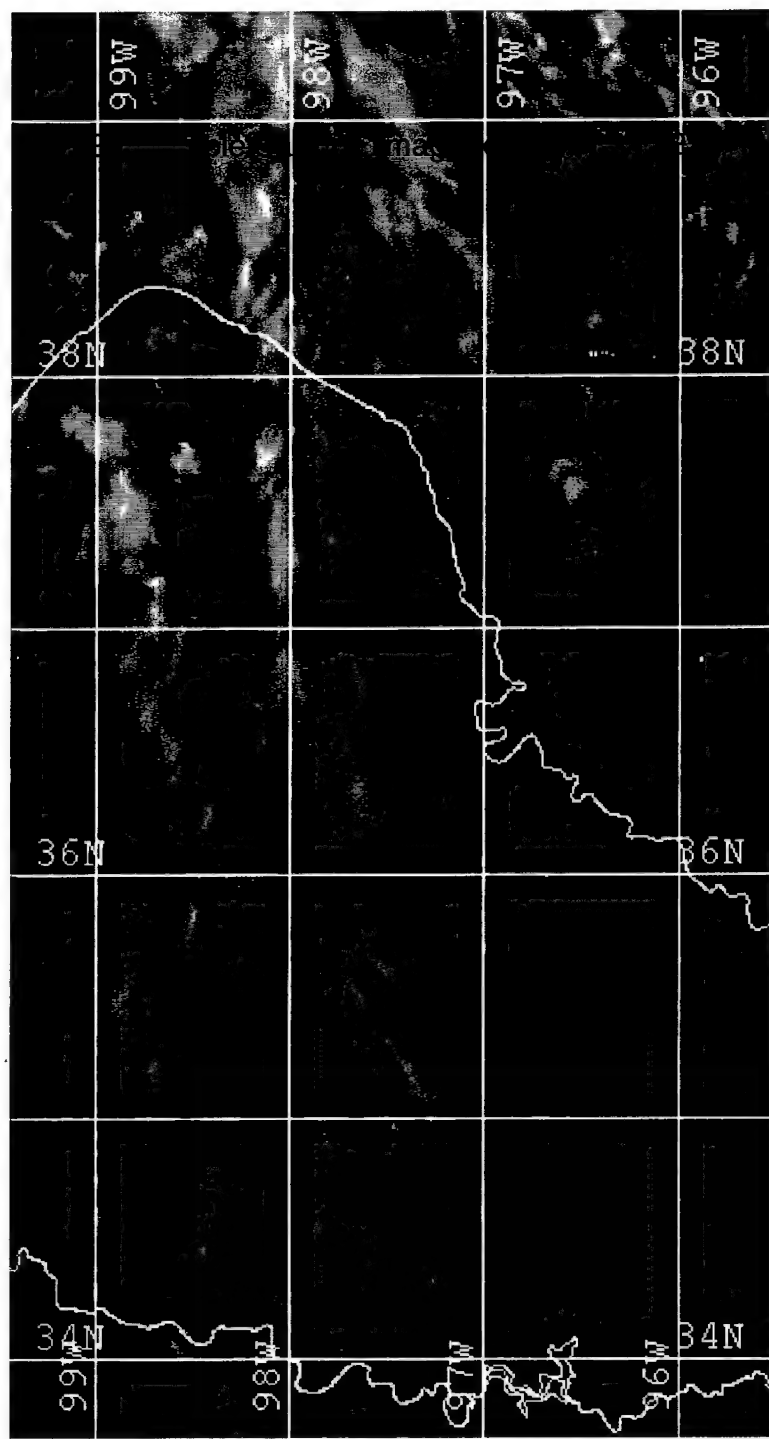


FIG. 8. GOES 8 visible satellite image for the ARM SGP CART site, 26 September 1997 cirrus case. The time of this image is 2025 Zulu.

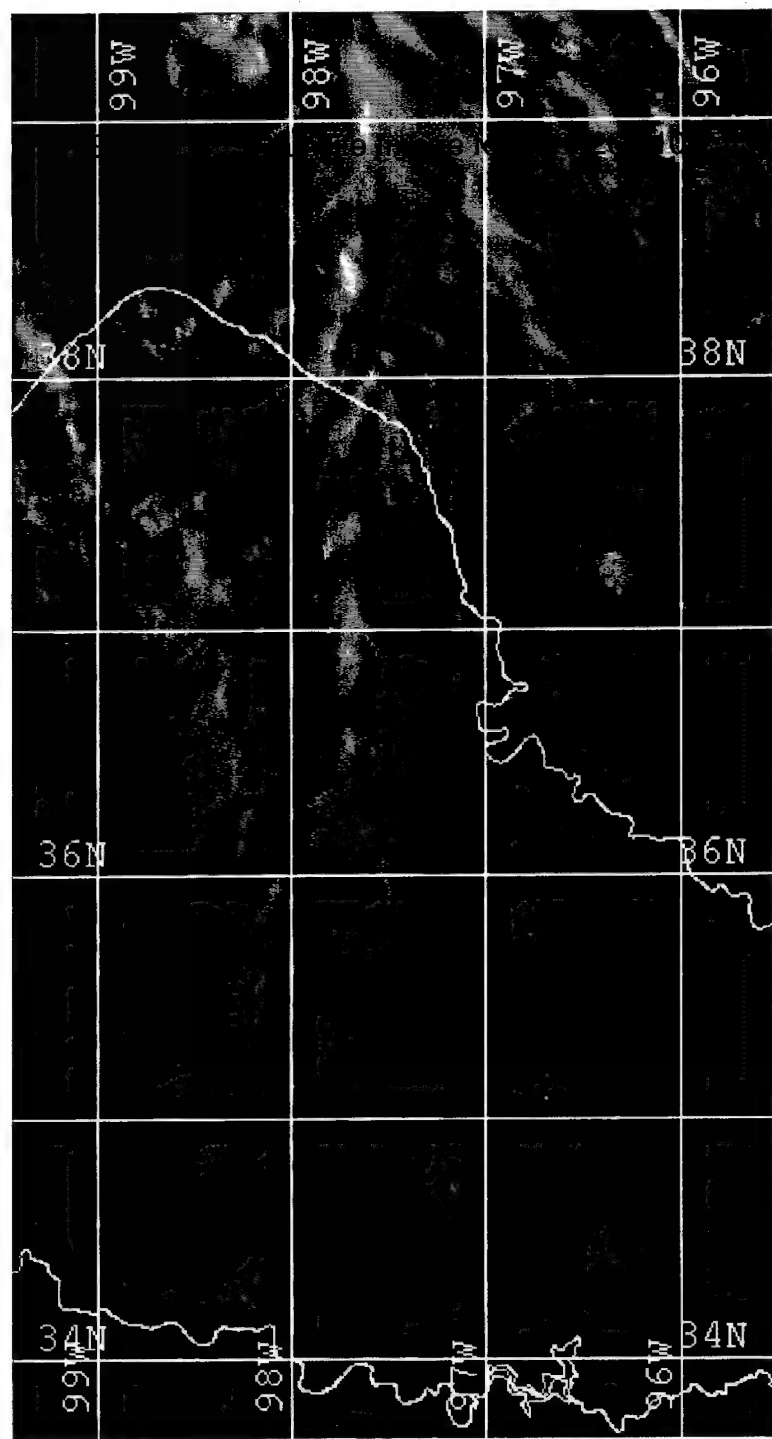
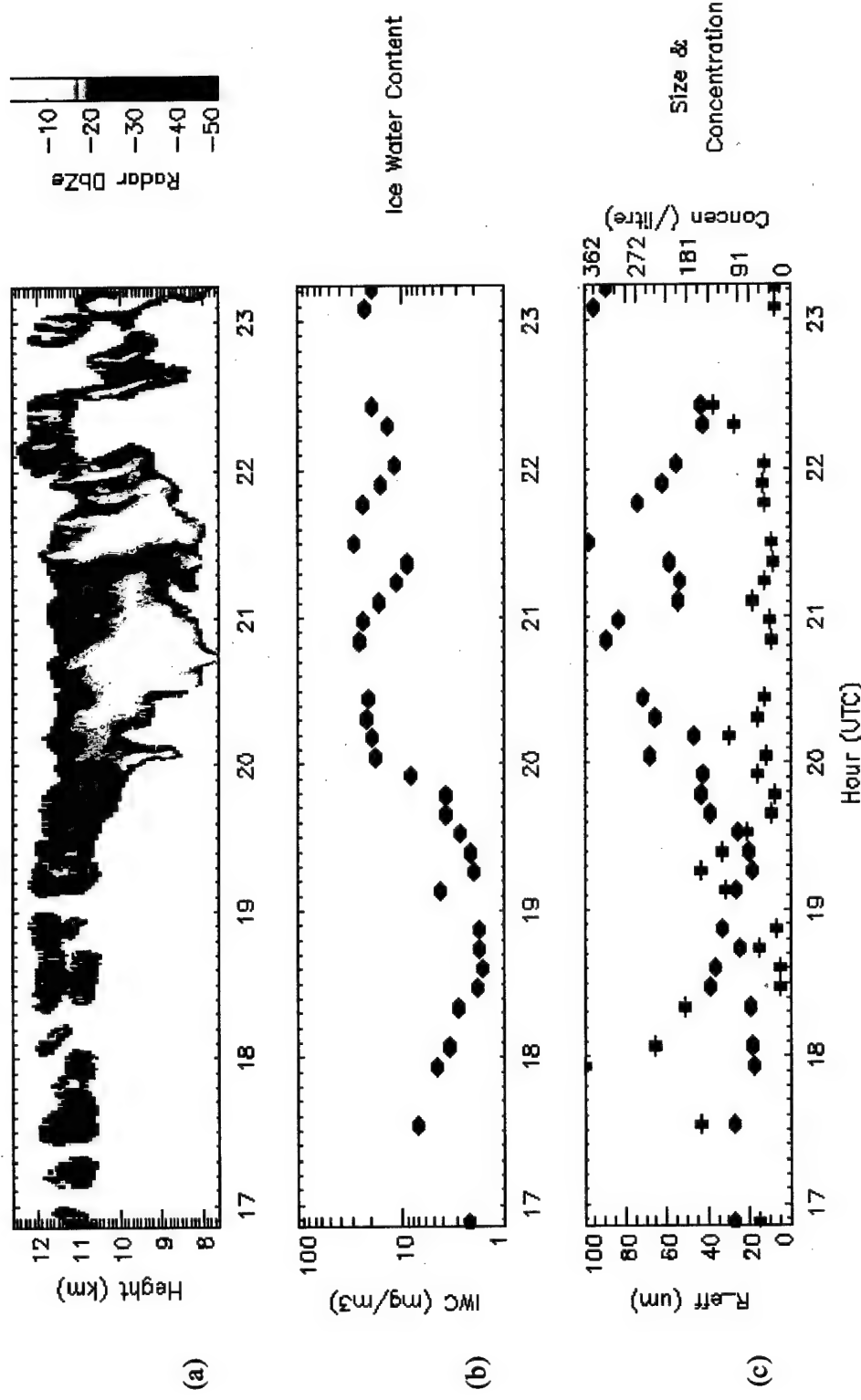


FIG. 9. GOES 8 visible satellite image for the ARM SGP CART site, 26 September 1997 cirrus case. The time of this image is 2108 Zulu.

FIG. 10. JM98 retrieved, layer-averaged cirrus cloud properties for 26 September 1997 at the ARM SGP CART site for (a) radar reflectivity, (b) ice water content, (c) particle effective radius and concentration, (d) layer emittance and visible optical depth, and (e) solar forcing - fraction of clear-sky flux removed by cloud.

Cirrus Cloud Properties 26 September 1997 SGP CART Site  
 Reflectivity Radiance Algorithm



Cirrus Cloud Properties 26 September 1997 SGP CART Site  
Reflectivity Radiance Algorithm

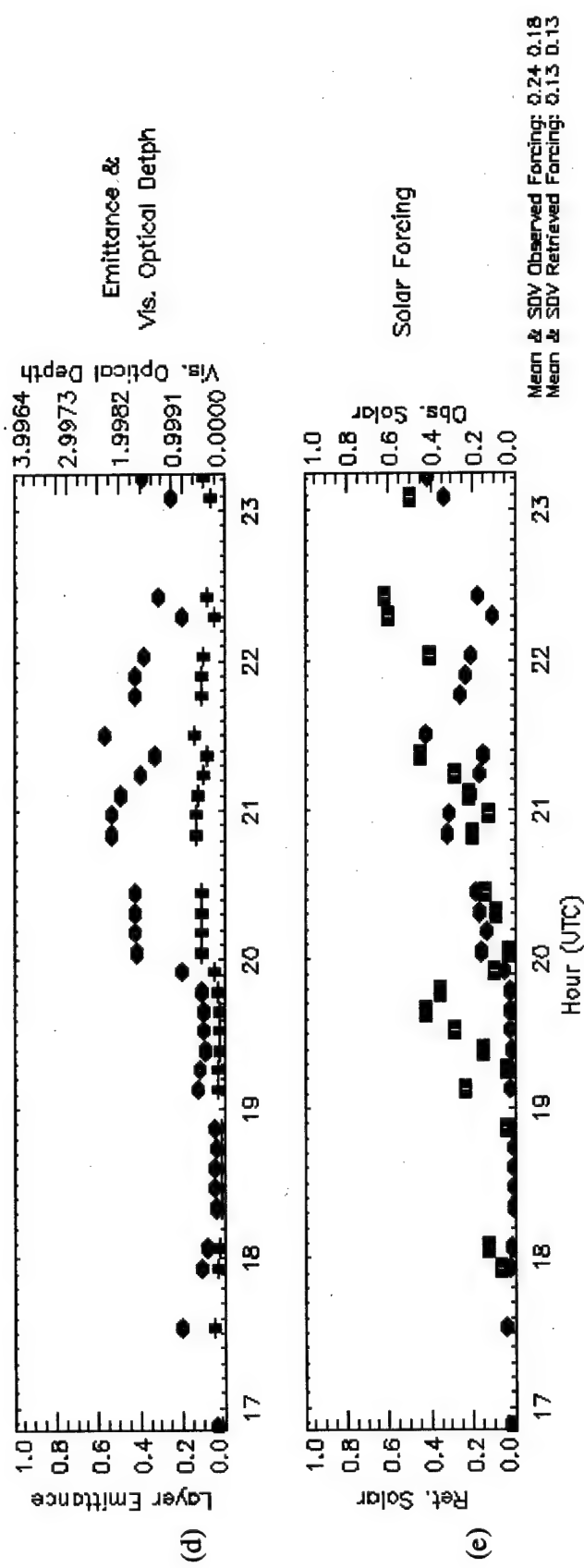


FIG. 10. Continued

mentioned previously, this comparison was done for the spectral range of  $\lambda = 3.4 - 3.7 \mu\text{m}$ . We first addressed the possibility that user error was the source of our problems.

To identify any possible user input errors, a sample input file (known as a MODTRAN tape5) was sent to Mr. Chetwynd. He examined the tape5 and verified that the syntax and format were correct. Additionally, from reading the tape5 and the MODTRAN output (known as a tape6), Mr. Chetwynd verified that MODTRAN was interpreting my input file correctly, and performing the calculations using my user-defined atmospheric profile. The code also recognized my user-defined cloud and its spectrally-defined asymmetry parameter, absorption coefficient, and extinction coefficient. However, he could not verify that the code was using the user-defined phase function for my cloud. He determined the phase function data was properly read by the code, but he could not verify its implementation. Mr. Chetwynd also noticed that the version of MODTRAN I was using was quite old. In light of this fact, he suggested that I upgrade my version of MODTRAN. MODTRAN 3 Version 1.3 had been corrected for errors, and some parametric relationships and options had been updated in later versions (J. Chetwynd 1998, personal communication). Therefore, the decision was made to upgrade to the latest version of MODTRAN.

#### MODTRAN 4 Version 1.1

MODTRAN 4 Version 1.1 (Beta) was released in December of 1998. The code was backward compatible with previous versions, so only minor modifications to input files were necessary. In addition to correcting errors found in previous versions of the code (J. Chetwynd 1998, personal communication), this version of MODTRAN professed to contain some significant enhancements over its predecessors. One of the more applicable

enhancements, for this research, was the ability of MODTRAN 4 to perform calculations with clouds, but without aerosol attenuation included. This option is invoked by setting the parameter IHAZE = -1.

The IHAZE parameter specifies the aerosol model used for the boundary layer (0 to 2 km), and the surface meteorological range (visibility). However, the values for IHAZE are also used to specify the aerosol model and meteorological range for each layer of the user-defined atmosphere; as IHA1 on Card 2C3. As such, the IHA1 = -1 option was chosen for our user-defined atmosphere. With the IHA1 parameter set to the no aerosol option, our calculations could be performed with only our user-defined cloud (ICLD1 = 11) included. In doing so we hoped to isolate the cloud's effect on the radiation fields. Simultaneously, we hoped we would be able to determine if the user-defined phase function was being applied to our cloud. Unfortunately, the results from this MODTRAN simulation did not provide any insight into the cloud's effect on the radiation field, nor did the results show that the user-defined phase function was (or was not) utilized in conjunction with our user-defined cloud. The radiance values produced, with these options in place, were unrealistic and increased without bound throughout the day. It was later determined (J. Chetwynd 1998, personal communication) that the IHAZE = -1 or IHA1 = -1 specification is not compatible with the user-defined cloud option (ICLD = 11 or ICLD1 = 11); although this is *not* specified in the user's manual (Anderson et al. 1998). In fact, the IHAZE = -1 option *may not be available* with MODTRAN 4 Version 1.1 (J. Chetwynd 1998, personal communication), even though it is listed as an option in the user's manual (Anderson et al. 1998).

Another enhancement afforded by MODTRAN 4 is the ability to adjust (stretch or compress) the boundaries of the four default altitude regions. By adjusting one of the regions to coincide with the base and top of our user-defined cloud, we hoped we could apply the cirrus phase function (Takano and Liou 1989) to only our user-defined cirrus cloud layer. The other three regions (containing code-standard aerosols) were supplied with a user-defined phase function based on the Mie scattering phase function (e.g., Stephens 1994).

In conjunction with this adjustment, we changed our user-defined cloud to a user-defined aerosol layer in an attempt to "trick" the code. This "trick" was suggested (J. Chetwynd 1999, personal communication) because of the uncertainty of the implementation of Cards 3B1 and 3B2 (user-defined phase function) with our user-defined cloud. The user-defined aerosol (IHAZE or IHA1 = 7) is defined exactly as the user-defined cloud, but it is recognized by the code as an aerosol layer. Since the user-defined phase functions are only applied when IPH = 1 (the user-defined aerosol phase function option), we hoped any problems with applying the user-defined phase function to our cloud, would be alleviated. Unfortunately, the results from this approach did not show any marked improvements over earlier methods. Additionally, it still could not be confirmed that the user-defined phase function was being applied to our user-defined cloud (aerosol) layer (J. Chetwynd 1999, personal communication).

Given our inability to isolate the problem plaguing our computational efforts, Mr. Chetwynd suggested we employ the MODTRAN model cirrus cloud (ICLD = 18) in our calculations. Even though the majority of the model cirrus' microphysical properties are fixed, Mr. Chetwynd believed this option would result in radiances within the proverbial

“ballpark” of the observed radiances. This option also greatly simplified the tape5 input file. As mentioned previously, the phase function for the model cirrus is defined in the code. So, the user-defined phase function option was dropped. The only nonstandard input used in these calculations was the user-defined 34-layer atmospheric profile. However, even this nonstandard input was simplified, since the user-defined cloud layer, within the atmospheric profile, was not necessary. Unfortunately, using the model cirrus cloud (ICLD = 18) did nothing to improve our current situation. In fact, another problem surfaced.

The radiance and transmittance values calculated using the model cirrus cloud, for the spectral range of  $\lambda = 0.54 - 0.55 \mu\text{m}$ , showed virtually no change for the highly variable 26 September 1997 SGP cirrus case. Regardless of whether the cloud’s optical thickness, as calculated using equation (11), was as thick as  $\tau \approx 8$  or as thin as  $\tau = 0.5$ , the average transmittance as reported in the MODTRAN 4 output file never changed. For these same conditions, the calculated total integrated radiance values changed only in the fifth significant digit. Even for the clear sky calculation (no cloud included; ICLD = 0), an option chosen to further highlight the problems associated with ICLD = 18, the radiance and transmittance values were nearly identical to those calculated using the model cirrus cloud! The results from the model cirrus cloud (ICLD = 18) and no cloud (ICLD = 0) simulations are compared in Table 1.

After much consultation with some of MODTRAN’s programmers at Spectral Sciences Incorporated (SSI), it was determined that the UNIX version of MODTRAN 4 Version 1.1 (Beta), distributed via the AFRL/VSBM file transfer protocol site, contained 26 *old or incorrect subroutines* (P. Acharya 1999, personal communication). The names of the affected routines are listed in Table 2.

TABLE 1. MODTRAN 4 Version 1.1 (Beta) for Unix Tape6 Output  
File Results for  $\lambda = 0.54 - 0.55 \mu\text{m}$ .

ICLD	Cloud Optical Depth ( $\tau$ )	Integrated Total Radiance (W/cm <sup>2</sup> /sr)	Average Transmittance (Unitless)
18	7.7	5.180208E-05	0.6312
0	N/A	5.180931E-05	0.6312

TABLE 2. MODTRAN 4 Version 1.1 (Beta) for UNIX  
Uncorrected Subroutines.

26 Old or Incorrect Routines			
PARAM.lst	aernsm.f	aerprf.f	aprfnu.f
dgrd.f	dprfpa.f	driver.f	flxsum.f
layvsaf.f	loop.f	rdnsm.f	scnflx.f
ssrad.f	trans.f		

Unfortunately, even after the "corrected" subroutines were received, and the code recompiled with these routines included, our results did not change significantly. It turns out that not all of the problems with the subroutines were identified or fixed (P. Acharya 1999, personal communication). In fact, Mr. Acharya said the changes made to the 26 routines were based upon the results found by using the file differencing routine (known as the diff command) common to UNIX platforms. So, a comprehensive troubleshooting of the affected routines was not accomplished. This was due, in part, to time constraints and momentary funding problems (P. Acharya 1999, personal communication) for MODTRAN support at SSI.

Given the inability of MODTRAN to definitively implement the "exact" cirrus phase function (e.g., Takano and Liou 1989), we could not, in good conscience, continue with this code for research involving radiance calculations and cirrus clouds. Additionally, and more importantly, because of the problems surrounding the simplest MODTRAN radiance simulations involving cirrus (using the MODTRAN model cirrus, ICLD = 18), and due to the numerously reported (P. Acharya 1999, personal communication) incorrect subroutines distributed with the UNIX version of MODTRAN 4, Version 1.1 (Beta), we chose to terminate the use of MODTRAN for this research.

## CHAPTER 4

### ALBEDO AND SOLAR FORCING COMPARISONS

#### Background

The initial plan for this research called for performing a forward calculation of GOES-observed radiances using the MODTRAN radiative transfer code and the retrieved cirrus properties of JM98. As described in Chapter 3, this was not possible due to the problems encountered with MODTRAN. Additional top of the atmosphere (TOA) information beyond the observed radiances are available, however, in the form of albedos derived by the technique of Minnis et al. (1998). Even though the broadband shortwave albedo is a fundamental quantity in the earth's radiation budget, the values reported by Minnis et al. are derived from a sophisticated narrowband-broadband, narrow field of view-hemispheric field of view conversion algorithm. The decision to initially compare the calculated and observed radiances was done to avoid the inevitable uncertainty of knowing which product was responsible for differences between the two. However, as shown in this section, there appears to be little ambiguity in the albedo comparisons that cannot be explained by known shortcomings of both the surface and TOA techniques.

In order to move toward closure on the column radiation budget, and as an additional source of validation, comparisons between the observed and the calculated downwelling surface fluxes are also examined. In order to avoid ambiguity due to unknown calibration offsets and aerosol amounts, the actual fluxes are not compared. Instead, we use the transmission ratio ( $T_r$ ), which is given as

$$T_r = \frac{F_{CLR} - F_{CLDY}}{F_{CLR}} \quad (13)$$

where  $F_{CLR}$  and  $F_{CLDY}$  are the clear-sky and cloudy-sky downwelling surface solar fluxes, respectively. To generate the calculated transmission ratio, the retrieved cirrus properties are used in FL93 to estimate the optical depth, asymmetry parameter, and single scattering albedo. These values are used in the radiative transfer model of Toon et al. (1989) as modified by Kato et al. (1997) to determine the calculated cloudy-sky transmission ratio. The calculated clear-sky flux is computed in a similar manner, with the cirrus layer removed. The observed downwelling cloudy-sky fluxes are taken from the baseline surface radiation network (BSRN) hemispheric flux observations. The observed clear-sky flux is somewhat more problematical. Due to unknowns, such as aerosol amounts and calibration offsets (Kato et al. 1997), the calculated clear-sky flux can not be used for the observed clear-sky flux. Long (1995) describes a technique that uses the observed pyranometer data in clear skies to fit a curve to the clear sky data. The curve fit is continuously updated with clear sky information and is thus able to track the combined effect of calibration offsets and aerosol concentrations. Therefore, we use the estimated observed clear-sky flux as derived from the Long (1995) estimation.

In the following pages, the techniques used to derived the TOA albedos from the satellite-observed radiances and the JM98 retrievals are described in greater detail. The results of the comparisons are provided, and two in-depth case studies are presented. Finally, we attempt to determine if this research sheds any light on the controversial topic of anomalous absorption of solar radiation in cloudy atmospheres.

### The “Observed” Albedo

The interpretation of satellite-observed radiances to determine a cloud’s optical depth and effective particle size requires radiative transfer calculations relating these parameters to the cloud’s reflectance, transmittance, and emittance (Minnis et al. 1998). Hence, the radiative transfer model provides the critical link between the satellite-observed radiance and a cloud’s microphysical properties (and, ultimately, its impact on the radiation budget). Unfortunately, these radiative transfer calculations can be computationally intensive and quite time consuming. Therefore, effective parameterizations are required to efficiently and accurately estimate a cloud’s microphysical composition from satellite observations. One such parameterization is based upon Minnis et al. (1993a), Minnis et al. (1995), and Minnis et al. (1998). The parameterization will be referred to hereinafter as PM98.

The PM98 parameterization employs lookup tables for cloud reflectance ( $\rho_c$ ) and cloud effective emittance ( $\epsilon$ ) computed from an adding-doubling radiative transfer code for plane-parallel atmospheres (e.g., Minnis et al. 1993a). Given a cloud’s optical depth (determined by PM98 through an iterative process), the solar zenith angle ( $\theta_o$ ), satellite viewing zenith angle ( $\theta$ ), and relative azimuth angle ( $\psi$ ), PM98 determines the cloud reflectance by interpolating between the values in these lookup tables. According to Minnis et al. (1998), the directional albedo ( $\alpha(\mu_o)$ ) is calculated by integrating  $\rho_c$  over  $\theta$ , and the diffuse albedo ( $\alpha_d$ ) is derived by integrating  $\alpha(\mu_o)$  over  $\theta_o$ . The shortwave broadband albedos are total albedos, which include both direct (single scattered) and diffuse (multiple scattered) radiation components. These shortwave broadband albedos are computed empirically using a regression formula derived from correlating TOA

narrowband albedos with TOA broadband albedos determined during the Earth Radiation Budget Experiment (ERBE) (e.g., Minnis et al. 1995). The narrowband albedos are derived from the directional reflectance by applying an anisotropic correction factor which depends on the solar and viewing geometry.

The data used to compute these quantities are collected from a  $0.9^\circ \times 0.9^\circ$  grid centered over the SGP CART site. The central  $0.3^\circ \times 0.3^\circ$  grid box is located directly over the ARM SGP site (Fig. 1, Minnis et al. 1995). According to Minnis et al. 1998, the parameterization is applicable over any low albedo surface, for clouds at any altitude. For cirrus clouds, PM98 is valid for distributions of randomly oriented hexagonal crystals with effective diameters varying from 6 to 135  $\mu\text{m}$ . According to Minnis et al. (1998), this parameterization of reflectance is accurate to within  $\pm 9\%$ . However, they state that most of this error is confined to scattering angles near distinct features in the phase function. When this parameterization is constrained to only those angles useful in satellite retrievals, Minnis et al. (1998) show that the reflectance errors are reduced to approximately  $\pm 2\%$ . Additionally, Minnis et al. (1995) show that the overall uncertainty in the derived shortwave broadband albedos is 10.9%.

#### The “Calculated” Albedo

Using the radiative properties derived from the JM98 retrieval algorithm, the downwelling and upwelling solar fluxes were calculated by the RAPRAD radiative transfer model (Toon et al. 1989). In all of the RAPRAD calculations, the surface albedo was set to 0.2 (20%), for all scattering angles. This value was based on surface albedos derived from upward and downward-looking broadband radiometers located at the SGP site. The solar fluxes were calculated at 250-meter increments (in the vertical), with a

maximum altitude of 16 km. The use of 16 km as the TOA was done to minimize computational efforts. However, the validity of using the 16 km calculated flux to approximate the TOA flux is not without question. Although approximately 90% of the earth's atmosphere is contained below 16 km (Ahrens 1994), the TOA is usually taken to be at or near 100 km for radiative transfer purposes. In order to determine how much error is introduced by using 16 km, and the associated calculated fluxes for this altitude as the proxy TOA, comparisons were made between the flux values calculated by RAPRAD and those calculated by another radiative transfer model -- the Santa Barbara DISORT Radiative Transfer Model (SBDART) (Richiazz et al. 1998).

The calculations performed by SBDART were accomplished via the code's internet interface (<http://arm.mrcsb.com/sbdart/>). The calculations employed cirrus clouds with optical depths ranging from  $\tau = 0.5$  to  $\tau = 5.0$ . Additionally, the calculations were performed at the SGP site's latitude and longitude for March, June, September, and December, for times ranging from 1400 to 2300 hours UTC. From these calculations it was determined that, on average, the downwelling solar flux at 100 km was approximately  $30 \text{ W/m}^2$  greater than the downwelling flux at 16 km, for all hours of the day, and for all seasons. The difference between the upwelling flux at 16 km and 100 km was negligible for all hours of the day, and for all seasons. As such,  $30 \text{ W/m}^2$  was added to all 16 km downwelling solar flux values calculated by RAPRAD. The 16 km upwelling fluxes were used without adjustment.

The TOA albedo was determined from the RAPRAD calculated fluxes by dividing the upwelling 16 km flux by the adjusted downwelling 16 km flux. Thus, the calculated solar albedo is given by

$$\text{TOA Solar Albedo(%)} = \left( \frac{\text{Upwelling 16 km Solar Flux}}{\text{Adjusted Downwelling 16 km Solar Flux}} \right) \times 100.0 \quad (14)$$

For consistency, the adjusted TOA downwelling solar flux was used in all subsequent comparisons (e.g., surface solar forcing comparisons) or quantities involving the RAPRAD calculated data (e.g., surface solar transmittance).

### Results

A major advantage of using data collected by the ARM program is that the instruments operate continuously. This continuous data stream is in sharp contrast to most other field data which is limited by operator and deployment schedules. Given the large variability in cirrus properties that have been observed (Liou 1986), the continuous data stream is required to sample the full spectrum of cirrus properties that occur naturally in the atmosphere. However, since this research is intercomparing satellite retrievals (PM98) with surface retrievals (JM98), the first requirement for the comparison is that both data sets exist. As mentioned previously, JM98 is being used operationally on the ARM data streams. Currently, PM98 is only being implemented during the ARM intensive observing periods (IOP); approximately 6 weeks per year. A second requirement for these comparisons is that the cirrus clouds had to exist over the MMCR and AERI instruments long enough for them to collect data. Since the MMCR has a (maximum) pulse repetition frequency of 20 kHz, with a maximum dwell time of 1.0 seconds, the observations taken with this instrument should not pose a problem. However, the dwell time for each AERI measurement is 3 minutes, with an observation taken once every 8 minutes. Another factor necessary to consider for these comparisons was the time of day. Given that the primary

quantity we are interested in is the cloud solar albedo (derived from the upwelling and downwelling TOA solar fluxes), the observations taken by the instruments at the SGP site (and by the GOES satellite) had to occur during daylight hours. Additionally, to avoid problems with extreme solar zenith angles, comparisons were limited to those times when the solar zenith angle was less than 70 degrees. As such, the number of days available for comparison were somewhat limited. However, there were enough days, over the full spectrum of the year, to provide us with a reasonable amount of data.

In the following sections we present two in-depth case studies of cirrus events for which both surface and TOA comparisons are possible. While the strength of the ARM data set is in long-term statistical composites (demonstrated later in this chapter), detailed examination of individual cases are still a valuable tool for process oriented studies and algorithm comparison. The two cases examined, 24 March 1997 and 27 May 1998, represent two distinct classes of cirrus. The 24 March case was primarily associated with a transient mid-latitude cyclone, thus deriving its dynamic forcing ultimately from the synoptic scale. The 27 May event, by contrast, was associated with convective outflow from a mesoscale convective complex in Texas. Therefore, in the second case, the formation and maintenance of the cirrus is a result more from mesoscale and lower tropospheric sources.

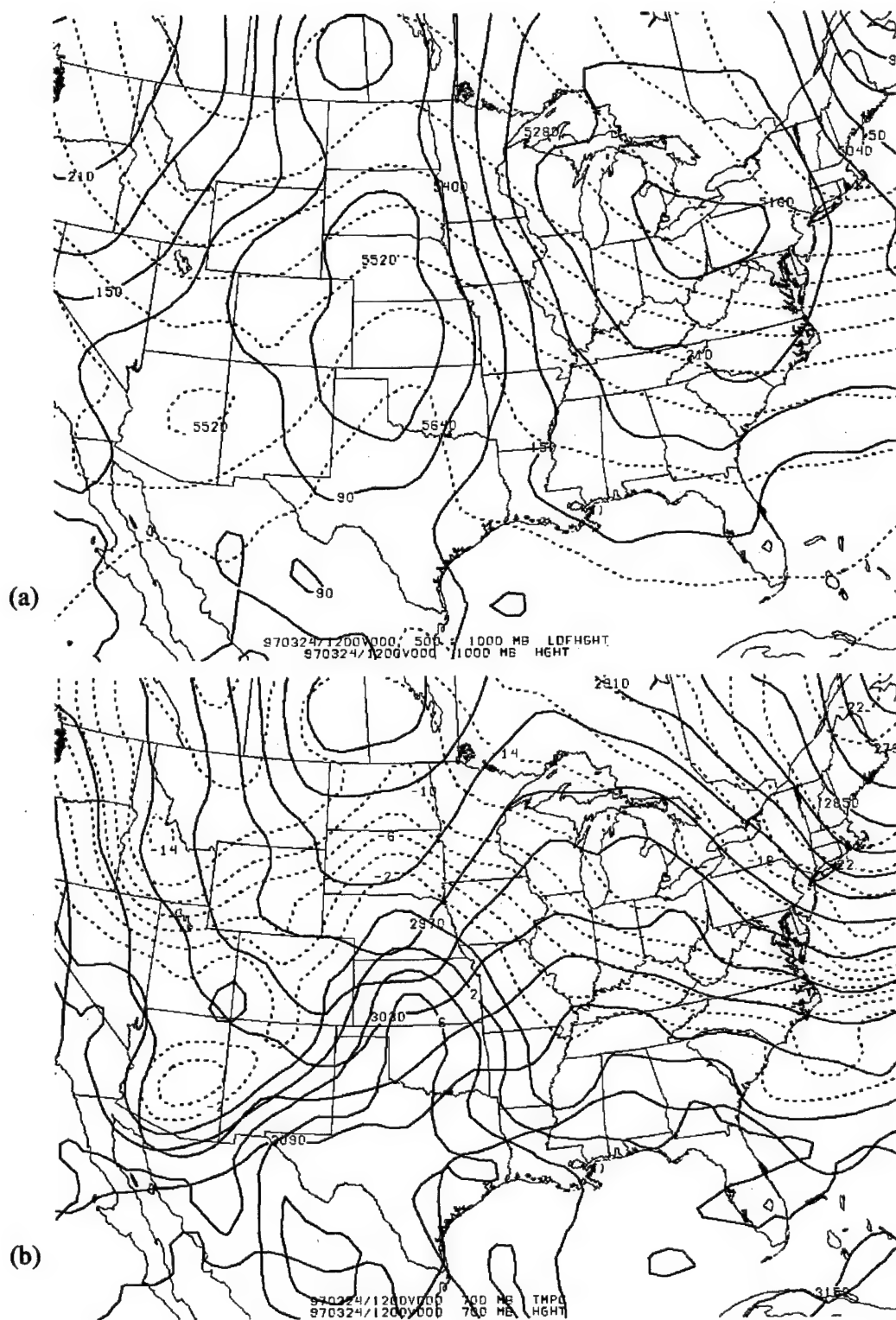
#### 24 March 1997

The 24 March 1997 cirrus case occurred in conjunction with an upstream developing synoptic scale system. The National Center for Environmental Prediction's (NCEP) ETA model 1000 mb, 700 mb, 500 mb, and 300 mb analyses and the GOES 8 infrared satellite image for 24/12Z are shown in Figs. 11 and 12, respectively.

At the surface, a broad area of low pressure stretches over the Great Plains of the United States at 12Z, on the 24th of March 1997; see Fig. 11(a). This trough of low pressure separates the two air masses located over the northeastern and northwestern portions of the country. The associated baroclinic zone is evident from the 700 mb thermal gradient; Fig. 11(b). From Figs. 11(b) through 11(d), the longwave trough can be seen to slant westward with height, in classic fashion. At 500 mb (Fig. 11(c)), a shortwave vorticity maximum can be seen moving through the base of the longwave trough, approximately over southwest Arizona. Another vorticity maxima can be seen moving southward along the backside of the longwave trough, over eastern Idaho. The 300 mb heights and wind speed (Fig. 11(d)) show a weak upper-level ridge located over the central U.S., with the ridge axis over the SGP site. Cirrus can be seen in association with the ridge in the corresponding 12Z infrared satellite image; see Fig. 12. Also, a northwesterly jet streak can be seen (Fig. 11(d)) west of the longwave trough axis, with core winds in excess of 100 knots (50 m/s).

With the aforementioned meteorological conditions in place, it can be expected that the longwave trough will deepen due to the cold air advection and the jet maxima entering the west side of the trough. In association with the deepening trough, and as a result of the vorticity advection from the shortwave impulses moving through the longwave trough, cyclogenesis (or intensification of the pre-existing surface low) can be expected. Additionally, using Meeker's Method for forecasting longwave trough movement (Elliot 1988), the trough can be expected to deepen southward over the intermountain-west, while simultaneously translating slowly eastward over the next 12 to 24 hours. The cyclogenesis is shown in the NCEP ETA 1000 mb and 700 mb analyses

FIG. 11. NCEP ETA model analysis for 12Z, 24 March 1997: (a) 1000 mb height and 1000-500 mb thickness, (b) 700 mb height/temperatures, (c) 500 mb height/vorticity, and (d) 300 mb height/wind speed.



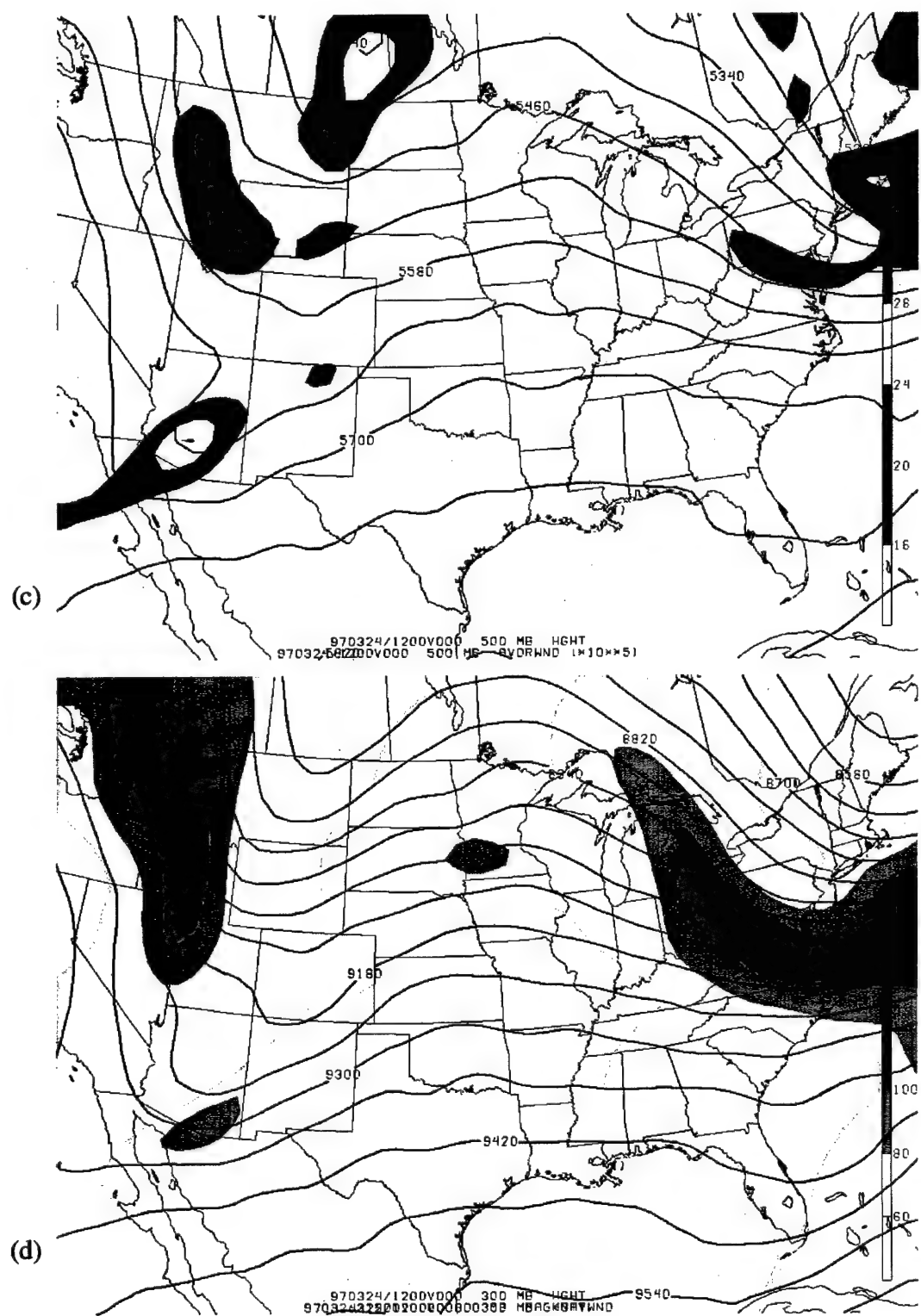


FIG. 11. Continued

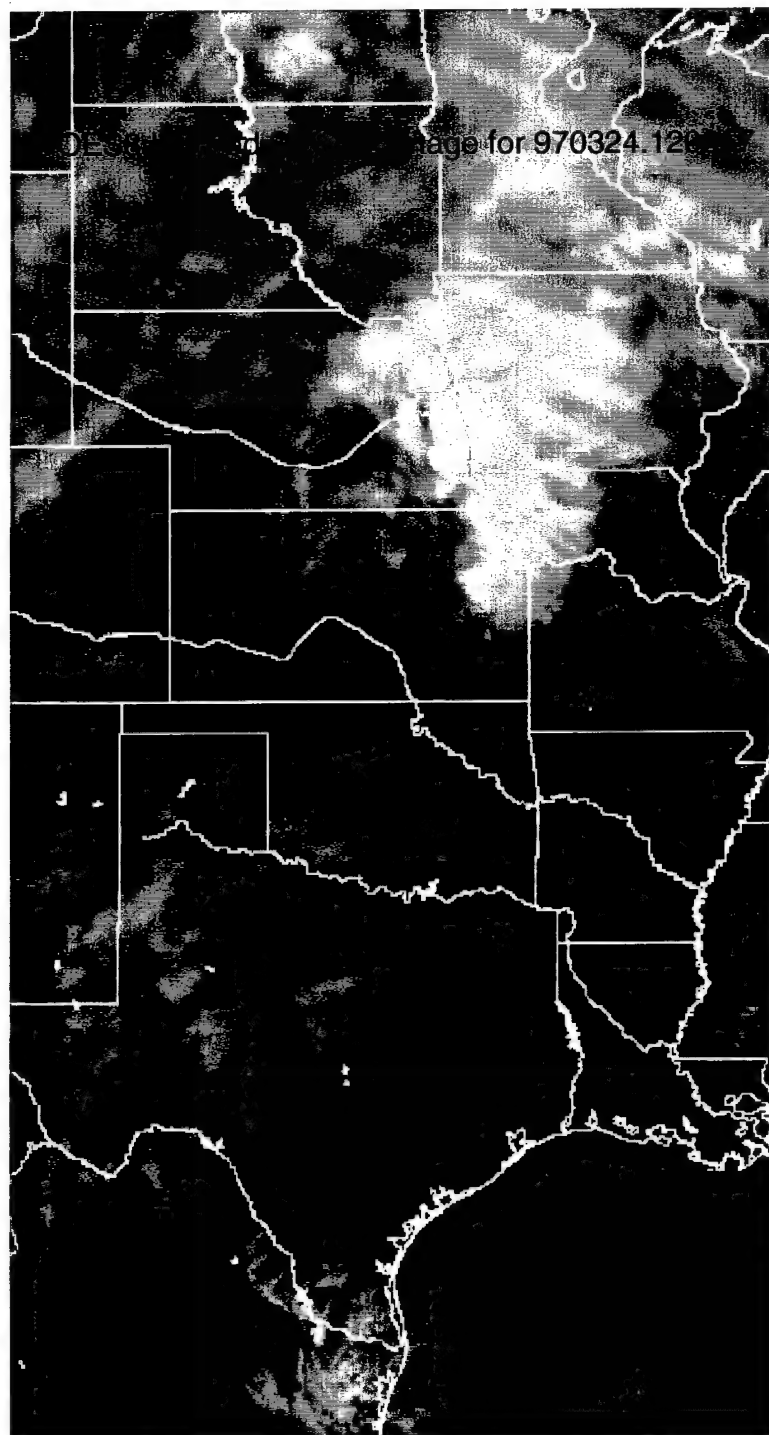


FIG. 12. GOES 8 infrared satellite image for the ARM SGP CART site, 24 March 1997 cirrus case. The time of this image is 1208 Zulu.

(Figs. 13(a) and 13(b), respectively) for 00Z, 25 March 1997. The developing surface low and associated frontal boundary can be seen, in Fig. 13(a), stretching from southeastern Kansas, southwestward through the Oklahoma and Texas panhandles, into eastern New Mexico. Figure 13(b) displays an intensification in the 700 mb thermal gradient associated with this cyclogenesis. At 300 mb, Fig. 13(d), the amplification and easterly movement of the wave can be readily identified. Further, the developing frontal boundary can be identified in the infrared satellite image from 23Z, on 24 March 97; see Fig. 14.

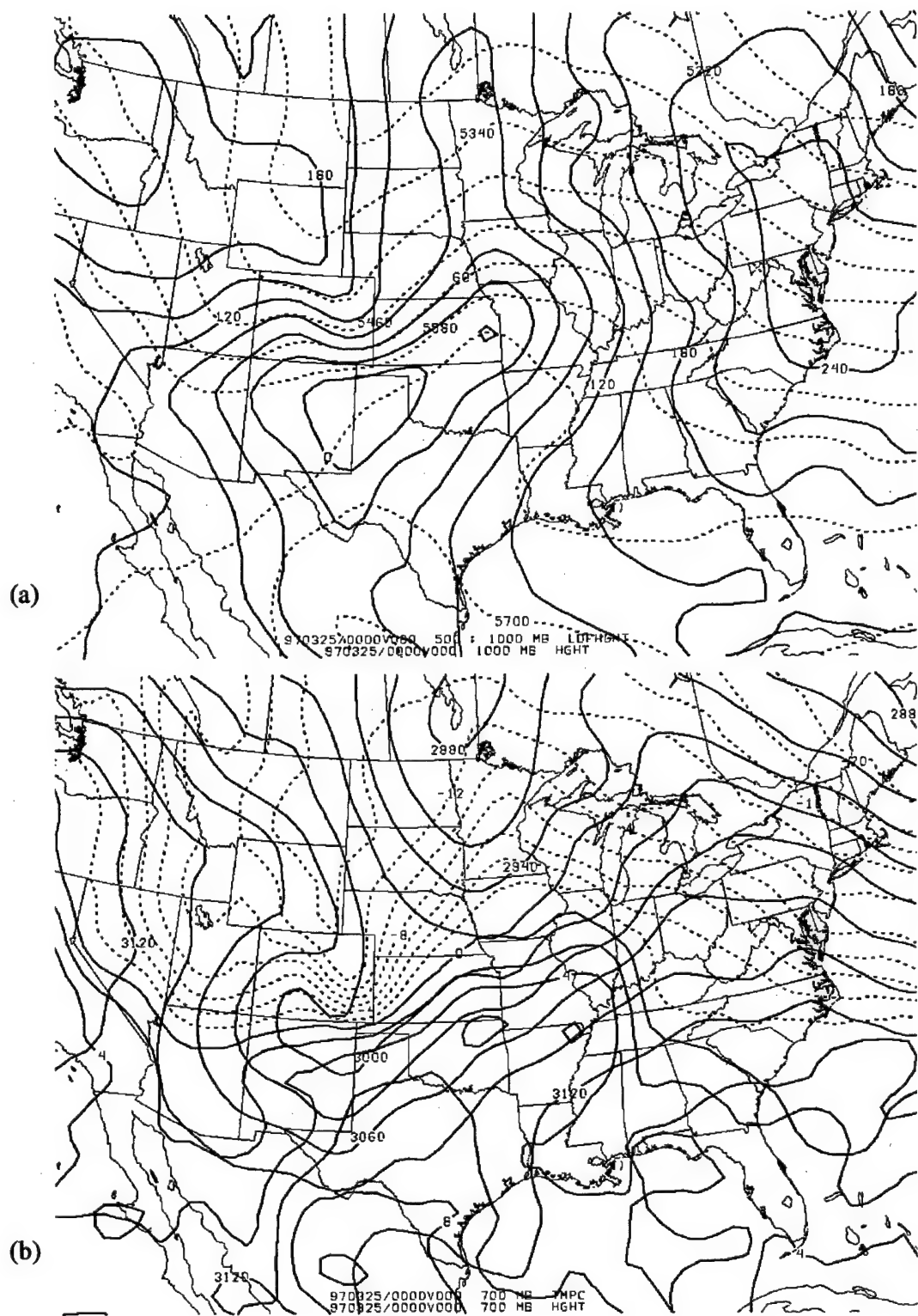
In conjunction with the deepening middle-latitude cyclone, the cirrus that advected over the SGP site became progressively thicker throughout the day. This is readily seen from the satellite images and in the MMCR radar reflectivity (Fig. 15(a)). As seen in the radar reflectivity, the cloud base at 12Z was located near 10 km, while the ragged radar-observed cloud top<sup>1</sup> was located near 11 km. However, as the day progressed the layer thickness increased to approximately 3 km. In association with this increasing cloud thickness, the height of the cloud top and base also lowered to approximately 10 km and 7 km, respectively. Further the corresponding MMCR reflectivity values rose from approximately -40 dBZe to near -10 dBZe.

The cirrus microphysical properties derived from the JM98 algorithm can be seen in Figs. 15(b) through 15(d). As seen in Fig. 15(b), the IWC of the cloud increased from an average of  $5 \text{ mg/m}^3$  during the period from 12 to 16Z, to an average of  $30 \text{ mg/m}^3$  during the latter part of the day. An increase in effective radius, from approximately  $20 \mu\text{m}$  to  $70 \mu\text{m}$ , and a decrease in particle concentration, from an average of  $150 \text{ liter}^{-1}$  to 60

---

1. Hereinafter when referring to radar-observed cloud tops, the qualifier "radar-observed" will be omitted for brevity. It is understood that millimeter-wavelength radars have some difficulty sensing the tenuous upper reaches of cirrus layers, and that the radar-observed cloud top may, therefore, be biased low.

FIG. 13. NCEP ETA model analysis for 00Z, 25 March 1997: (a) 1000 mb height and 1000-500 mb thickness, (b) 700 mb height/temperatures, (c) 500 mb height/vorticity, and (d) 300 mb height/wind speed.



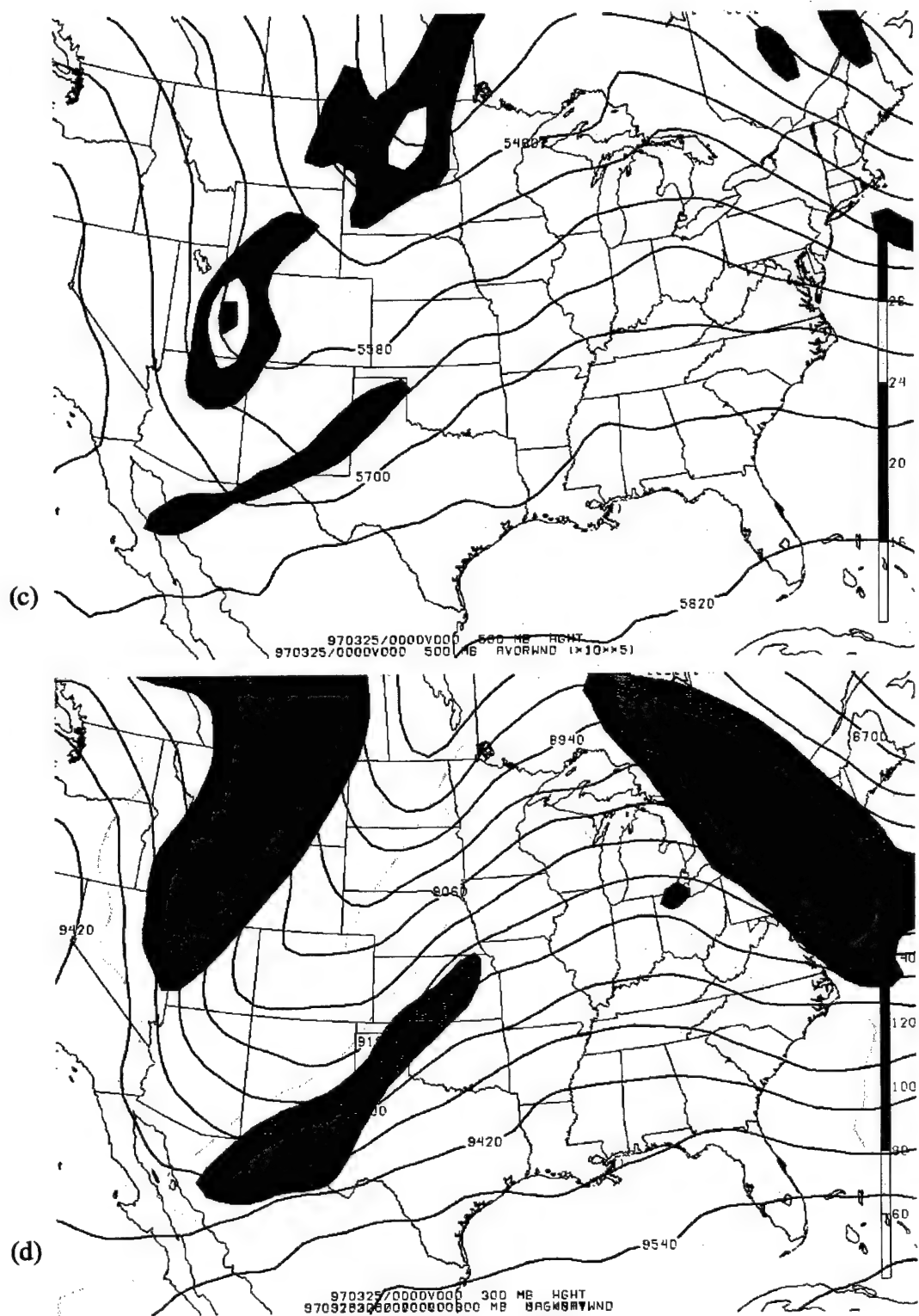


FIG. 13. Continued

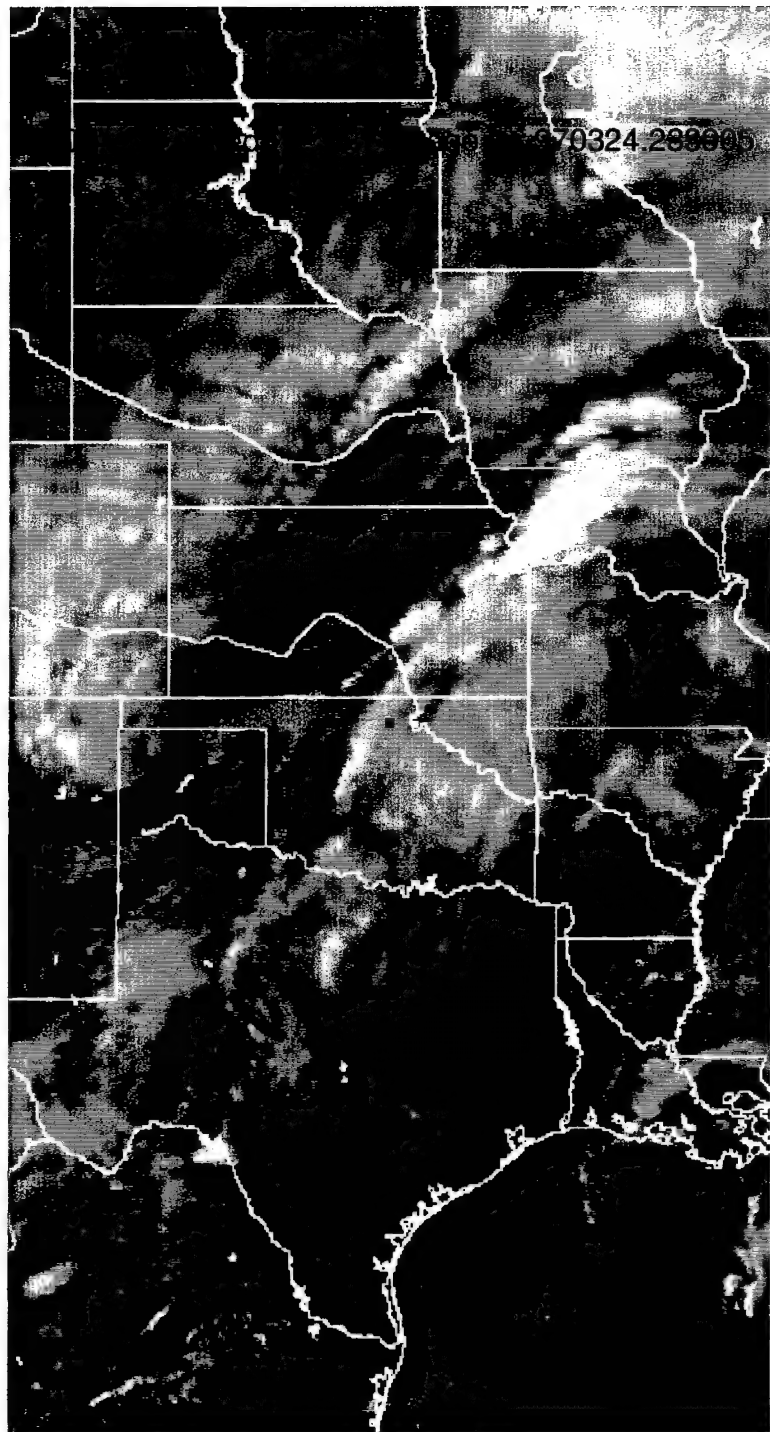
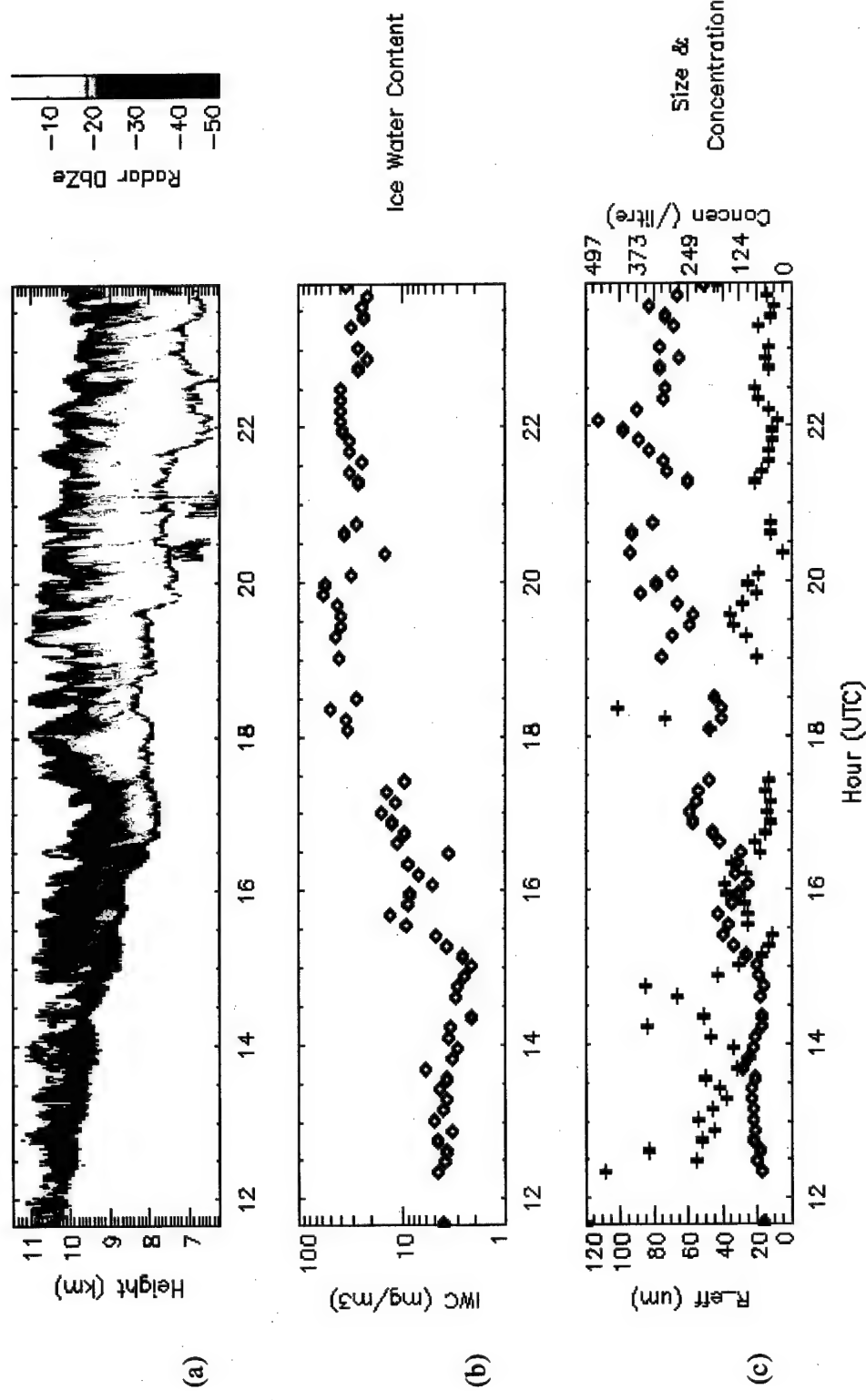


FIG. 14. GOES 8 infrared satellite image for the ARM SGP CART site, 24 March 1997 cirrus case. The time of this image is 2339 Zulu.

FIG. 15. JM98 retrieved, layer-averaged cirrus cloud properties for 24 March 1997 at the ARM SGP CART site for (a) radar reflectivity, (b) ice water content, (c) particle effective radius and concentration, (d) layer emittance and visible optical depth, and (e) solar forcing - fraction of clear-sky flux removed by cloud.

Cirrus Cloud Properties 24 March 1997 SGP CART Site  
 Reflectivity Radiance Algorithm



Cirrus Cloud Properties 24 March 1997 SGP CART Site

Reflectivity Radiance Algorithm

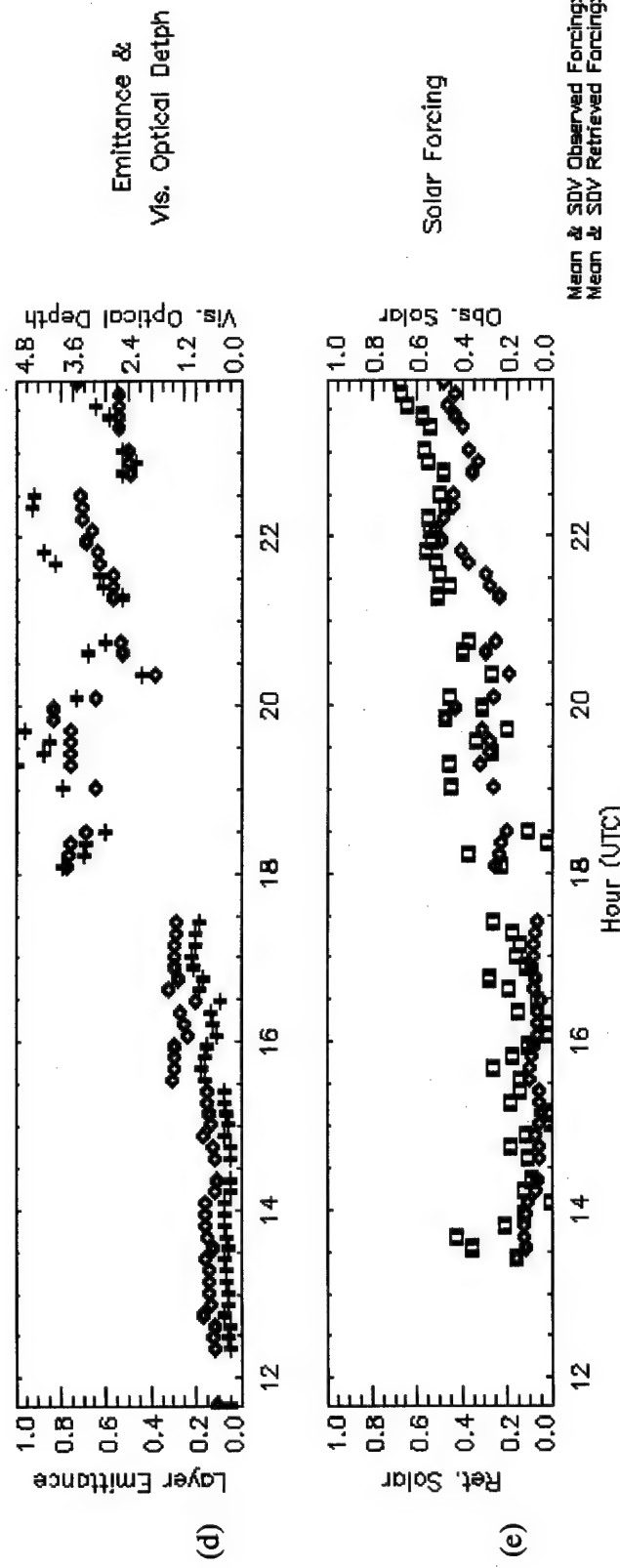


FIG. 15. Continued

liter<sup>-1</sup>, is shown in Fig. 15(c), for these same time periods. Finally, Fig. 15(d) displays the visible optical depth of the cloud. The optical depth was calculated using equation (11) and the radiative properties derived from FL93. As with the IWC and particle size, the visible optical depth showed little variance from 12 to 16Z. The average value for this period (from inspection of Fig. 15(d)) is  $\tau \leq 0.25$ . However, after 18Z, the visible optical depth showed a marked increase in magnitude and variability to  $2.4 \leq \tau \leq 4.8$ .

To understand where this cirrus event lies within the continuum of naturally occurring cirrus, the microphysical properties presented above were compared to layer-mean temperature dependent cirrus statistics. The layer-mean temperature dependent statistics are given in Tables 3 and 4, for the cold (November through April) and warm (April through October) seasons. These statistics were compiled from observations taken during the months of November 1996 through October 1997 (G. Mace 1999, personal correspondence). The ice water path (IWP), given in Tables 3 and 4, can be estimated by multiplying the average IWC by the cloud thickness (e.g., equation (6) of Mace et al. 1998a).

In comparison with the cold season layer-mean quantities, the 24 March 1997 JM98 derived cirrus IWP (5 g/m<sup>2</sup>), effective radius ( $r_e \sim 20 \mu\text{m}$ ), and particle concentration (150 liter<sup>-1</sup>), for the period from 12 to 16Z, are very nearly equal to the average values found the coldest 1/3 of cirrus events. Remembering that the cirrus observed at the SGP site for this time period had an average mid-cloud height near 10.5 km, the temperature of the cloud can be inferred from the atmospheric temperature profile (Fig. 16) to be approximately 215 K. However, for the latter part of the day, as the cloud thickness increased and cloud height lowered, the concentration ( $\sim 60 \text{ liter}^{-1}$ ) and  $r_e$  ( $\sim 70$

TABLE 3. Layer-Mean Cirrus Properties for Cold Season November 1996 to April 1997.

	Coldest 1/3 Cirrus	Middle 1/3 Cirrus	Warmest 1/3 Cirrus
Ice Water Path (g/m <sup>2</sup> )	5.3	7.6	12.6
Concentration (liter <sup>-1</sup> )	133	86	52

TABLE 4. Layer-Mean Cirrus Properties for Warm Season April to October 1997.

	Coldest 1/3 Cirrus	Middle 1/3 Cirrus	Warmest 1/3 Cirrus
Ice Water Path (g/m <sup>2</sup> )	5.0	10.5	10.6
Concentration (liter <sup>-1</sup> )	104	97	81

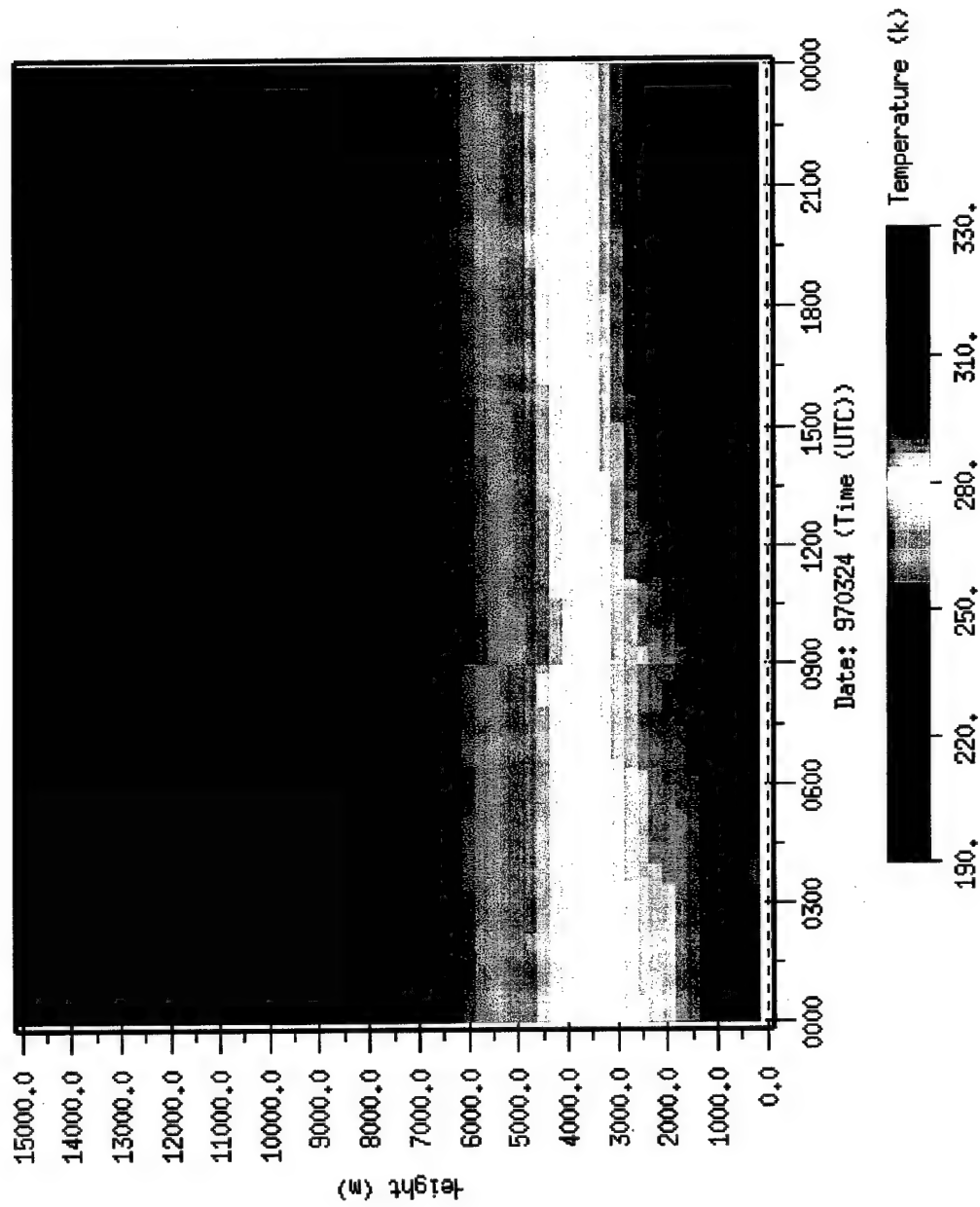


FIG. 16. Atmospheric temperature profile at the ARM SGP CART site derived from a radiosonde sounding for 24 March 1997.

$\mu\text{m}$ ) more closely match those found in the warmest 1/3 of cirrus clouds. The IWP for this same time period is relatively high; on the order of four times the magnitude of the average value found in the warmest 1/3 of cirrus clouds in the cold season. The mean-cloud height for this thicker cirrus observed during the latter part of the day was approximately 8.5 km. As such, the inferred cloud temperature is approximately 235 K; see Fig. 16. Thus, through comparison with the cold season cirrus statistics, the JM98 results suggest that the cirrus observed on 24 March 1997 lie very near the average cirrus cloud properties found during the cold season. With the underlying meteorological conditions known for this cirrus event, as well as its place within the continuum of cold season cirrus, we next present the albedo comparison for 24 March 1997.

The albedo comparison for 24 March 1997 is shown in Fig. 17(a). The albedos calculated from the RAPRAD solar fluxes derived from the JM98 algorithm retrievals (indicated by the blue asterisks and labeled as Mace) show good agreement with the satellite derived shortwave broadband albedos (indicated by the black diamonds and labeled as Minnis). The mean satellite (PM98) derived albedo for the time period shown is 31.39%. The mean albedo calculated from the JM98 retrievals is 29.27%. Equally encouraging, is the nearly identical trend of the two albedos, which capture well the evolving nature of the cirrus layer. Toward the latter part of the comparison, near 22-23Z, the magnitudes of the two albedos begin to differ. The average difference in albedos for this time period is on the order of 10%. One possibility for this error could be due to the increasing solar zenith angles found at this time of the day, and the adverse effects large solar zenith angles have on visible satellite observations. Another possible cause for this discrepancy could arise from the JM98 algorithm's adjustment for the bulk density of ice;

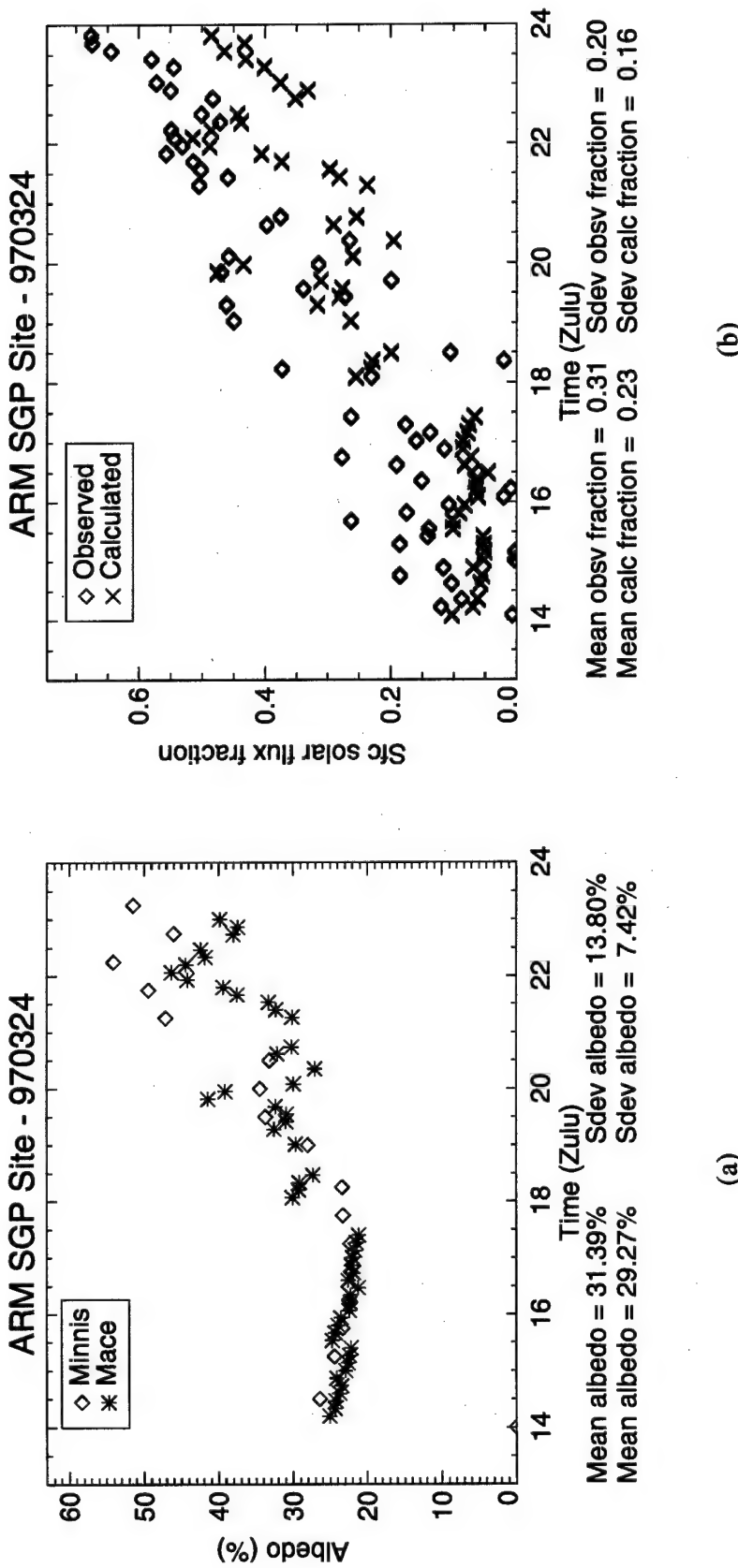


FIG. 17. Comparisons for the 24 March 1997 cirrus case at the ARM SGP CART site for (a) TOA solar albedo(%), and (b) surface solar forcing expressed as the fraction of the clear-sky flux removed by cloud.

which is dependent on the particle size. With JM98 particle sizes in the range of 60  $\mu\text{m}$  to 80  $\mu\text{m}$ , the JM98 algorithm would infer a particle density less than that used in the PM98 parameterization, since PM98 assumes solid ice crystals. The two algorithms should sense the same amount of ice mass, but the distribution of this mass is handled differently. Additionally, the difference between the albedos could be due to the insensitivity of the JM98 algorithm to the smaller particles found near the top of the cloud; which are strong light scatters. If the small particles located in the low-reflectivity regions near the actual cloud top were below the detection threshold of the radar, the total ice mass in the column derived by the JM98 algorithm may be underpredicted and, thus, result in the lower albedos. Despite the differences in the magnitudes of the albedos found near the end of the comparison, the overall agreement between the albedos derived by the two techniques is quite encouraging.

If the JM98 retrieved cloud properties result in TOA albedos (fluxes) that compare well with albedos derived from satellite observed TOA radiances *and* lead to reasonable estimates in the solar flux at the surface, we can be reasonably assured that the algorithm has attained a sufficient level of accuracy to evaluate the influence of the cirrus layer on the radiation budget. To this end, the surface solar flux fraction comparison of Fig. 17(b) is presented. In this plot, the surface fluxes are represented as the fraction of the clear-sky flux removed by the cloud. From this comparison, we find reasonably good agreement between the observed and calculated fractions, in both trend and magnitude. Still, there does appear to be an overall bias for the calculated flux fractions to be lower than observed. It is true that the horizontal heterogeneity of the cloud may cause significant differences between the observed flux and the calculated flux. However, horizontal

heterogeneity probably would not lead to a bias, but rather would produce scatter in the differences between the two values. Other possible sources for the bias could be: 1) An incorrect asymmetry parameter (in this case  $\bar{g} = 0.818 \pm 0.0203$ ); the FL93 values of the asymmetry parameter assume randomly-oriented hexagonal columns. Observations and recent theoretical studies (e.g., Kinne et al. 1992) suggest that significantly lower values for the asymmetry parameter may be more appropriate. 2) An incorrect treatment of the infrared radiative properties of small ice crystals; the FL93 parameterization bases the infrared properties of these small ice crystals on assumed spheres using Mie calculations. Recent work by Fu et al. (1998) show that Mie theory significantly overestimates the extinction efficiency of small ice crystals. Thus, the JM98 algorithm would underestimate the IWP and thereby result in lower than observed flux fractions. 3) An incorrect observed clear-sky flux derived from the technique of Long (1995). In essence, no clear sky occurred on this particular day. Therefore, the clear-sky fit must be the result of some previous or later day's observations. This could lead to error if the aerosol loading of the day used to generate the fit was higher than the day in question.

While the exact cause of the error for this case is unknown, it can be stated with some measure of confidence that, for the most part, the essential elements of this rather typical synoptic scale event were captured by the surface and satellite based retrieval algorithms.

#### 27 May 1998

Where conditions are favorable for convection, a number of individual thunderstorms will occasionally grow in size and organize into a large convective weather system (Ahrens 1994). In fact, these convective systems can cover an area in excess of  $10^5$

$\text{km}^2$  (Barry and Chorley 1990), possibly encompassing an entire state. In special cases, these convectively driven systems work together to generate a relatively slow moving, long-lasting weather phenomena known as a mesoscale convective complex (MCC) (Ahrens 1994).

The 27 May 1998 cirrus case occurred in conjunction with a decaying MCC moving across Texas. At 06Z, on 27 May 1998, the GOES 8 infrared satellite image (Fig. 18) clearly shows a system that could possibly qualify as an MCC; based on the aerial coverage and convective nature of the system. The cirrus anvil from the MCC covers a large portion of central Texas and southern Oklahoma. The system initially formed in southwest Texas, late on the previous day, and was a result of, among many other components, southerly surface winds advecting warm, moist air from the Gulf of Mexico, northward over Texas, and moderate vertical (directional) wind shear. This situation is clearly shown in the NCEP ETA model 1000 mb and 500 mb analyses displayed in Figs. 19(a) and 19(b), respectively. In the southeast U.S., a ridge axis associated with a large anticyclone centered over the middle Atlantic Ocean (also known as the Bermuda High) can be seen extending over Florida, westward into eastern Texas; see Fig. 19(a). The resulting south to north oriented 1000 mb height contours (over Texas) are indicative of the aforementioned southerly wind. This warm, moist air is the fuel that drives the convective system. At 500 mb, Fig. 19(b), the southwest to northeast oriented height contours would result in a southwesterly wind. The directional shear of the wind with height, helps keep the system alive. Also at 500 mb, a vorticity maxima and shortwave trough in the 5820 meter isohypse are analyzed as a result of the existence of the MCC.

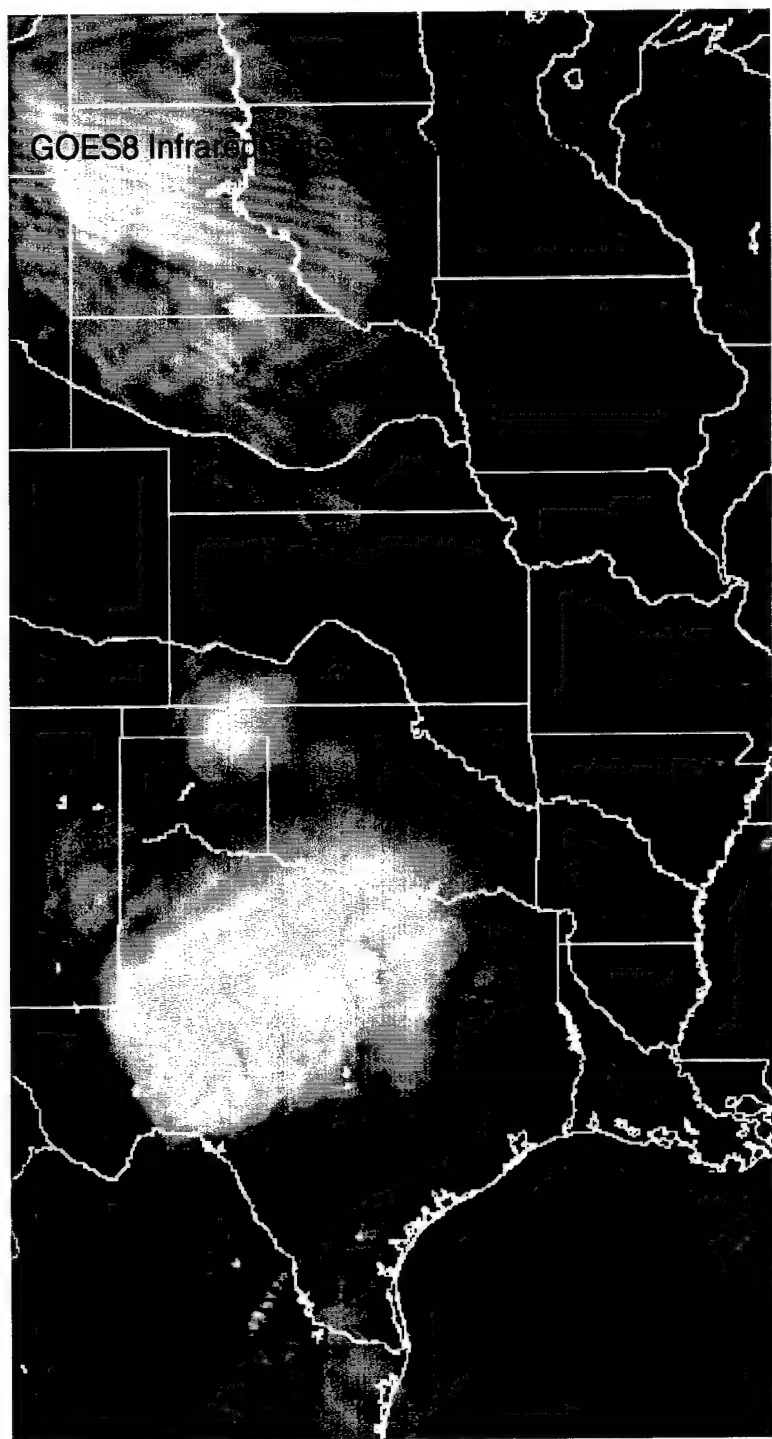
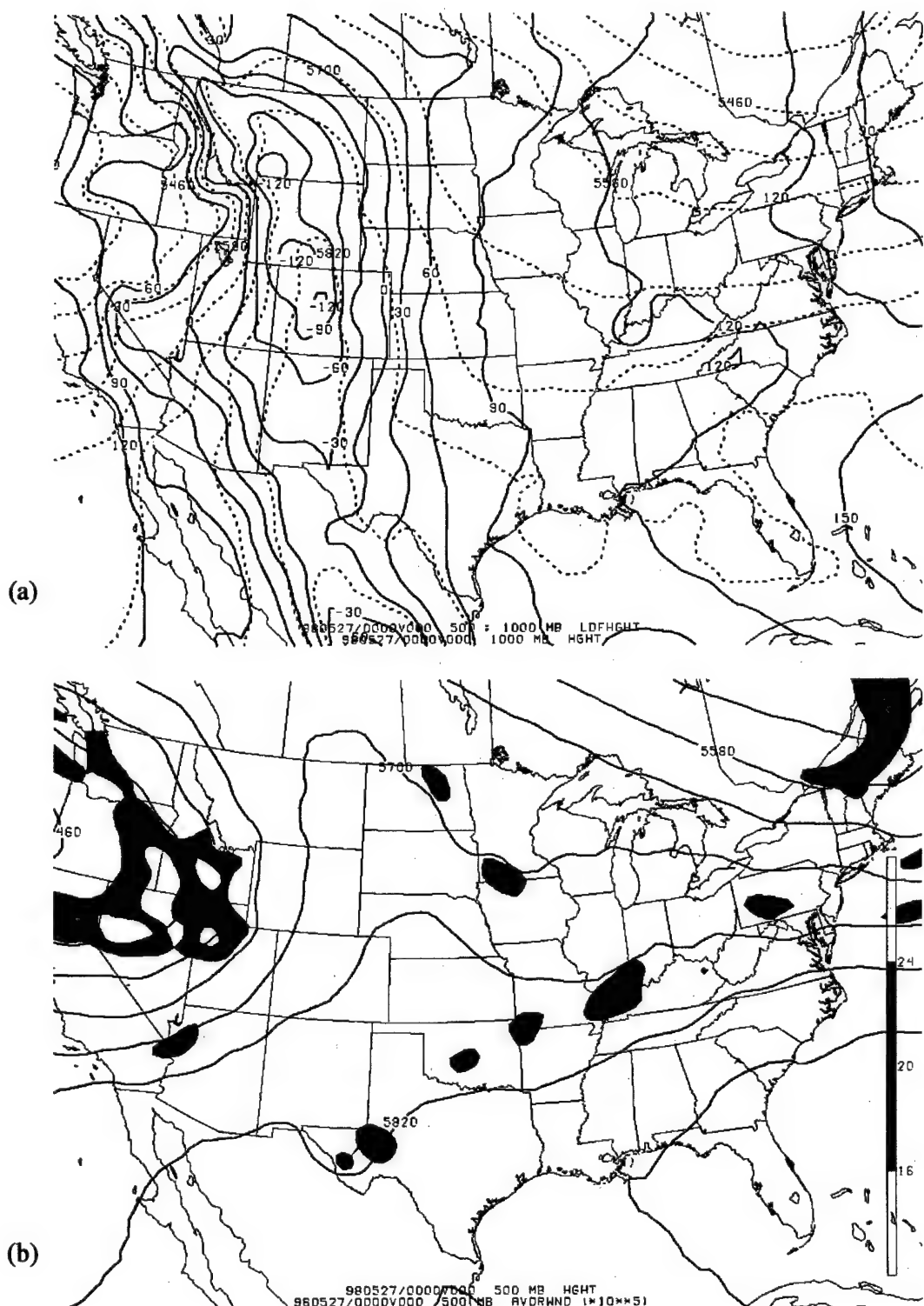


FIG. 18. GOES 8 infrared satellite image for the ARM SGP CART site, 27 May 1998 cirrus case. The time of this image is 0608 Zulu.

FIG. 19. NCEP ETA model analysis for 00Z, 27 May 1998: (a) 1000 mb height and 1000-500 mb thickness, and (b) 500 mb height/vorticity.



By 12Z on the 27th of May, the MCC is clearly in the dissipating stage of its life cycle; as shown in the corresponding GOES 8 infrared satellite image (Fig. 20). The majority of the active convective cells are dead, except for the few remaining cells in northeastern Texas and southwestern Arkansas. The large, very cold cirrus anvil seen in the 06Z infrared satellite image (Fig. 18) has become less coherent and warmed (as evident from the darker pixels in Fig. 20). Throughout the remainder of the day, the MCC continued to dissipate and translate in an east-northeasterly direction. By 23Z, the remnants of the MCC are now located on the Texas-Arkansas border; see Fig. 21. The few remaining clustered convective cells can no longer be considered an MCC. However, the decaying cirrus anvil from the former MCC can still be seen advecting over the ARM SGP CART site.

The cirrus anvil of the MCC originally began to advect over the SGP site shortly after 06Z, and continued to advect over the site for the remainder of the day. The anvil cirrus' microphysical properties derived from the JM98 algorithm can be viewed in Figs 22(a) through 22(d). Initially, as seen from the MMCR reflectivity (Fig. 22(a)) and the GOES 8 visible satellite image (Fig. 23), the cirrus seen at the SGP site was quite stratiform in nature. For the period from 12Z to 15Z, the height of the average radar-observed cloud base and cloud top were 9.5 km and 12 km, respectively. However, as the day waned and the MCC dissipated, the advecting cirrus became more patchy. In fact, as seen in Fig. 22(a), the radar reflectivity would suggest that the decaying cirrus also became multilayered. The lower cloud elements had radar-observed bases near 9.5 km and tops near 10.5 km. The very thin, very low reflective upper layer was located near 12 km.

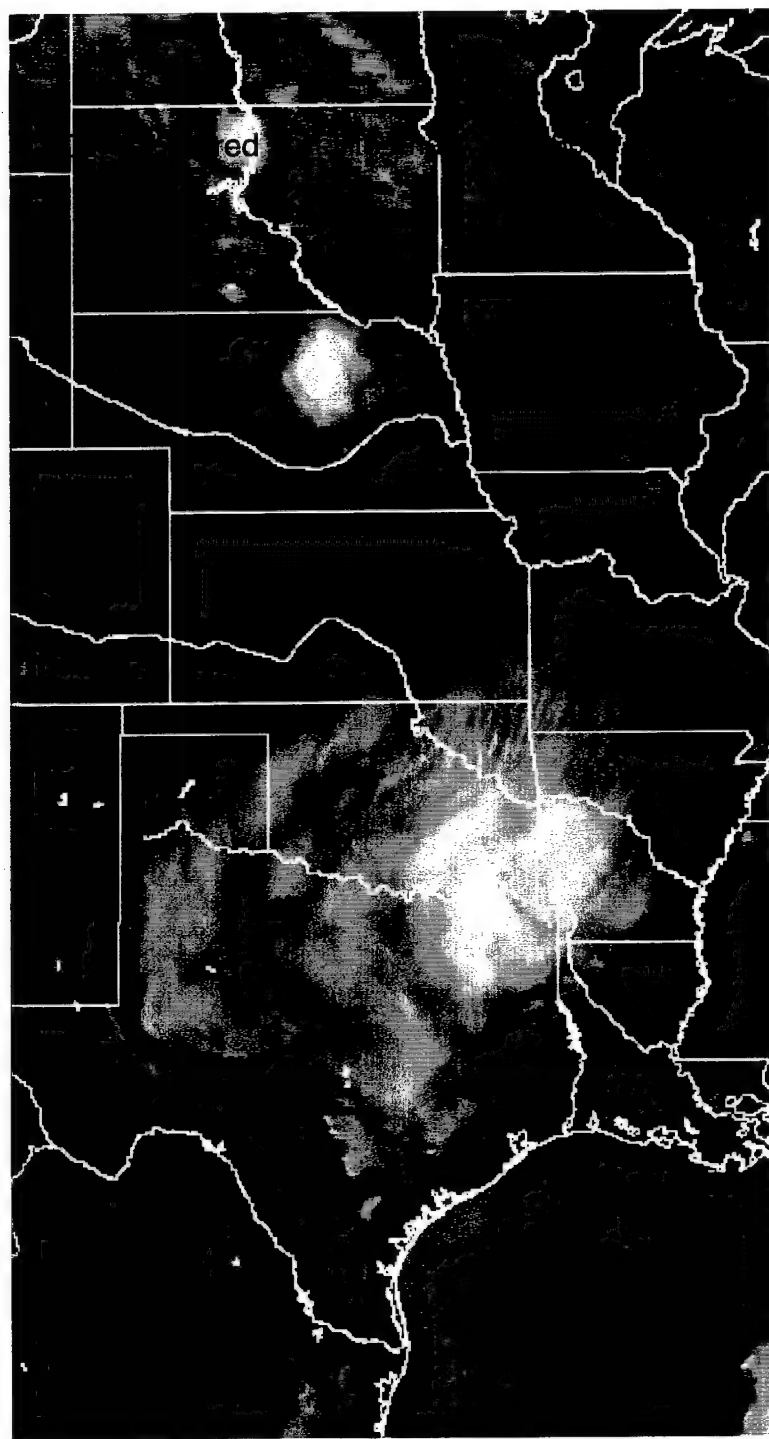


FIG. 20. GOES 8 infrared satellite image for the ARM SGP CART site, 27 May 1998 cirrus case. The time of this image is 1209 Zulu.

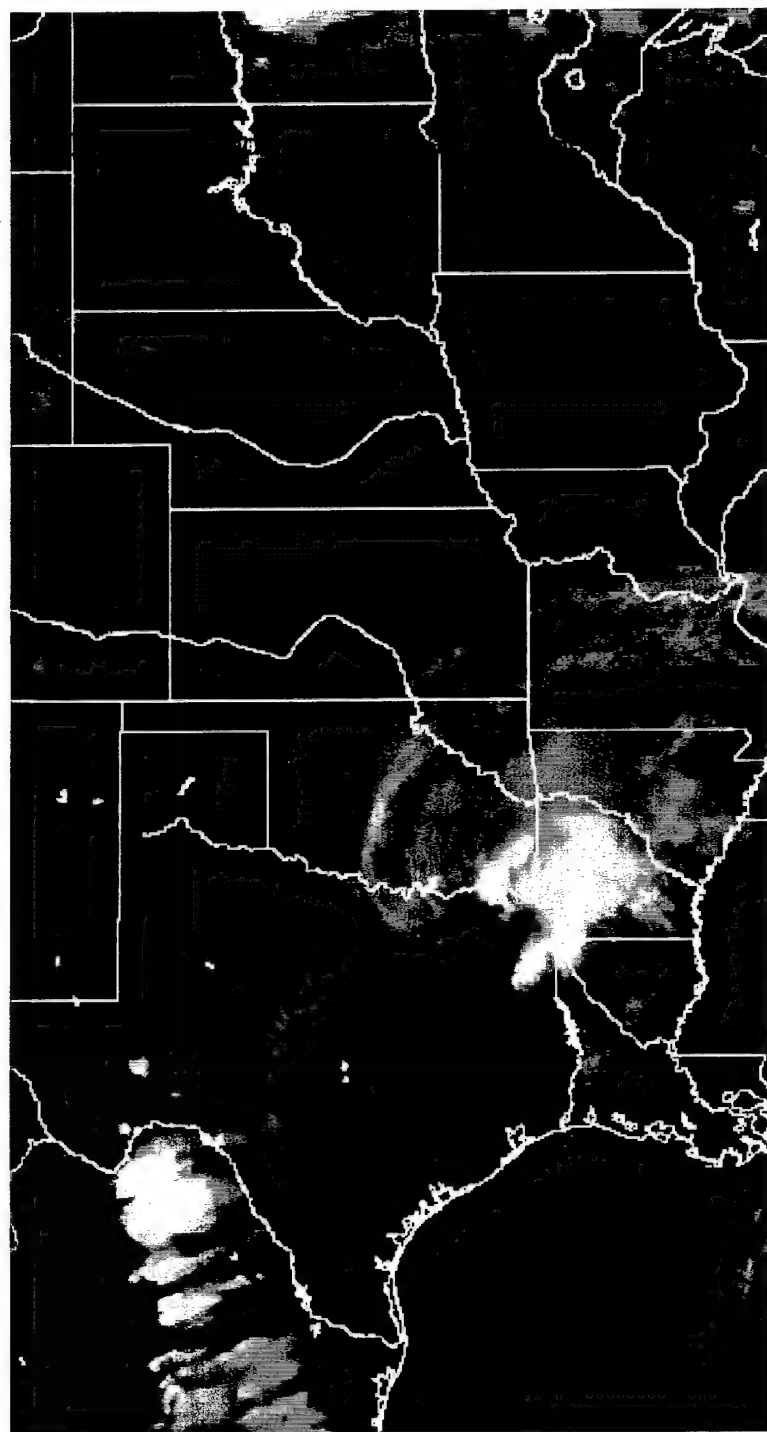
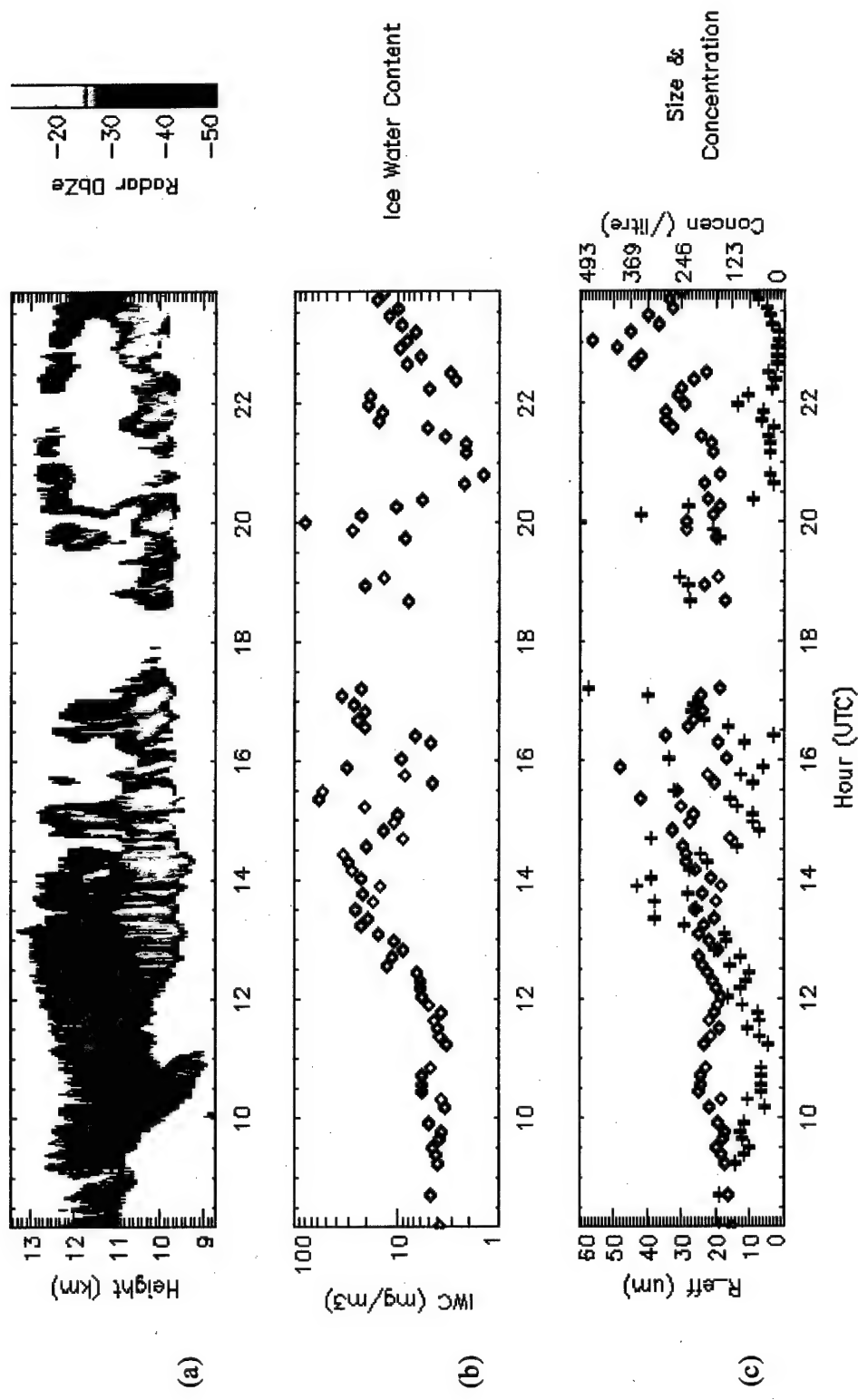


FIG. 21. GOES 8 infrared satellite image for the ARM SGP CART site, 27 May 1998 cirrus case. The time of this image is 2339 Zulu.

FIG. 22. JM98 retrieved, layer-averaged cirrus cloud properties for 27 May 1998 at the ARM SGP CART site for (a) radar reflectivity, (b) ice water content, (c) particle effective radius and concentration, (d) layer emittance and visible optical depth, and (e) solar forcing - fraction of clear-sky flux removed by cloud.

Cirrus Cloud Properties 27 May 1998 SGP CART Site  
 Reflectivity Radiance Algorithm



Cirrus Cloud Properties 27 May 1998 SGP CART Site  
Reflectivity Radiance Algorithm

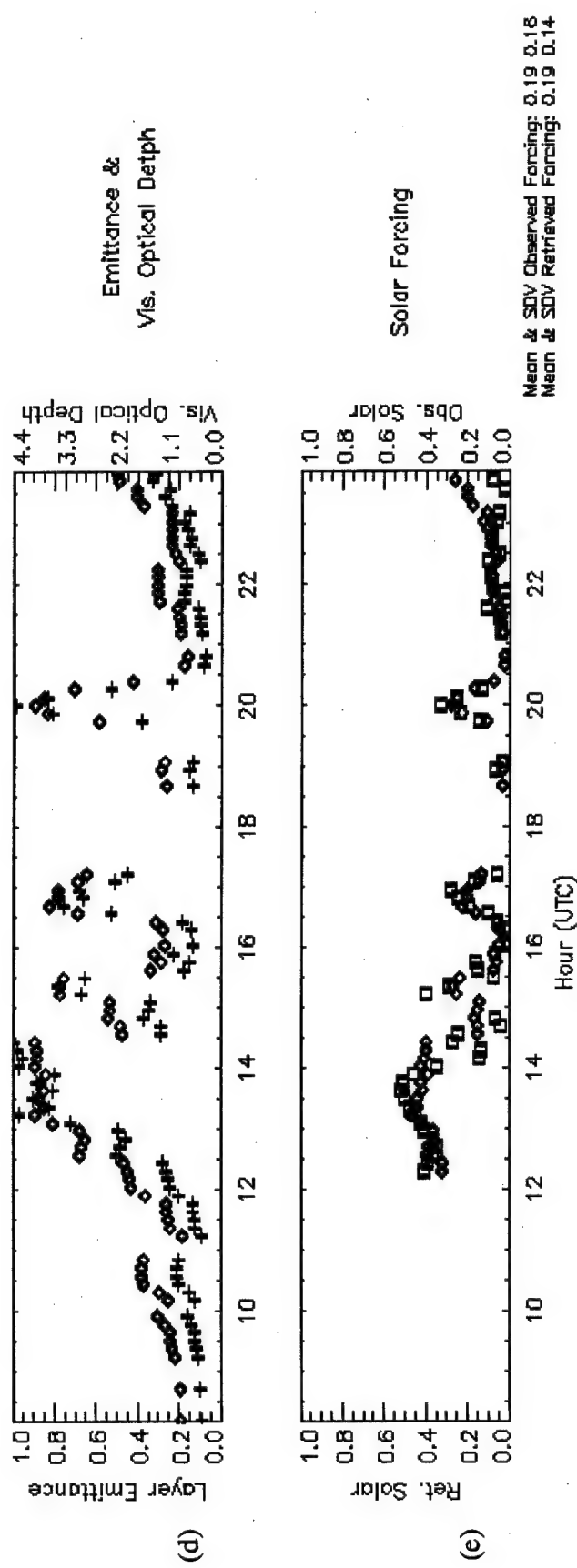


FIG. 22. Continued

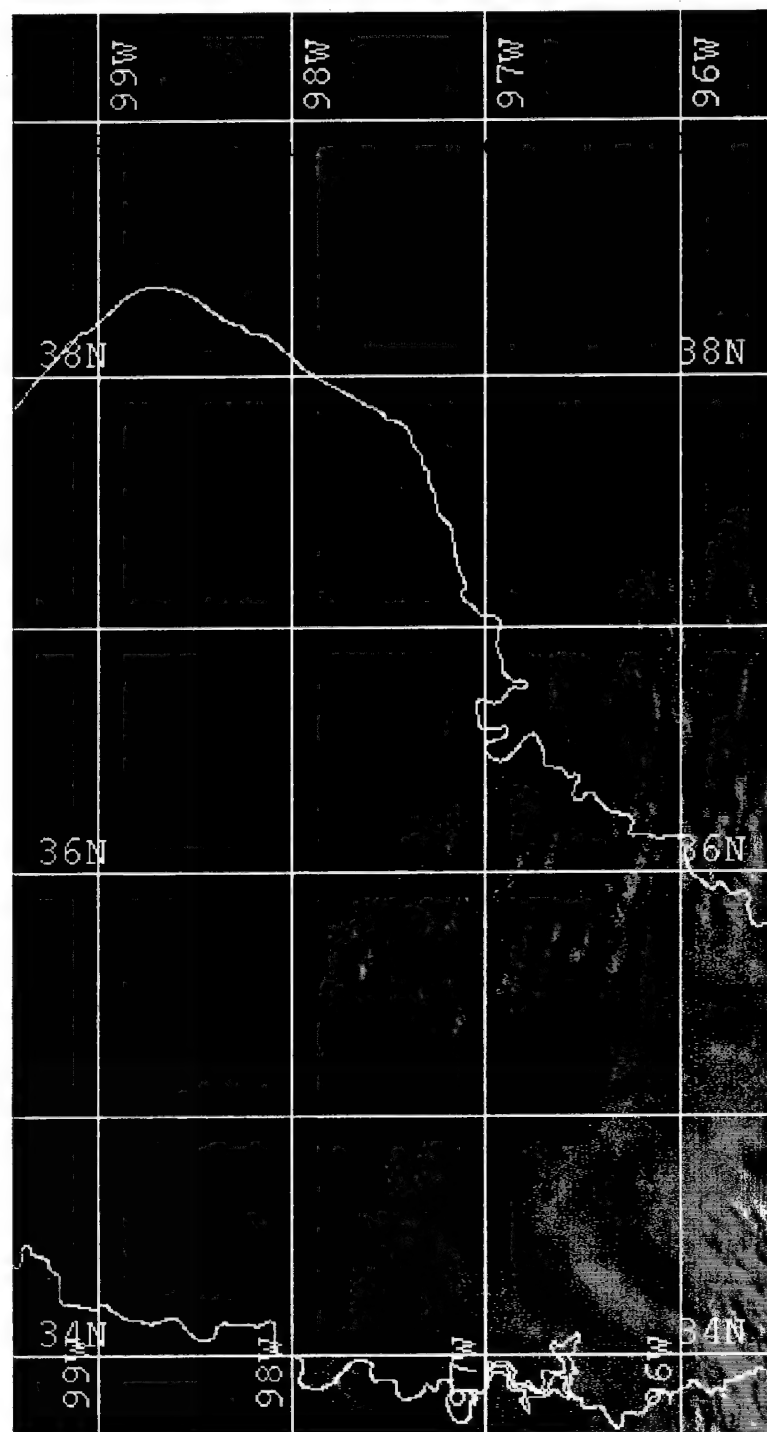


FIG. 23. High resolution GOES 8 visible satellite image for the ARM SGP CART site, 27 May 1998 cirrus case. The time of this image is 1209 Zulu.

The cirrus cloud properties derived from the JM98 algorithm are shown in Figs. 22(b) through 22(d). The IWC for the cirrus was somewhat uniform at the beginning of the time period, as shown in Fig. 22(b), with an average IWC near  $5 \text{ mg/m}^3$ . However, after approximately 13Z, the IWC became quite variable, ranging from a high near  $100 \text{ mg/m}^3$  at 20Z, to a low of  $2\text{-}3 \text{ mg/m}^3$  around 21Z. Overall, for the period from 14Z through the end of the day, the average IWC was approximately  $10\text{-}20 \text{ mg/m}^3$ . The effective radius of the cirrus remained somewhat steady throughout the day, with an average effective radius (from inspection of Fig. 22(c)) of approximately  $20 \mu\text{m}$ . One exception is found near the end of the day, around 23Z, when the particle effective radius rose to an average value near  $40 \mu\text{m}$ ; with a singular maximum of approximately  $60 \mu\text{m}$  near 23Z. The particle concentration for the anvil cirrus was highly variable throughout the entire time period shown in Fig. 22(c). For the beginning, more stratiform period of the day, the average particle concentration is approximately  $120 \text{ liter}^{-1}$ . For the latter period of the day, during the highly variable cirrus conditions, the particle concentration ranged from an average of  $200 \text{ liter}^{-1}$  near 20Z, to a nearly constant value of  $20 \text{ liter}^{-1}$  from 21Z on to the end of the day. The visible optical depths of the cirrus are shown in Fig. 22(d)). The visible optical depths (from inspection of Fig. 22(d)) were also highly variable for the entire time period shown. Between the hours of 14Z to 20Z, the optical depth ranged in magnitude as  $0.5 \leq \tau \leq 4.0$ , with maximums located near 14Z and 20Z. After 21Z, the optical depth was fairly constant --  $\tau \approx 0.8$ .

Comparing these JM98 retrieved microphysical properties to the warm season, layer-mean temperature dependent values (Table 4), a trend similar to the 24 Mar 97 case is found. At the beginning of the time period, the IWP, effective particle radius, and

particle concentration lie very near the average values for the coldest 1/3 of cirrus events observed during the warm season. In contrast to the 24 March 1997 case, the cirrus over the SGP site during this time period was much thicker than the cirrus over the site in that latter period of the day. For this latter portion of the day, the JM98 derived microphysical properties fall closer to the average values for the warmest 1/3 of cirrus events observed during the warm season.

As in the 24 March 1997 case, comparisons for the TOA albedo and the surface solar forcing fraction (Figs. 24(a) and 24(b), respectively) were created. The comparison between the albedos will be analyzed first. Once again, the two albedos compare very well with each other. The average "observed" albedo, derived using PM98, is 26.28%, while the average "calculated" albedo, derived from the JM98 retrievals, is 27.19%. The trends of the two albedos are also in very good agreement. Once again, there are some instances where the magnitude of the two albedos differ. One noticeable difference is found near 20Z in Fig. 24(a). This is also the time when the JM98 algorithm derived a peak in the cloud IWC of approximately  $100 \text{ mg/m}^3$ , a relative maximum in cloud visible optical depth of  $\tau \approx 4.4$ , and corresponding peak in the layer emittance. Additionally, at this time, the MMCR radar reflectivity shows a cloud layer of nearly 1 km in thickness, of relatively high core reflectivity values (near -20 dBZe). However, from inspection of the 27/20Z high resolution visible GOES 8 satellite image (Fig. 25), it is impossible to distinguish this cloud element. As such, one might conclude that the lower albedo derived by PM98 from the satellite radiance may be in error due to the inability of the satellite to resolve such a small individual cloud element. As a result, the effects of this cloud element may have been smoothed by the PM98 spatial averaging over the  $0.9^\circ \times 0.9^\circ$  grid. Additional

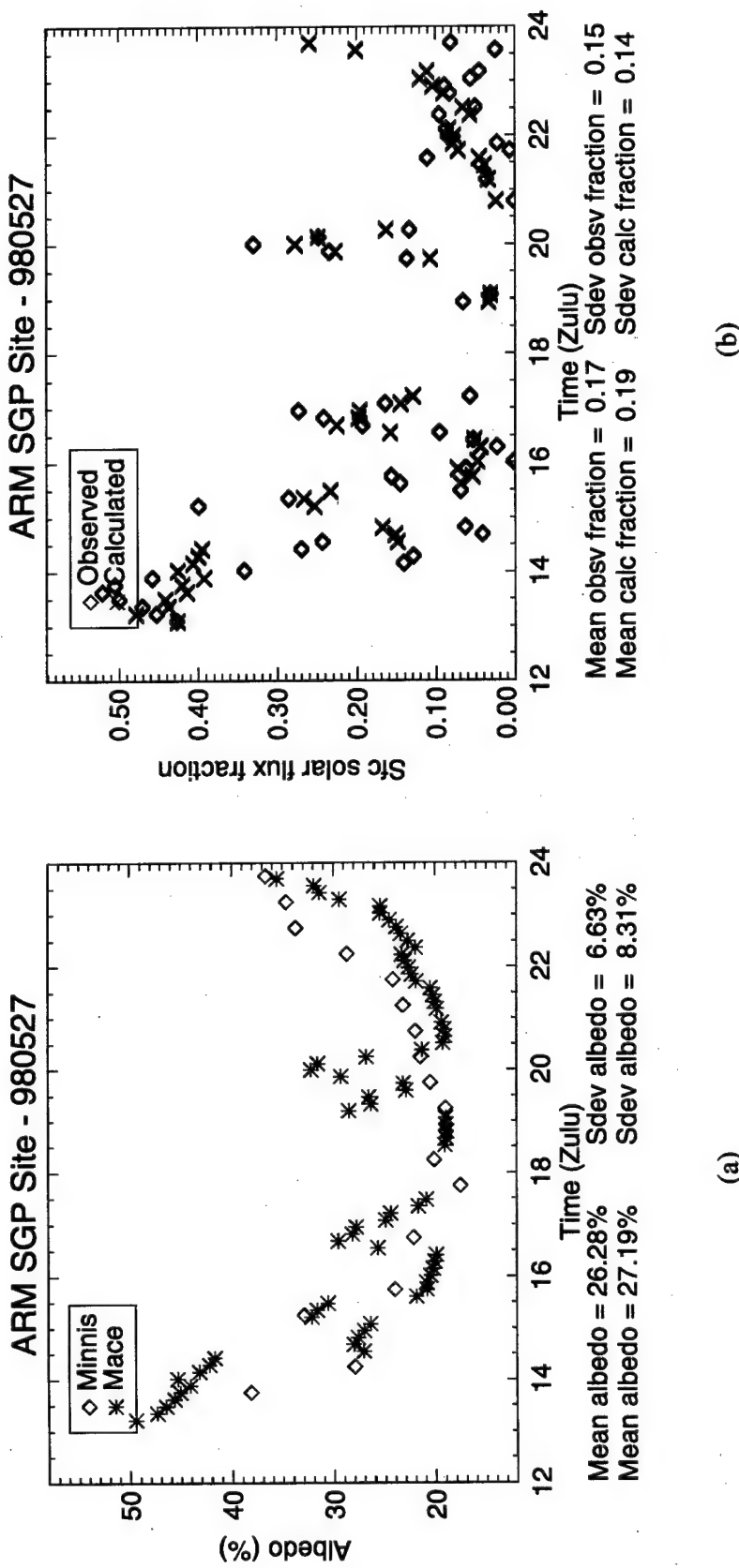


FIG. 24. Comparisons for the 27 May 1998 cirrus case at the ARM SGP CART site for (a) TOA solar albedo(%), and (b) surface solar forcing expressed as the fraction of the clear-sky flux removed by cloud.

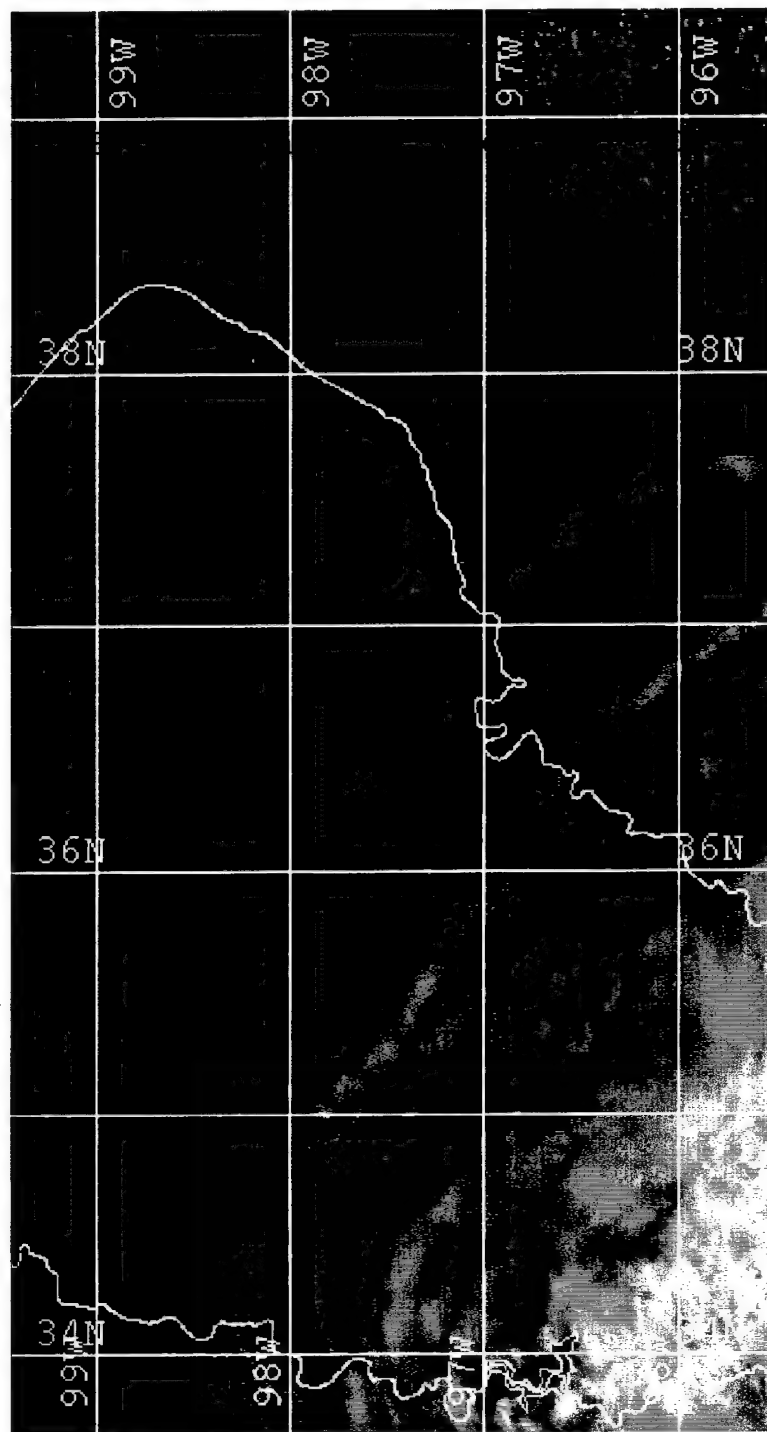


FIG. 25. High resolution GOES 8 visible satellite image for the ARM SGP CART site, 27 May 1998 cirrus case. The time of this image is 2009 Zulu.

support for the error being constrained to the satellite derived albedo is provided in Fig. 24(b). The calculated and observed values near 20Z are in excellent agreement. One exception is found at 20Z. In fact, the actual 20Z calculated fraction (approximately 0.29) is slightly less than the observed solar fraction (approximately 0.33). Since these values represent the fraction of the clear-sky flux removed by the cloud, one can conclude that the higher observed value justifies a locally larger TOA albedo than reported by the area averaged PM98 value.

The observed and calculated solar forcing fractions are in very good agreement. The average magnitude for the calculated values are 0.19, which compares very well to the average magnitude of the observed values of 0.17. The trends found in this comparison are also in very good agreement. Unlike the 24 March case, the surface flux fraction bias in this case is negligible, with very good correlation between individual points on the time series. It is instructive to at least speculate what might have caused this agreement. Using the possible reasons listed for disagreement in the previous case as an outline for this discourse: 1) If the asymmetry parameter in this case is correct ( $\bar{g} = 0.7976 \pm 0.0152$ ), it implies that the microphysical properties of the convectively generated cirrus event were significantly different than the synoptically driven case. This would be a significant finding if it could be confirmed with any certainty; which it cannot. 2) The infrared radiative properties of this case were characterized correctly by the FL93 parameterization. This might suggest that relatively few small particles existed. However, this does not seem appropriate since, given the distance to the convective source region, a significant amount of time would have elapsed allowing the large particles to precipitate from the advecting cirrus. 3) The Long (1995) technique correctly characterized the

downwelling clear-sky surface flux. This statement is certainly true, but we are unable to determine if an incorrect observed clear-sky flux was the source of error in the 24 March 1997 case. While the source of the error in the 24 March case could not be confidently identified, it can be stated with confidence that the 27 May 1998 convective cirrus case is quite well characterized. Thus, this case would make an excellent candidate for a modeling intercomparison case study, or for parameterization development and testing.

#### Calculated and Observed Albedo Correlation

As stated previously, the primary strength of the ARM data streams is their continuity. While several hundred hours of cirrus retrieval data has been processed up to the present time (e.g., <http://www.met.utah.edu/mace/homepages/research/archive/sgp.html>), satellite retrievals have only been performed on a limited subset of these events. A scatter plot of the PM98 derived albedos (observed) compared to the albedos derived from the JM98 retrievals (calculated) is shown in Fig. 26. The comparison is derived from 15 cirrus events ranging in time from 24 March 1997 through 27 May 1998. The individual plots for each cirrus event are included in the appendix. As can be seen in Fig. 26, the correlation between the albedos determined by the two different methods is quite good. The correlation coefficient between the PM98 and JM98 albedos is 0.788, and the slope of the least squares fit line is 1.045. Barnett et al. (1998) performed an analysis to deduce the representativeness of (point) surface solar radiation measurements made at the ARM SGP site to area averages. From the cloudy day nomograms given in Fig. 6 of Barnett et al. (1998), for a time average (given by the AERI observations) on the order of 10 minutes and a spatial averaging radius (given by the PM98  $0.9^\circ \times 0.9^\circ$  grid) on the order of 50 km, the correlation ( $r$ ) between the JM98 and PM98 derived albedos should be

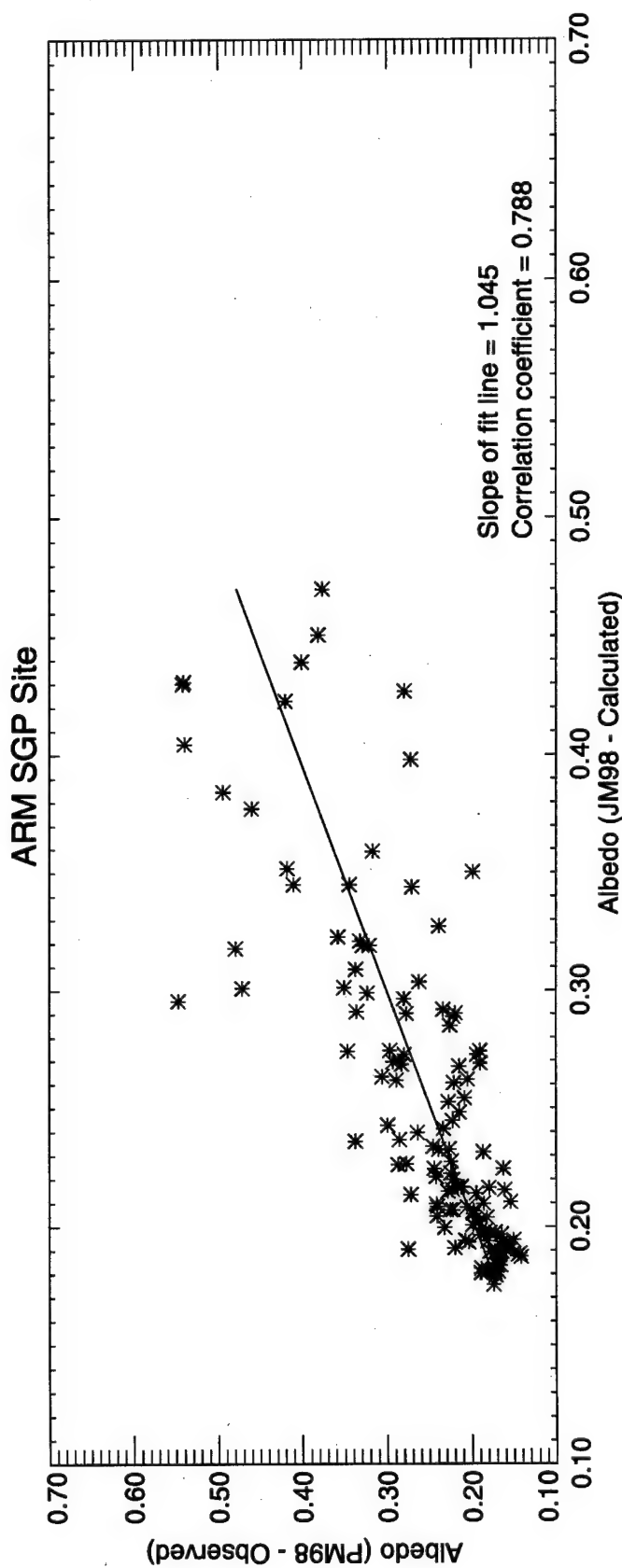


FIG. 26. Comparison of the "observed" (Minnis) albedos versus the "calculated" (Mace) albedos for all 15 ARM SGP CART site cirrus events examined in this research.

on the order of  $r \leq 0.6$ . Thus, for these 15 cirrus events, an albedo correlation of 0.788 is excellent and better than what should be expected.

Aside from the issues previously raised, some of the differences between the albedos derived by the two methods, especially for very thin cirrus, may result from the fixed, lambertian surface albedo used in the RAPRAD radiative transfer simulations. This problem is illustrated in the albedo comparisons for the 28 and 29 April 1997 cirrus events (Figs. 31 and 32, respectively). The parameterization used to derive the satellite "observed" albedos is not constrained in this manner, and the PM98 derived albedos may be more representative in very (optically) thin cirrus cases. However, because these differences are a result of the surface albedo used in the radiative transfer simulation, and not due to a flaw in the radiance-reflectivity (JM98) algorithm, the results derived from JM98 may still be valid. Another cause for the difference in the magnitudes of the two albedos may be due to satellite instrument limitations (resolution). As mentioned in the study of the 27 May 1998 cirrus event, while the MMCR and AERI instruments may be able to distinguish relatively small, individual cloud elements passing over their fields of view, the GOES 8 satellite might not resolve the element as well. However, a similar, but reverse, scenario may apply to the MMCR and AERI. For instance, the narrow fields of view for these instruments may only catch the thin, wispy edge of a larger bright cloud mass, whereas the satellite observation might capture the entire cloud mass. Still, a further reason for the differences might be the spatial averaging used in the PM98 parameterization. This could possibly smooth out very small, bright cloud elements, and thus derive lower albedos. This may be the reason for the scatter in the data plotted to the right and below the least squares fit line in Fig. 26. As for the data where the JM98 albedos

are less than the PM98 albedos, the scatter in this data may be a result of the JM98 algorithm's underprediction of the total ice mass in the column; as in the 24 March 1997 case. However, further research into this matter is necessary.

#### Anomalous Absorption

A fairly recent study by Cess et al. (1995) claims that our current understanding of the interaction between clouds and solar radiation is incomplete. In this study, the authors use a combination of satellite and ground-based radiometer data, at several locations worldwide, to conclude that clouds absorb more solar radiation than can be accounted for by current theory. In fact, their research finds that cloudy atmospheres result in approximately  $25 \text{ W/m}^2$  more global-mean absorption than what is predicted by theoretical models. Their findings are said to be invariant with respect to location and season.

To support their hypothesis, Cess et al. (1995) employ an approach patterned after a study of Antarctic clouds (Nemesure et al. 1994), which used scatter plots of the TOA albedo against the atmospheric transmission (e.g., Fig. 2 of Cess et al. 1995). The atmospheric transmission is defined as the ratio of the solar insolation at the earth's surface to that at the TOA. Using the slope ( $\beta$ ) of a linear root mean square fit of the scatter plot data, given as

$$\beta = \frac{d(\text{TOA Albedo})}{d[(\text{Surface Insolation})/(\text{TOA Insolation})]} \quad (15)$$

Cess et al. (1995) infer to what degree the cloudy column absorbs solar radiation. This inference is gleaned from comparisons with values of  $\beta$  derived from scatter plots of data

produced by two general circulation models (GCM): the European Centre for Medium-Range Weather Forecasts (ECMWF) model (ECMWF GCM cycle 36), and the National Center for Atmospheric Research Community Climate Model version 2 (NCAR CCM2). The slopes for the two GCMs were nearly identical -- for the ECMWF CGM,  $\beta = -0.79$ , while  $\beta = -0.81$  for the NCAR CCM2. The slope of the data gathered by Cess et al. (1995), derived from the visible channel brightness counts of the GOES image centered over Boulder Colorado and near-surface pyranometer data mounted on the National Oceanic and Atmospheric Administration's Boulder atmospheric observatory tower, was found to be  $\beta = -0.59$ . The authors claim that the *only* way the value of the GCMs'  $\beta$  can be modified to agree with their observed value is through an increase in cloud shortwave absorption. An increase in the cloud shortwave absorption would result in less surface insolation (lower transmission values), with a simultaneous decrease in TOA albedo (darker, more absorbing clouds). The end result is a more shallow slope for the scatter plot.

Taking their hypothesis one step further, Cess et al. (1995) state that  $\beta$  is a direct determinate of cloud absorption. Integrating equation (15), they arrive at a relation between  $\beta$  and the shortwave cloud forcing ( $C_s$ );  $C_s$  is the difference between cloudy-sky and clear-sky net downward (downwelling minus upwelling) radiation. The relation between  $\beta$  and the cloud forcing ratio ( $C_s(S)/C_s(TOA)$ ) is shown to be

$$\frac{C_s(S)}{C_s(TOA)} = \frac{(1 - \alpha_s)}{\beta} \quad (16)$$

where  $\alpha_s$  is the surface albedo. According to Cess et al. (1995), equation (16) applies in the absence of broken-cloud enhancements of surface insolation. Theoretical cloud models typically produce cloud forcing ratios near unity; the ratio for the two GCMs is 1.07 (Cess et al. 1995). For the observed data, with a surface albedo of 0.17 derived from the upward and downward facing pyranometers on the Boulder tower, the cloud forcing ratio is found to be 1.41. With an observed cloud forcing ratio of 1.41 and model calculated cloud forcing ratios of 1.07, the authors conclude that the GCMs underestimate cloud absorption, and that their results point to a shortcoming in the current knowledge of cloud radiative transfer processes. Additionally, from further analysis of their data (not discussed here), Cess et al. (1995) argue that the shortwave cloud forcing enhancement is not due to factors such as interstitial water vapor content within the atmospheric column, aerosol influence on cloud albedo, or cloud geometry. However, they do not provide a physical explanation for the anomalous absorption of shortwave radiation by cloudy atmospheres.

Since this research involved similar data streams, it seemed readily applicable for use in the approach employed by Cess et al. (1995). However, we did not have an observed value for the downwelling TOA solar flux; for use in the observed atmospheric transmission ratio. Therefore, in both the observed and calculated cases, the adjusted RAPRAD-calculated 16 km downwelling solar flux was used as the TOA solar flux. The observed surface solar insolation was given by the downwelling hemispheric solar flux measured by the baseline surface radiation network (BSRN) at the SGP site. The PM98-derived shortwave broadband albedos were used as the observed TOA albedos. The two cases previously discussed in this chapter were chosen as candidates for the approach used

in Cess et al. (1995). The scatter plots for 24 March 1997 and 27 May 1998 are shown in Figs. 27 and 28, respectively.

In the 24 March 1997 scatter diagram (Fig. 27), the observed data produced  $\beta = -0.82$ , while the calculated data resulted in  $\beta = -0.62$ . Although the difference between the two slopes is relatively large, the paucity of observed data points, and the differences between the end of day albedos (see Fig. 17) and the low bias of the calculated surface solar flux fractions could be the primary causes behind the different  $\beta$  values. Also, it is interesting to note that the results from this case are exactly opposite from those derived by Cess et al. (1995). For our 24 March 1997 data, the slope of the calculated (model) data would suggest that some anomalous absorption in the cloudy atmosphere is occurring, while slope of the observed data suggests the opposite.

Applying this same data analysis technique to the 27 May 1998 data (Fig. 28), we found an observed  $\beta = -0.41$ , while the calculated data produced  $\beta = -0.72$ . In this case, the calculated (model) data suggests anomalous absorption is not occurring, while the observed data suggests larger than expected amounts of solar radiation are being absorbed in the cloudy column; in direct contrast to the results from 24 March. Further inspection of the original albedo plot (Fig. 24) might explain this discrepancy. Near 20Z on this day (see Fig. 24(a)), the calculated albedos were approximately 10% greater in magnitude than the observed albedos; a possible result of the spatial averaging used in PM98. Around this same time, Fig. 24(b) shows good agreement between the observed and calculated surface solar forcing fractions ( $\sim 0.30$ ). Remembering that these fractions represent the amount of clear-sky flux removed by the cloud, the combination of a low observed albedo and a relatively high observed surface solar flux fraction would produce data points near the

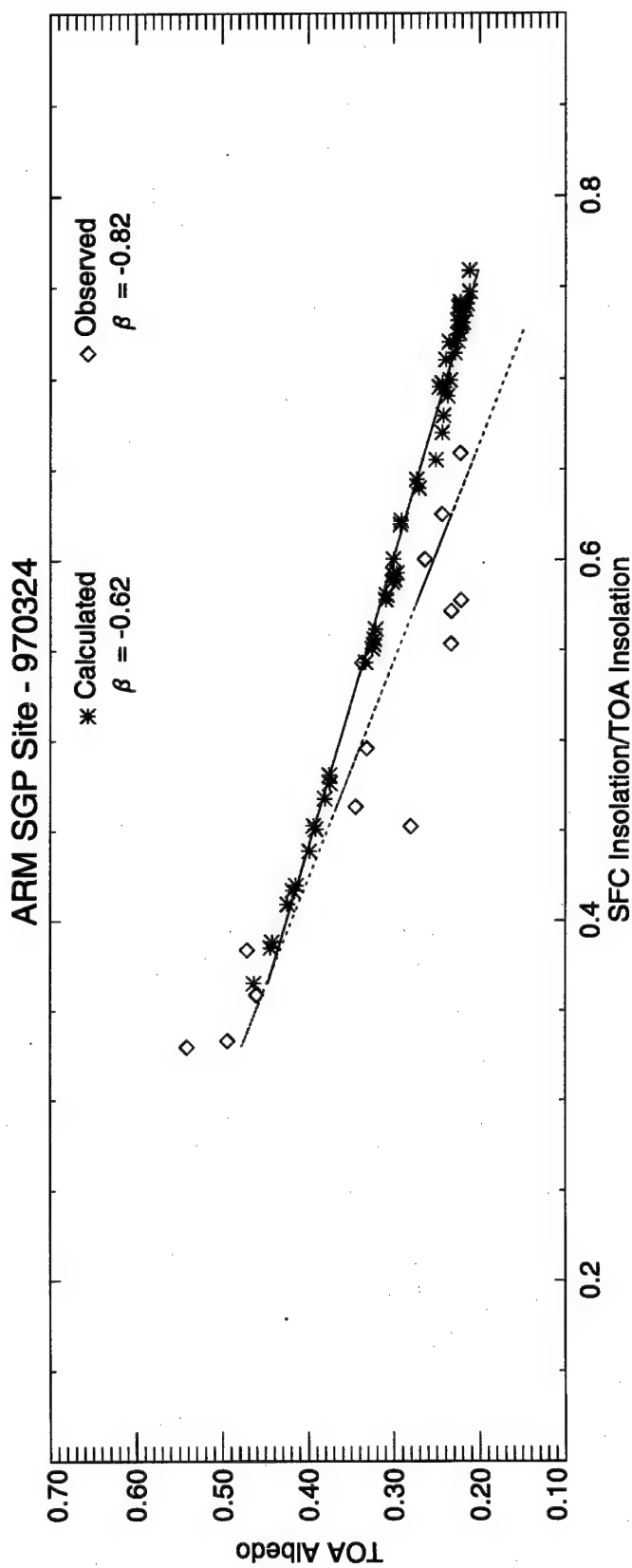


FIG. 27. Scatter plot of TOA albedo versus atmospheric solar transmission. The atmospheric transmission is expressed as the ratio of surface solar insolation to that at the TOA. The calculated data (blue asterisks) are derived from the JM98 algorithm. The observed data (red diamonds) are derived from the PM98 parameterization. The TOA solar insolation is given by the adjusted downwelling 16 km solar flux calculated from the RAPRAD radiative transfer code, for both data sets.

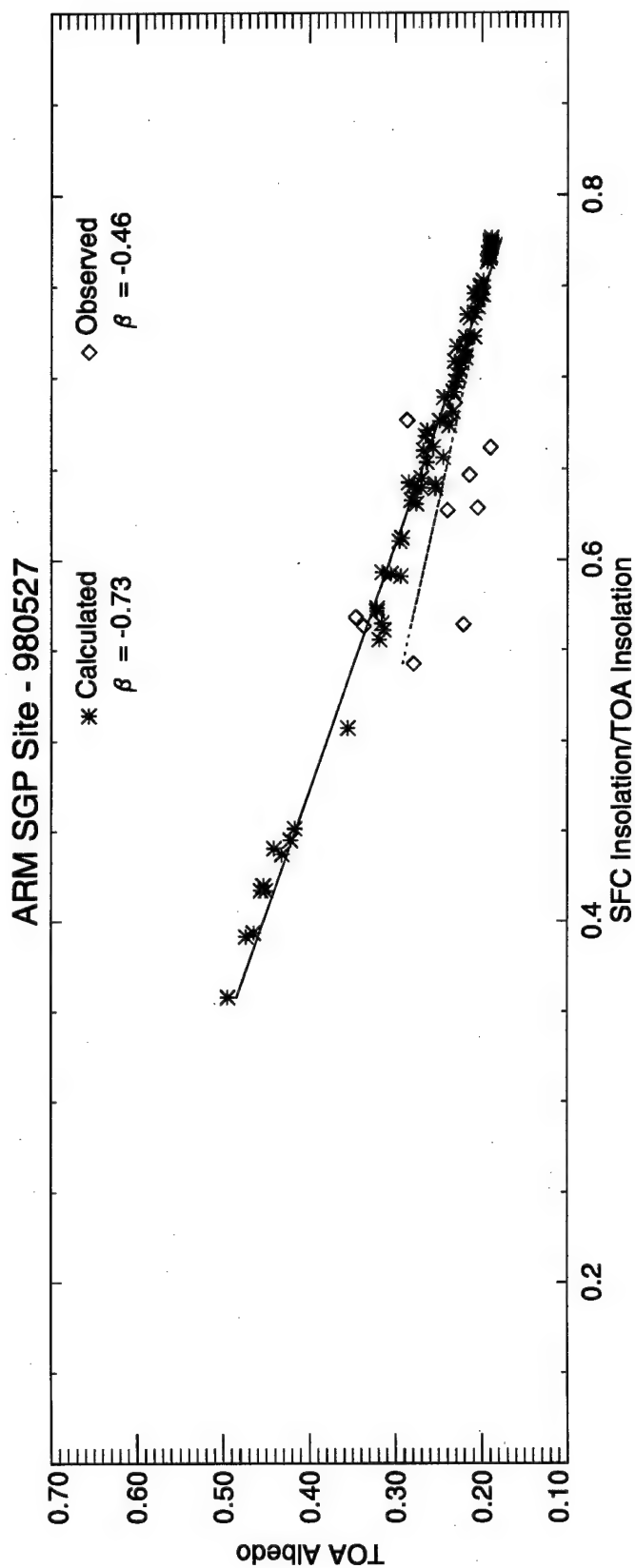


FIG. 28. Scatter plot of TOA albedo versus atmospheric solar transmission. The atmospheric transmission is expressed as the ratio of surface solar insolation to that at the TOA. The calculated data (blue asterisks) are derived from the JM98 algorithm. The observed data (red diamonds) are derived from the PM98 parameterization. The TOA solar insolation is given by the adjusted downwelling 16 km solar flux calculated from the RAPRAD radiative transfer code, for both data sets.

bottom and toward the left of the scatter diagram of albedo versus atmospheric transmission. The 14Z data in Fig. 24 would produce a similar result. Thus, due to the combination of the relatively few observed data points and the problems described for the 14Z and 20Z data, the interpretation of the observed  $\beta$ , for this case, may be flawed.

While our results are contradictory and it is certainly impossible to make any definitive conclusions regarding anomalous absorption given just two case studies, these comparisons do show the potential pitfalls of using satellite-derived albedos in conjunction with fluxes measured by surface pyranometers; as Cess et al. (1995) did in their original paper. Even though sampling problems were identified in these cirrus cases, upper troposphere clouds would tend to minimize the spatial mismatch inherent in this technique, given their distance from the radiometer. On the other hand, using this technique to study the effects of lower troposphere clouds could lead to larger errors. If an attempt were to be made to draw *any* conclusion from either of the observed data sets, the wider range in the data for the 24 March 1997 case would make the slope of its least squares fit line more believable. The fact that the observed slope, for this case, is greater than the model predicted slope, and thus would imply less absorption than predicted by the model data, is somewhat significant.

## CHAPTER 5

### SUMMARY AND CONCLUSIONS

Cirrus clouds are an integral element of the global climate system. However, because of their location in the cold upper troposphere and due to their complex interactions with incoming solar and outgoing infrared radiation, they remain one of the least understood components of the climate system. In order to develop a continuous record of the characteristics of optically thin cirrus, the ARM program is currently using the JM98 algorithm to retrieve the layer-averaged microphysical properties of cirrus. Using the MMCR reflectivity and the downwelling radiance observed by the AERI, the algorithm derives these properties in terms of a low-order, modified gamma distribution of particle size. To ensure confidence in the algorithm's capabilities, comparisons against observations are necessary. Given that the ultimate goal of the ARM program is to evaluate how clouds affect the radiation field, comparisons against observed atmospheric radiative quantities is preferred.

In an effort to validate the JM98 cirrus retrievals, we attempted to compare the MODTRAN forward-calculated visible radiance, computed using the cirrus radiative properties derived from the JM98 retrievals, to GOES 8 observed visible radiances. Since radiance calculations involve very specific solid angles, it was necessary to use the "exact" phase function for cirrus clouds (e.g., Takano and Liou, 1989), in addition to the JM98-derived cirrus radiative properties. Although MODTRAN allows users to input spectrally dependent, cloud microphysical properties (asymmetry parameter, absorption and

extinction coefficients) via the user-defined cloud option (ICLD or ICLD1 =11), there is no input conduit available for a user-defined *cloud* phase function. The only user-defined phase function option available with MODTRAN is for use with *aerosols*. The phase function used by MODTRAN for user-defined clouds is determined from the user-supplied, spectrally dependent asymmetry parameter (e.g., HG phase function). As demonstrated in Fu and Takano (1994), the phase function for ice crystals, which contains a strong forward scattering peak and specific halos and backscattering features, can not be adequately represented by a single parameterization in terms of the asymmetry parameter. Thus, MODTRAN (and its user-defined cloud option) could not be used to accurately compute the TOA visible radiance from our JM98 derived radiative properties. Additionally, attempts to use the MODTRAN standard cirrus model (ICLD =18) for the radiance comparisons were stymied by the 26 *incorrect or old subroutines* provided with MODTRAN 4, Version 1.1 (Beta), via the AFRL/VSBM file transfer protocol site. As such, this avenue of approach was abandoned and an alternate method was adopted.

The alternate research approach used the JM98-derived cirrus radiative properties as input to the RAPRAD radiative transfer code (Toon et al. 1989). From these radiative transfer simulations, upwelling and downwelling solar fluxes were computed at a vertical resolution of 0.25 km, up to a proxy TOA of 16 km. Through comparisons of the calculated TOA solar albedo, derived from the ratio of the (adjusted) calculated TOA fluxes, with shortwave broadband albedos, derived from satellite observations and the PM98 parameterization, we show that the JM98 retrieved properties result in reasonably good estimates of TOA solar albedo. For the 15 cirrus cases given in Appendix A, the correlation factor between the two albedos is 0.788, which is much better than would be

expected from the analysis of Barnett et al. (1998). Further, as presented in the two cirrus case studies, it was shown that the JM98 retrievals resulted in reasonable estimates of the surface flux. The discrepancies found in the comparisons of the radiative quantities derived from the JM98 retrievals and the "observed" quantities may be due to many factors: the fixed, isotropic surface albedo used in the RAPRAD calculations, the insensitivity of the MMCR and the JM98 algorithm to small cirrus particles, problems with the FL93 parameterization (e.g., resulting in asymmetry parameters that may be too large), errors introduced by using 16 km fluxes for the TOA values, errors introduced by using the technique of Long (1995) to determine the clear sky flux, instrument limitations, or because of the spatial averaging inherent to the satellite observations. However, pinpointing these shortfalls and identifying areas of improvement within the JM98 algorithm require further investigation, and are recommended for future research. Additionally, since this research involved only 15 cirrus events and two case studies, it is recommended that further research of a similar nature include additional cirrus events. This may require the identification of an alternate comparison method, since the PM98 parameterization is not being implemented on an operational basis. More comparisons (for both surface and TOA radiative quantities) may also provide better insight into the topic of anomalous absorption in cloudy atmospheres. However, a different approach than that employed by Cess et al. (1995) is recommended.

Given the overall agreement between the TOA albedo comparisons and, as shown in the two cases examined in this study, the ability of the JM98 retrieved cloud properties to reasonably model the effects of cirrus on the solar flux at the surface, we feel confident that the JM98 algorithm has attained a reasonable level of accuracy. However, as with any

scientific endeavor, refinements and improvements are necessary and should be actively sought out. Future improvements might incorporate and exploit additional remote-sensing capabilities. They might also incorporate more recent improvements in the parameterization of the broadband solar and infrared properties of cirrus (e.g., Fu et al. 1998). Regardless, the accomplishments of the JM98 algorithm to effectively derive the layer-averaged cirrus microphysical properties should be seen as a good first step and not an end state.

## **APPENDIX**

### **ALBEDO COMPARISONS**

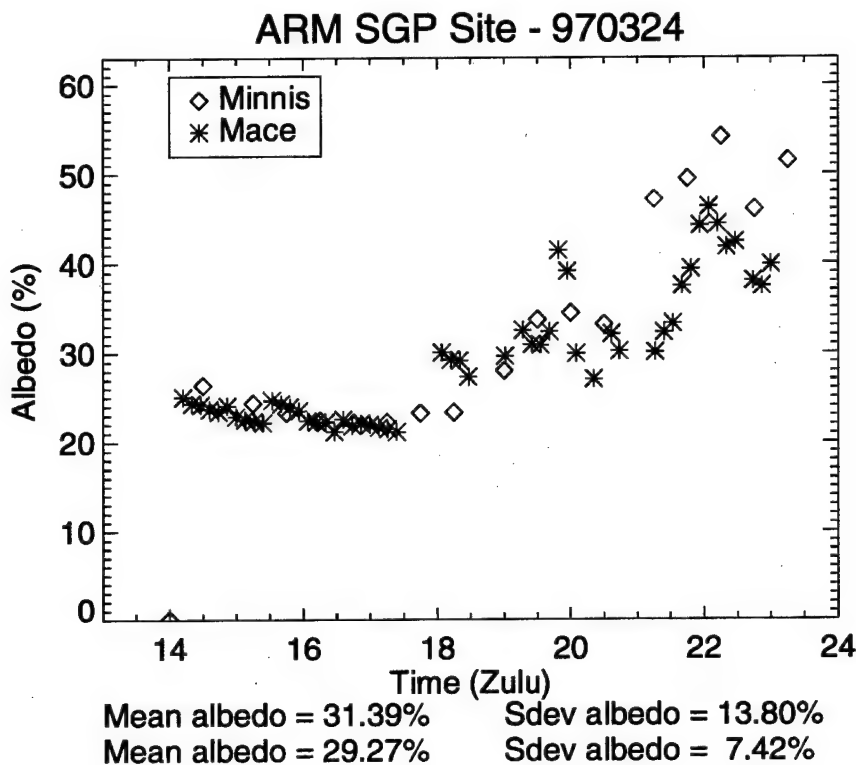


FIG. 29. Comparison of TOA solar albedo for the 24 March 1997 cirrus case at the ARM SGP CART site.

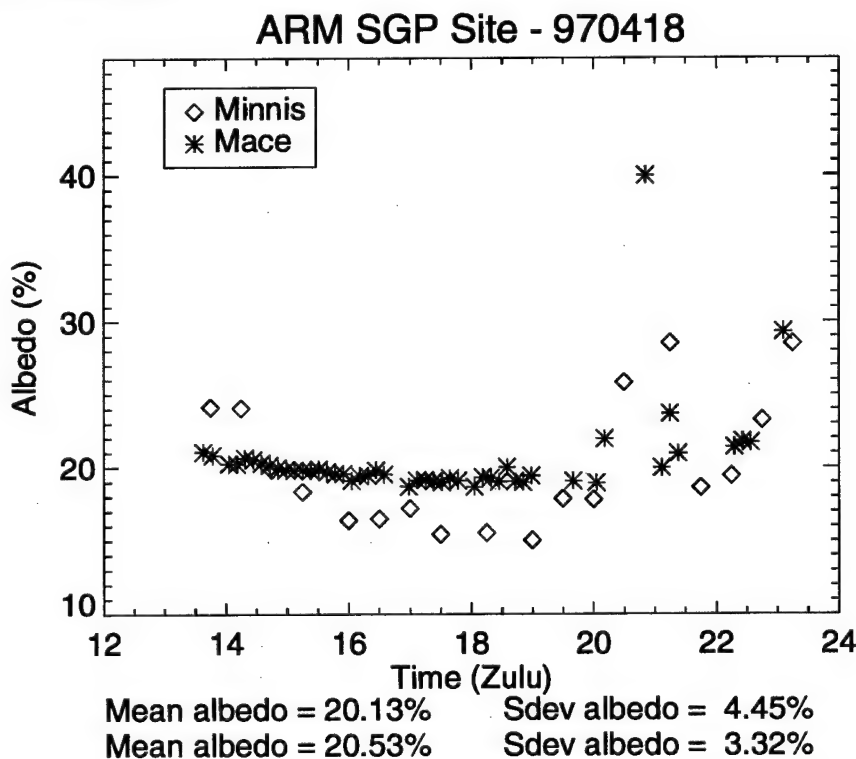


FIG. 30. Comparison of TOA solar albedo for the 18 April 1997 cirrus case at the ARM SGP CART site.

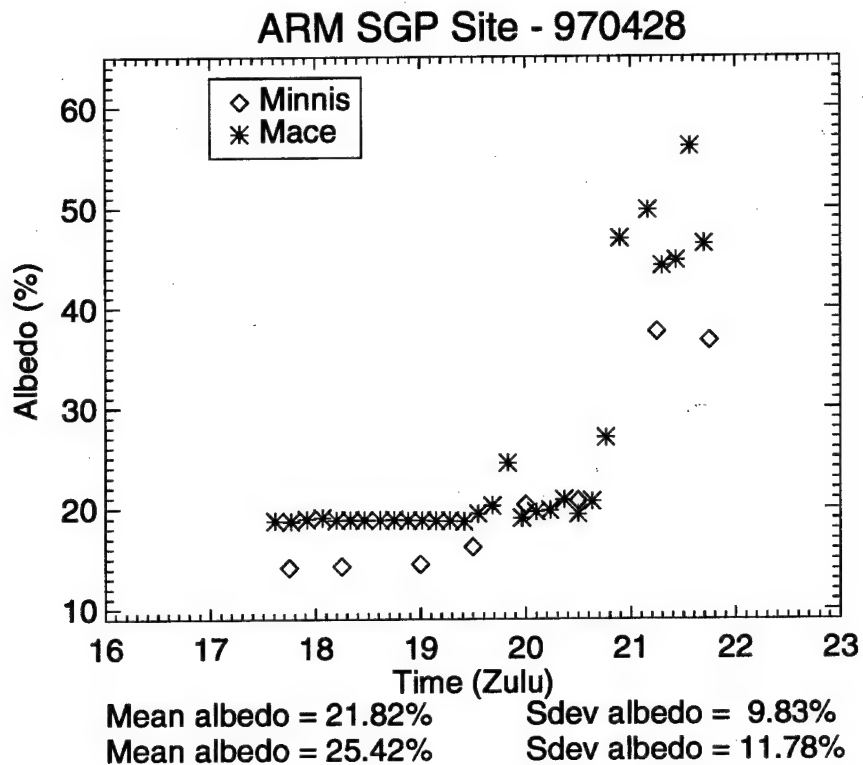


FIG. 31. Comparison of TOA solar albedo for the 28 April 1997 cirrus case at the ARM SGP CART site.

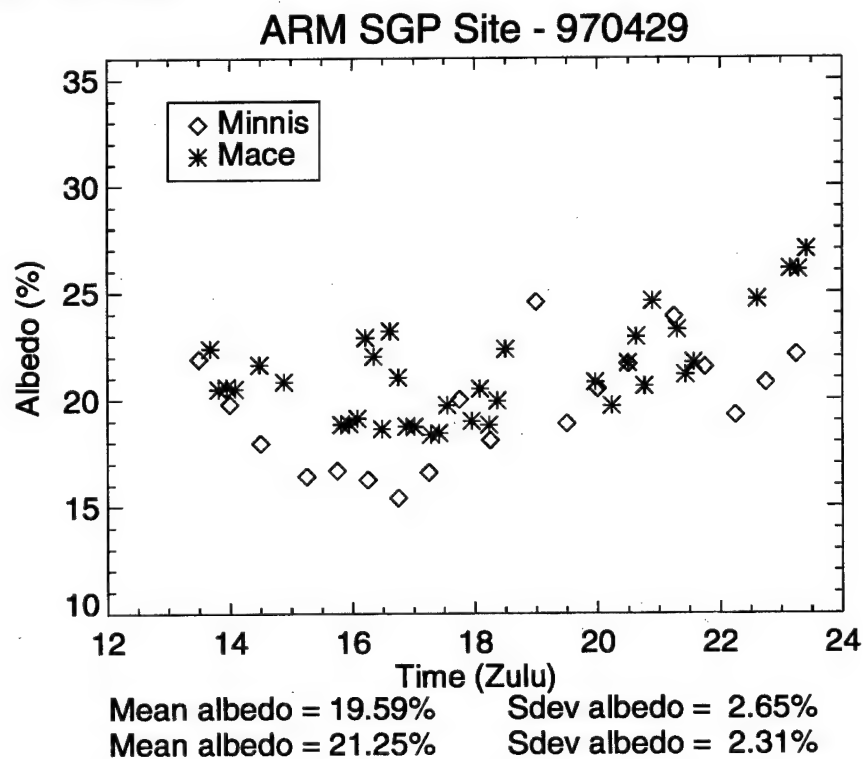


FIG. 32. Comparison of TOA solar albedo for the 29 April 1997 cirrus case at the ARM SGP CART site.

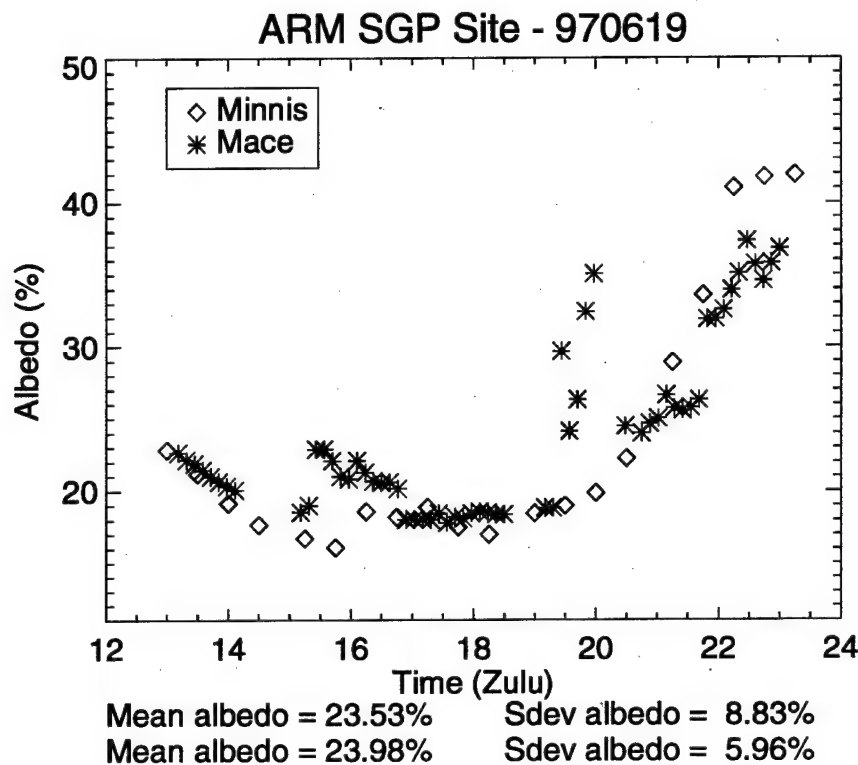


FIG. 33. Comparison of TOA solar albedo for the 19 June 1997 cirrus case at the ARM SGP CART site.

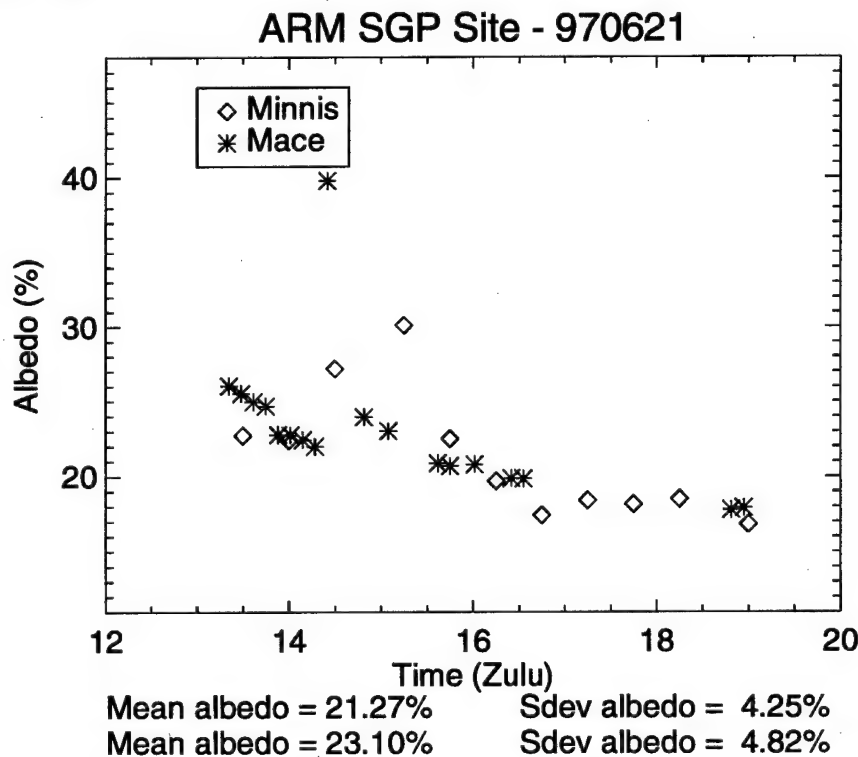


FIG. 34. Comparison of TOA solar albedo for the 21 June 1997 cirrus case at the ARM SGP CART site.

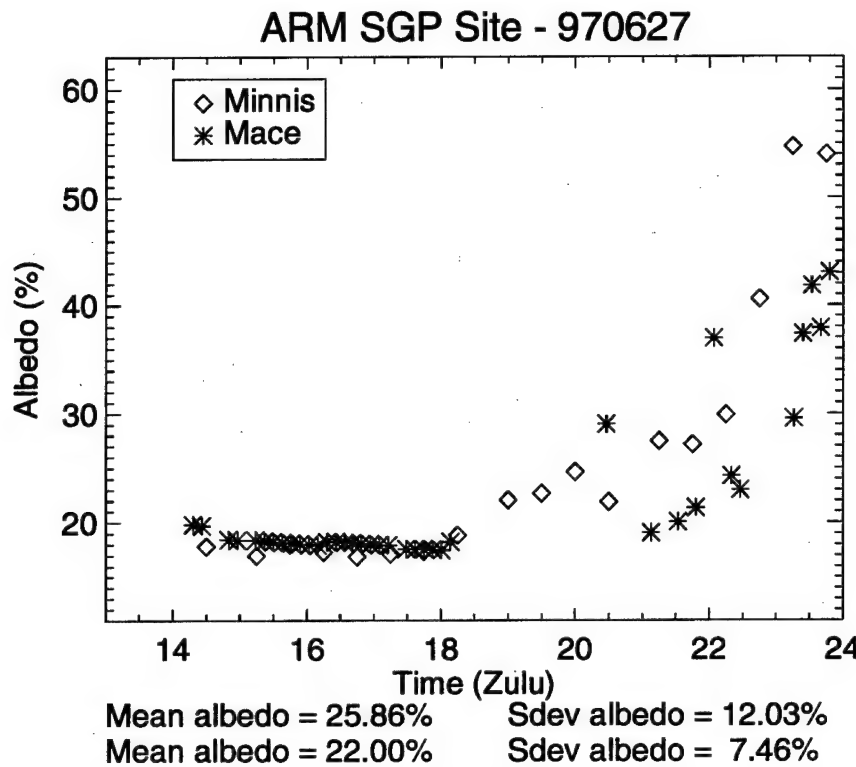


FIG. 35. Comparison of TOA solar albedo for the 27 June 1997 cirrus case at the ARM SGP CART site.

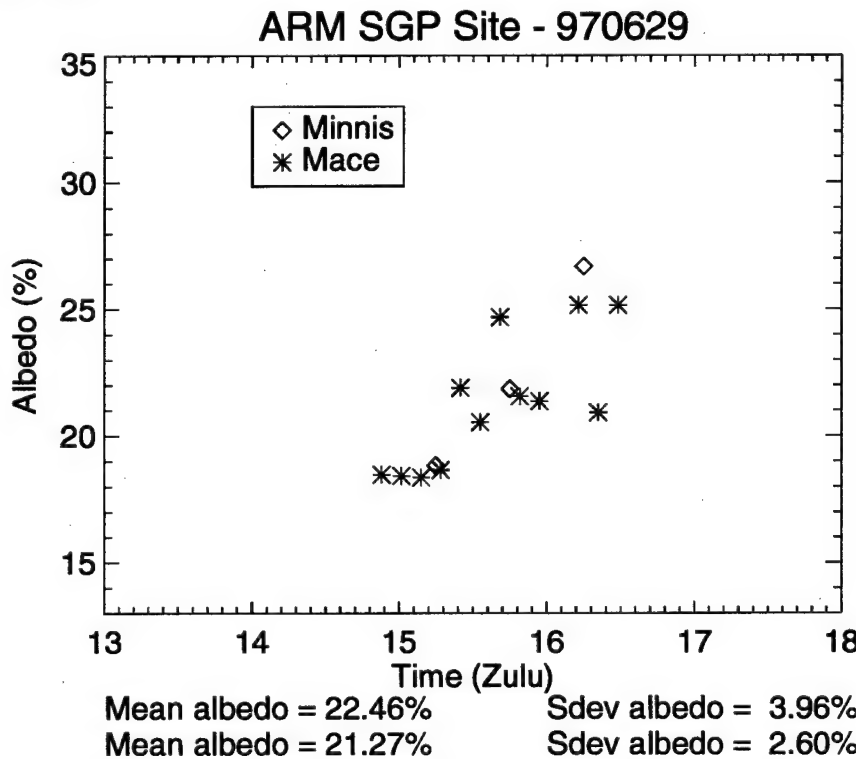


FIG. 36. Comparison of TOA solar albedo for the 29 June 1997 cirrus case at the ARM SGP CART site.

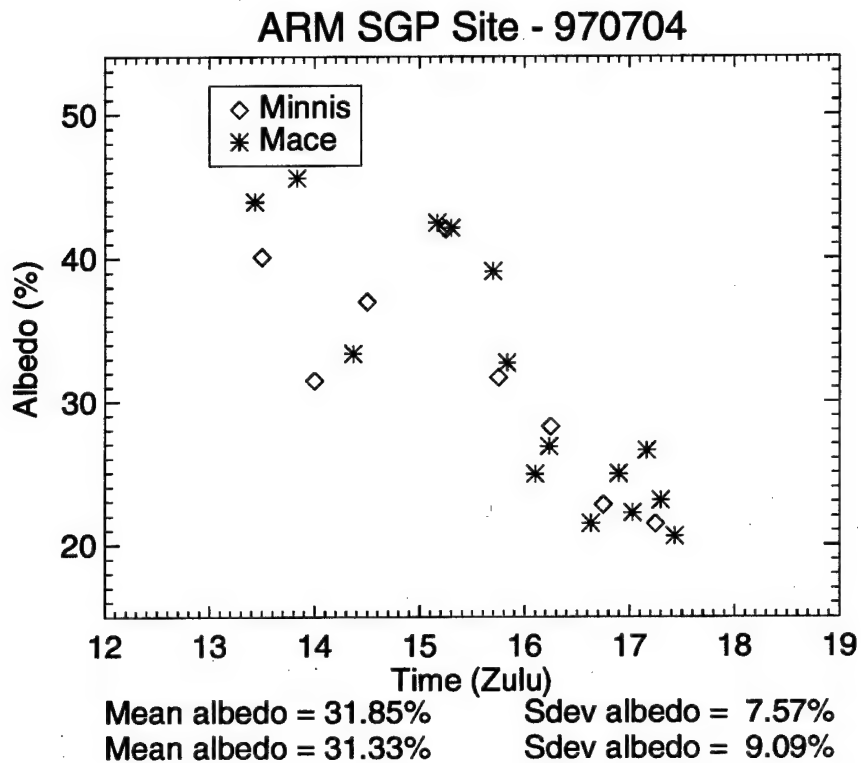


FIG. 37. Comparison of TOA solar albedo for the 4 July 1997 cirrus case at the ARM SGP CART site.

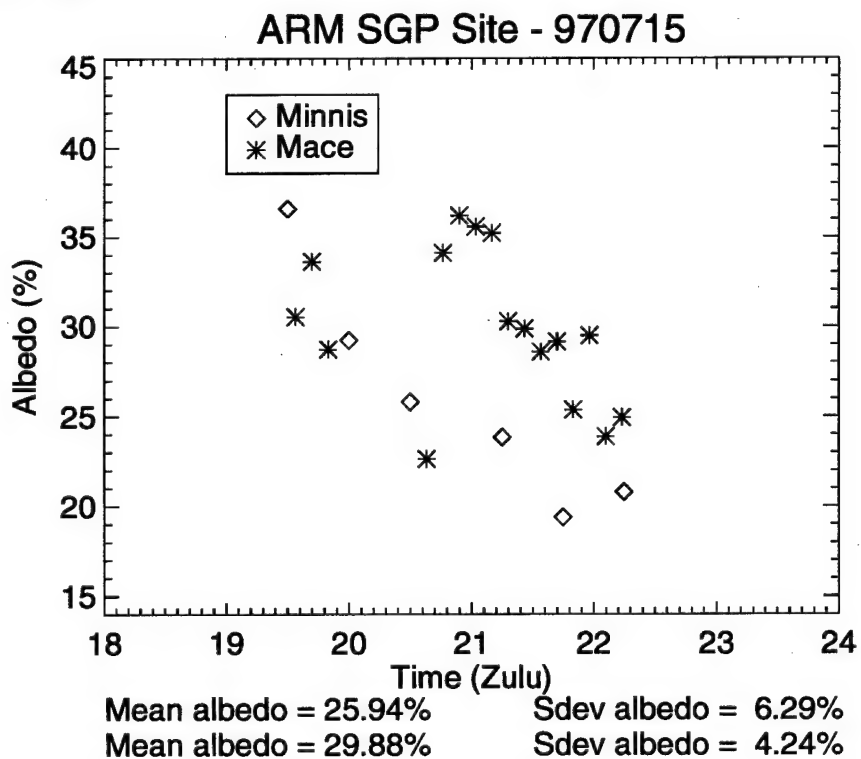


FIG. 38. Comparison of TOA solar albedo for the 15 July 1997 cirrus case at the ARM SGP CART site.

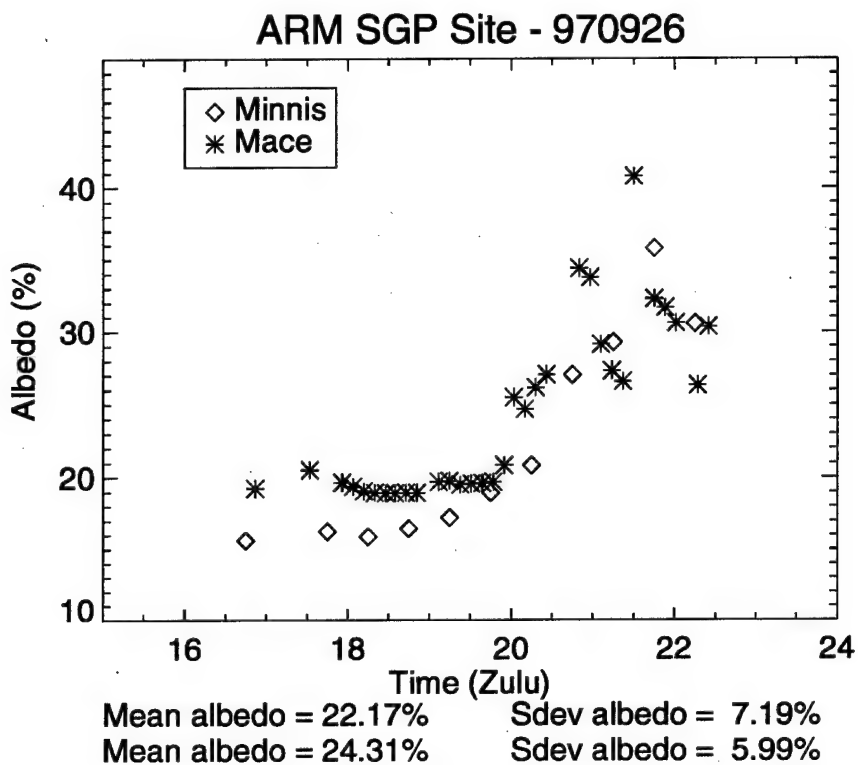


FIG. 39. Comparison of TOA solar albedo for the 26 September 1997 cirrus case at the ARM SGP CART site.

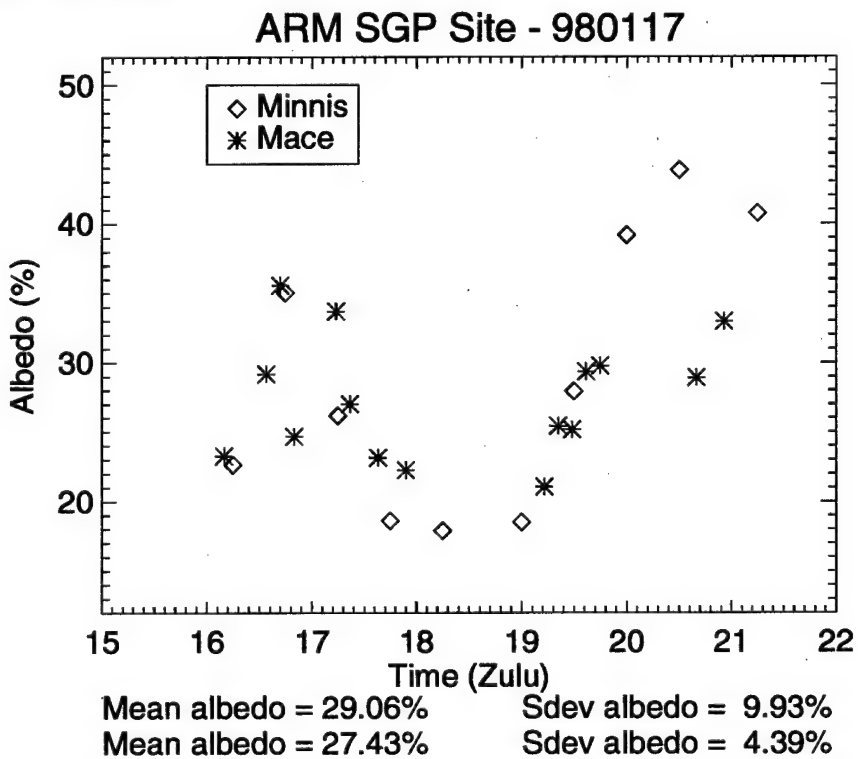


FIG. 40. Comparison of TOA solar albedo for the 17 January 1998 cirrus case at the ARM SGP CART site.

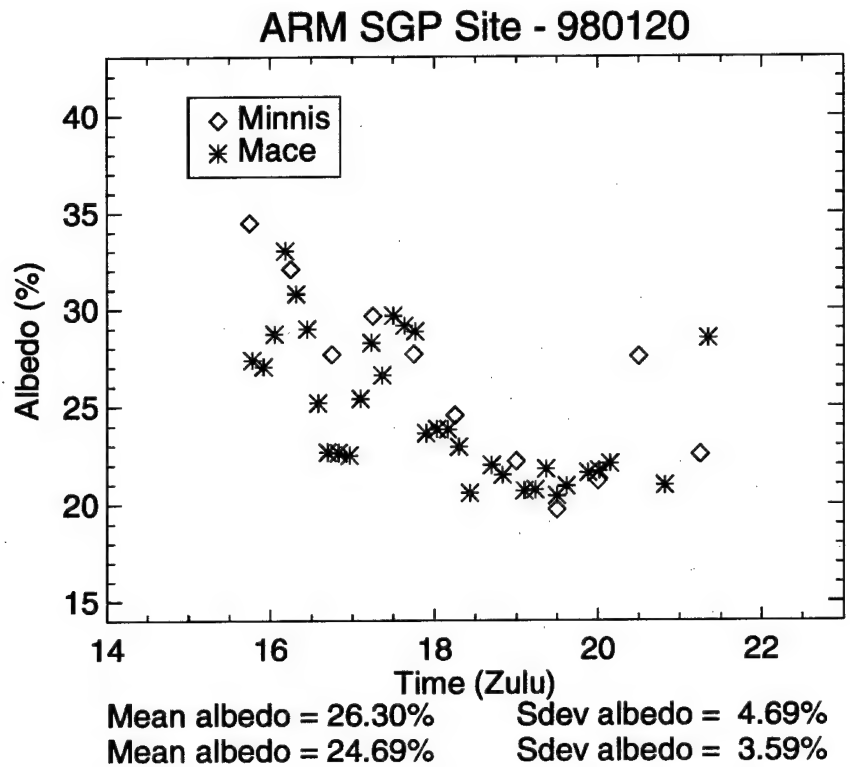


FIG. 41. Comparison of TOA solar albedo for the 20 January 1998 cirrus case at the ARM SGP CART site.

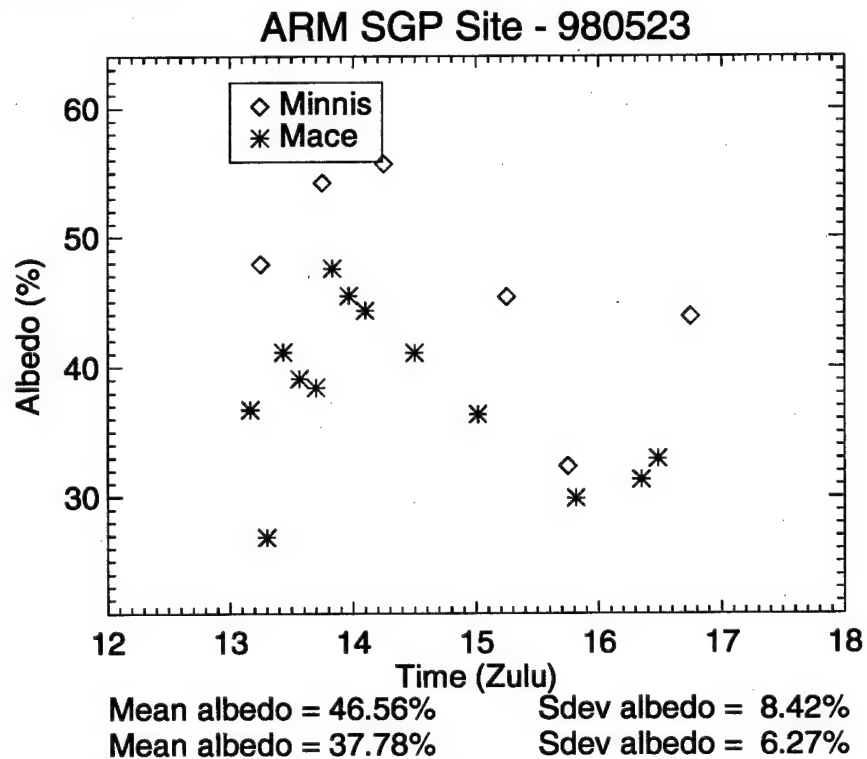


FIG. 42. Comparison of TOA solar albedo for the 23 May 1998 cirrus case at the ARM SGP CART site.

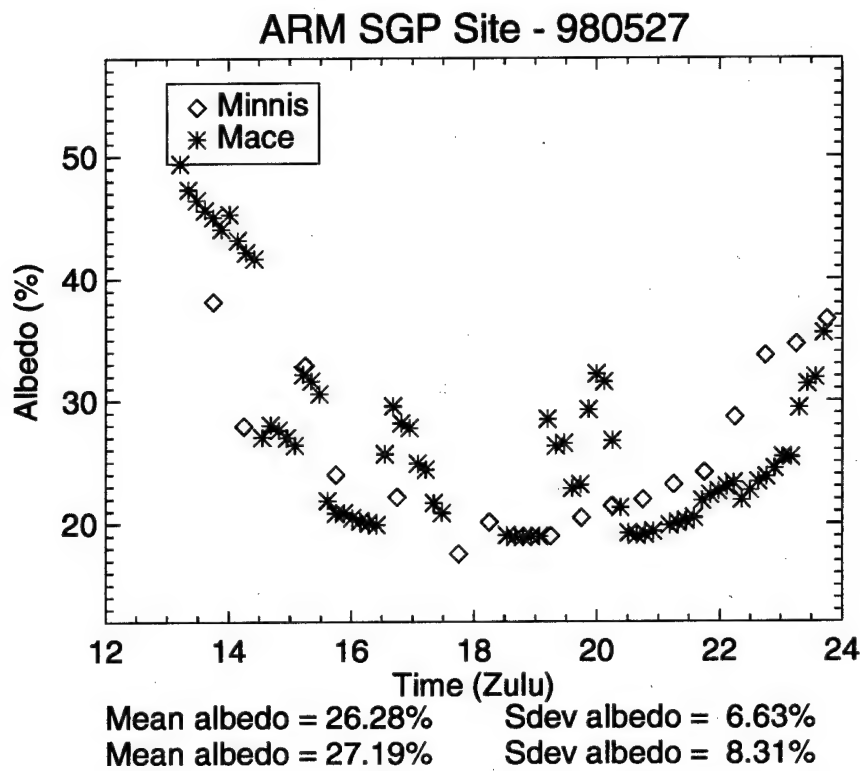


FIG. 43. Comparison of TOA solar albedo for the 27 May 1998 cirrus case at the ARM SGP CART site.

## REFERENCES

Ackerman, T. P., K. N. Liou, F. P. Valero, and L. Pfister, 1988: Heating rates in tropical anvils. *J. Atmos. Sci.*, **45**, 1606-1623.

Ahrens, C. D., 1994: *Meteorology Today*, West Publishing Company, 592 pp.

Anderson, G. P., J. H. Chetwynd, F. X. Kneizys, E. P. Shettle, L. W. Abreu, W. O. Gallery, J. E. A. Selby, S. A. Clough, P. K. Acharya, A. Berk, L. S. Bernstein, M. W. Matthew, S. M. Adler-Golden, D. C. Robertson, 1998: *MODTRAN User's Manual Versions 3.7 and 4.0*, Phillips Laboratory/Geophysics Directorate, 61 pp.

Arking, A., 1996: Absorption of solar energy in the atmosphere: Discrepancy between model and observations. *Science*, **273**, 779-782.

Auer, A. H. Jr., and D. L. Veal, 1970: The dimension of ice crystals in natural clouds. *J. Atmos. Sci.*, **27**, 991-926.

Barnett, T. P., J. Ritchie, J. Foat, and G. Stokes, 1998: On the space-time scales of the surface solar radiation field. *J. Climate*, **11**, 88-96.

Barry, R. G., and R. J. Chorley, 1990: *Atmosphere, Weather and Climate*. Routledge, 460 pp.

Berk, A., L. S. Bernstein, and D. C. Robertson, 1989: MODTRAN: A moderate resolution model for LOWTRAN 7, *Air Force Geophysics Laboratory Technical Report, GL-TR-89-0122*, A1-A37.

Brown, P. R. A., and P. N. Francis, 1995: Improved measurements of the ice water content in cirrus using a total water probe. *J. Atmos. Oceanic Technol.*, **11**, 410-414.

Cess, R. D., M. H. Zhang, P. Minnis, L. Corsetti, E. G. Dutton, B. W. Forgan, D. P. Garber, W. L. Gates, J. J. Hack, E. F. Harrison, X. Jing, J. T. Kiehl, C. N. Long, J. J. Morcrette, G. L. Potter, V. Ramanathan, B. Subasilar, C. H. Whitlock, D. F. Young, and Y. Zhou, 1995: Absorption of solar radiation by clouds: Observations versus models. *Science*, **267**, 496-499.

Chou, M., A. Arking, J. Otterman, and W. L. Ridgway, 1995: The effect of clouds on the atmospheric absorption of solar radiation. *Geophys. Res. Lett.*, **22**, 1885-1888.

Dowling, D. R., and L. F. Radke, 1990: A summary of the physical properties of cirrus clouds. *J. Appl. Meteorol.*, **29**, 970-978.

Elliot, G., 1988: *Weather Forecasting - Rules, Techniques, and Procedures*. American Press, 153 pp.

Evans, W. F. J., C. Reinhart, and E. Puckrin, 1995: A ground based measurement of the anomalous cloud absorption effect. *Geophys. Res. Lett.*, **22**, 2135-2138.

Francis, P. N., J. P. Taylor, P. Hignett, and A. Slingo, 1997: On the question of enhanced absorption of solar radiation by clouds. *Q. J. R. Meteorol. Soc.*, **123**, 419-434.

Fu, Q., and K. N. Liou, 1993: Parameterization of the radiative properties of cirrus clouds. *J. Atmos. Sci.*, **50**, 2008-2025.

\_\_\_\_\_, and Y. Takano, 1994: On the limitation of using asymmetry factor for radiative transfer involving cirrus clouds. *Atmos. Res.*, **34**, 299-308.

\_\_\_\_\_, P. Yang, and W. B. Sun, 1998: An accurate parameterization of the infrared radiative properties of cirrus clouds for climate models. *J. Climate*, **11**, 2223-2237.

Henyey, L. C., and J. L. Greenstein, 1941: Diffuse radiation in the galaxy. *Astrophys. J.*, **93**, 70-83.

Kato, S., T. P. Ackerman, E. E. Clothiaux, J. H. Mather, G. G. Mace, M. L. Wesley, F. Murcray, and J. Michalsky, 1997: Uncertainties in modeled and measured clear-sky surface shortwave irradiances. *J. Geophys. Res.*, **102**, 25,881-25,898.

Kinne, S., T. Ackerman, A. J. Heymsfield, F. P. J. Valero, K. Sassen, and J. Spinhirne, 1992: Cirrus microphysics and radiative transfer: Cloud field study on 28 October 1996. *Mon. Wea. Rev.*, **120**, 661-684.

Liou, K. N., 1972: Light scattering by ice clouds in the visible and infrared: A Theoretical Study. *J. Atmos. Sci.*, **29**, 524-535.

\_\_\_\_\_, 1973: Transfer of solar irradiance through cirrus cloud layers. *J. Geophys. Res.*, **78**, 1409-1418.

\_\_\_\_\_, and G. D. Whitman, 1979: Parameterization of the radiative properties of clouds. *J. Atmos. Sci.*, **36**, 1261-1273.

\_\_\_\_\_, 1980: *An Introduction to Atmospheric Radiation*, Academic Press, Inc., 392 pp.

\_\_\_\_\_, 1986: Influence of cirrus clouds on weather and climate processes: A global perspective., *Mon. Wea. Rev.*, **114**, 1167-1199.

\_\_\_\_\_, 1992: *Radiation and Cloud Processes in the Atmosphere*, Oxford University Press, 487 pp.

Lohman, U., and E. Roeckner, 1995: Influence of cirrus cloud radiative forcing on climate and climate sensitivity in a general circulation model. *J. Geophys. Res.*, **100**, 16,305-16,323.

Long, C. N., 1995: *Surface radiative energy budget and cloud forcing: Results from TOGA COARE and techniques for identifying and calculating clear sky irradiance*. Ph.D. Dissertation, The Penn. State University, Univ. Park, 193 pp.

Mace, G. G., T. P. Ackerman, P. Minnis, and D. F. Young, 1998a: Cirrus layer microphysical properties derived from surface-based millimeter radar and infrared interferometer data. *J. Geophys. Res.*, **103**, 23,207-23,216.

\_\_\_\_\_, K. Sassen, S. Kinne, and T. P. Ackerman, 1998b: An examination of cirrus characteristics using data from millimeter wave radar and lidar: The 24 April SUCCESS case study. *Geophys. Res. Lett.*, **25**, 1133-1136.

Maddox, R. A., 1980: Mesoscale convective complexes. *Bull. Amer. Meteor. Soc.*, **61**, 1374-1387.

Manabe, S., 1975: Cloudiness and the radiative convective equilibrium. *The Changing Global Environment*, S. F. Singer, Ed., Reidel, 175-176.

Matrasov, S. Y., T. Uttal, J. B. Snider, and R. A. Kropfli, 1992: Estimation of ice cloud parameters from ground-based infrared radiometer and radar measurements. *J. Geophys. Res.*, **97**, 11,567-11574.

Minnis, P., K. N. Liou, and Y. Takano, 1993a: Inference of cirrus cloud properties from satellite-observed visible and infrared radiances. Part I: Parameterization of radiance fields. *J. Atmos. Sci.*, **50**, 1279-1304.

\_\_\_\_\_, P. W. Heck, and D. F. Young, 1993b: Inference of cirrus cloud properties from satellite-observed visible and infrared radiances. Part II: Verification of theoretical radiative properties. *J. Atmos. Sci.*, **50**, 1305-1322.

\_\_\_\_\_, W. L. Smith Jr., D. P. Garber, J. K. Ayers, and D. R. Doelling, 1995: Cloud properties derived from GOES-7 for the Spring 1994 ARM intensive observing period using version 1.0.0 of the ARM satellite data analysis program. *NASA Reference Publications*, **RP-1366**, 1-59.

\_\_\_\_\_, D. P. Garber, D. F. Young, R. F. Arduini, and Y. Takano, 1998: Parameterizations of reflectance and effective emittance for satellite remote sensing of cloud properties. *J. Atmos. Sci.*, **55**, 3313-3339.

Nemesure, S., R. D. Cess, E. G. Dutton, J. J. DeLuisi, Z. Li, and H. G. Leighton, 1994: Impact of clouds on the shortwave radiation budget of the surface-atmosphere system for snow-covered surfaces. *J. Climate*, **7**, 579-585.

Ricchiazzi, P., S. Yang, C. Gautier, and D. Sowle, 1998: SBDART: A research and teaching software tool for plane-parallel radiative transfer in the earth's atmosphere. *Bull. Amer. Met. Soc.*, **79**, 2101-2114.

Sassen, K., 1991: The polarization lidar technique for cloud research: A review and current assessment. *Bull. Amer. Meteor. Soc.*, **72**, 1848-1866.

\_\_\_\_\_, and L. Liao, 1996: Estimation of cloud content by W-band radar. *J. Atmos. Sci.*, **35**, 932-938.

\_\_\_\_\_, and V. I. Khvorostyanov, 1998: Radar probing of cirrus and contrails: Insights from 2D model simulations. *Geophys. Res. Lett.*, **25**, 975-978.

Schneider, T. L., and G. L. Stephens, 1995: Theoretical aspects of modeling backscattering by cirrus particles at millimeter wavelengths. *J. Atmos. Sci.*, **52**, 4367-4385.

Smith, W. L., X. L. Ma, S. A. Ackerman, H. E. Revercomb, and R. O. Knuteson, 1993: Remote sensing cloud properties from high spectral resolution infrared observations. *J. Atmos. Sci.*, **50**, 1708-1720.

Stamnes, K., S. Tsay, W. Wiscombe, and K. Jayaweera, 1988: Numerically stable algorithm for discrete-ordinate-method radiative transfer in multiple scattering and emitting layered media. *Appl. Opt.*, **27**, 2502-2509.

Stephens, G. L., S. C. Tsay, P. W. Stackhouse, and P. J. Flatau, 1990: The relevance of the microphysical and radiative properties of cirrus clouds to climate and climatic feedback. *J. Atmos. Sci.*, **47**, 1742-1753.

\_\_\_\_\_, 1994: *Remote Sensing of the Lower Atmosphere*, Oxford University Press, 523 pp.

\_\_\_\_\_, R. D. Cess, M. H. Zhang, P. Pilewskie, and F. P. J. Valero, 1996: How much solar radiation do clouds absorb. *Science*, **271**, 1131-1136.

Takano, Y., and K. N. Liou, 1989: Solar radiative transfer in cirrus clouds. Part I: Single-scattering and optical properties of hexagonal ice crystals. *J. Atmos. Sci.*, **46**, 3-19.

\_\_\_\_\_, and P. Minnis, 1992: The effects of small ice crystals on cirrus infrared radiative properties. *J. Atmos. Sci.*, **49**, 1487-1493.

Toon, O. B., C. P. McKay, T. P. Ackerman, and K. Santhanam, 1989: Rapid calculation of radiative heating rates and photodissociation rates in inhomogeneous multiple scattering atmospheres. *J. Geophys. Res.*, **94**, 16,287-16,301.